Doctoral dissertation

Development of low-grade waste heat recovery using lead-free pyroelectric $Ba(Zr,Ti)O_3$

Ngo Nguyen Chi Trung

Department of Science of Technology Innovation
Nagaoka University of Technology, Japan

Supervisor: Nakayama Tadachika

February 11, 2023

Contents

List of Figures

List of Tables

Abstract

In 2016, 72% of the world's energy corresponding to approximately 341 PJ, was reported to be lost during conversion and exhaust to the surrounding environment as a form of waste heat. Quickly, multiple countries and areas realize the enormous potential of waste heat as a clean renewable source. Waste heat recovery contributes 1585.3 TWh to the total energy supply of the United State. Another area is European with 12.44 TWh of waste heat recovered in 2018. Japan also recovered about 0.8 PJ/year using heat exchangers and economizers.

Although waste heat recovery shows multiple successes and is taking measures against the global energy crisis, most of the recovered waste heat was in the medium to high-grade ($>$ 200 ℃), leaving behind more than 63% of medium low-grade heat ($<$150 ℃). Therefore, recent research is taking an attempt on recycling these high-potential low-grade heat, making them a promising sustainable power source for modern technologies like the Internet of Things, Robots, and Artificial intelligence. Pyroelectricity which can convert fluctuating heat to electricity shows its flexibility towards the nature characteristic of low-grade waste heat, is able to operate without setting up additional cooling devices, and especially work more efficiently under miniaturization, making the technologies the most suitable ones for the suggested applications.

In this research, our group faces two big problems in conventional pyroelectric materials: 1) lack of materials for medium low-grade heat, and 2) being toxicity with lead usage. So far the lowest temperature for a conventional pyroelectric material to exhibit its best potential was above 130 ℃which can slightly cover the medium-grade heat but not the low ones. Furthermore, the materials use lead, which is a pure toxic substance and therefore, is one of many concerns in 17 Sustainable Development Goals (SDGs). As consequence, our group aims the development of a lead-free pyroelectric material that can convert waste heat at temperatures lower than 130 ℃. The objective is to fulfill Goals 7 and 12 of SDGs, provide a sustainable renewable energy source from unused waste heat, and at the same time ensure sustainable consumption and production patterns by excluding the use of toxic substances like lead.

Lead-free Ba(Zr Ti)O_3 - BZT with a phase transition temperature of 93 ℃, exhibits a remanent polarization P_r = 7 μC/cm^2, saturated polarization P_s = 17 μC/cm^2, coercive field E_c = 134 kV/m was chosen as an investigated target in this research. The material undergoes a mix of ferroelectric-relaxor phases, which helps maintain the low phase transition temperature while enabling a large pyroelectric energy against the variation of temperature.

The BZT with 10% Zr was fabricated using the solid-state reaction and hot-press sintering and exhibited a perovskite rhombohedral crystal structure at room temperature. The dielectric constant curve revealed a mix of ferroelectric-relaxor phases which diffuses the permittivity peaks and induces a large polarization variation of $DeltaP_r$ = 0.8 and ΔP_s = 1.1 μC/cm2 with the early phase transition of ferroelectric to relaxor.

As a result, the BZT10 sample under a single heat source (no cooling assist) configuration exhibit a maximum power density of 6.8 mW/cm^3 at a temperature range of 80-100 ℃, frequency f = 0.05 Hz. Increasing the frequency to 0.067 and 0.1 Hz, the maximum power density was enhanced to 8.5 and 8.9 mW/cm^3 respectively. Both are in the temperature range of 70-90 ℃. Efficiently utilizing the pyroelectric effect with the novel Kim cycle was the main reason for the significant increase in power generation ability. On the other hand, heat conduction also kicked in, reducing the achievable energy density and shifting the maximum temperature range to 70-90 ℃. Taking the advantage of the novel Kim cycle, the power density of the BZT10 sample was further enhanced, achieving 15 mW/cm^3 when increasing the temperature difference ΔT to 40 ℃. In addition to the measured value using the cycle loop, the BZT10 sample also exhibits a maximum discharged (output) power density of 13.7 mW/cm^3 showing its potential for an actual application; for example as a power source for a Bluetooth Low Energy which consumes around 2.9 mW/cm^3.

In addition, the BZT10 under a cooling assist configuration also shows a comparatively high energy density. The BZT10 sample exhibit the maximum potential with a heating time of 12.5 s and cooling time of 22.5 s, achieving 504 mJ/cm^3 in the temperature range of 20-120 ℃. This value is higher than any reported bulk-type lead-free pyroelectric materials. Therefore, BZT10 composition is a potential and novel discovery for soft-type lead-free bulk ferroelectric materials used in energy harvesting applications.

Finally, to further enhance the pyroelectric power generation of BZT10 samples, isovalent Sr and Ca dopants were substituted with ratios of 2.5 mol% and 5 mol%. Sr doping successfully enhances the saturate polarization to a high value of 18.2 $\mu C/cm^2$ and 17.4 $\mu C/cm^2$ for the 2.5 mol% and 5 mol% respectively. The 2.5 mol% Sr doping improved the power generation by 1.4 times for the Kim cycle and 1.1 times for the Olsen cycle. The 5 mol% Sr doping achieved an even higher value, 1.5 times with the Kim cycle and 1.3 times when using the Olsen cycle. Unfortunately, the Ca doping decreased the power generation of the BZT10 samples, dropping down to almost 0 or even minus in both cycles. This was due to a significantly high leakage current induced by a large observed dielectric constant. Nevertheless, Sr doping was a promising method for enhancing the pyroelectric heat-to-electricity of BZT10 samples, making technologies a sustainable and safe solution for batteries crisis in IoT and Robots.

Chapter 1

Introduction

1.1 Potential of waster heat

Depending on the application purposes, energy is converted into various suitable forms during primary energy carriers to final energy use. For instance, the kinetic energy of water flow or geothermal heat in hydroelectric and geothermal power stations is converted into electricity before being stored and carried to households and industries. Here, the stored electricity is again converted back to other forms like heat, light, chemicals, and so on according to the processes of burning, lighting, or synthesizing required in the services [1–5]. However, all the conversions and consumption exist a limited efficiency, which produces an amount of unused energy as heat given to the surrounding environment [6–10]. Waste heat accounts for more than 50% of the total produced energy exhibits great potential and is considered an important factor for the current environmental problems. In this section, we will go over the availability of waste heat to clarify the motivation of this studies, at the same time, specify the targeting characteristics of waste heat required for the later system design.

1.1.1 Estimation of the global energy efficiency and lost

In an attempt of utilizing energy usage to face the great demand of the global economy, many studies have been conducted, estimating the amount of available lost (waste heat) from the primary energy sources; through fuel transformation, electricity generation, and end-use device conversion; and finally to useful energy (Fig. 1.1) [11–14].

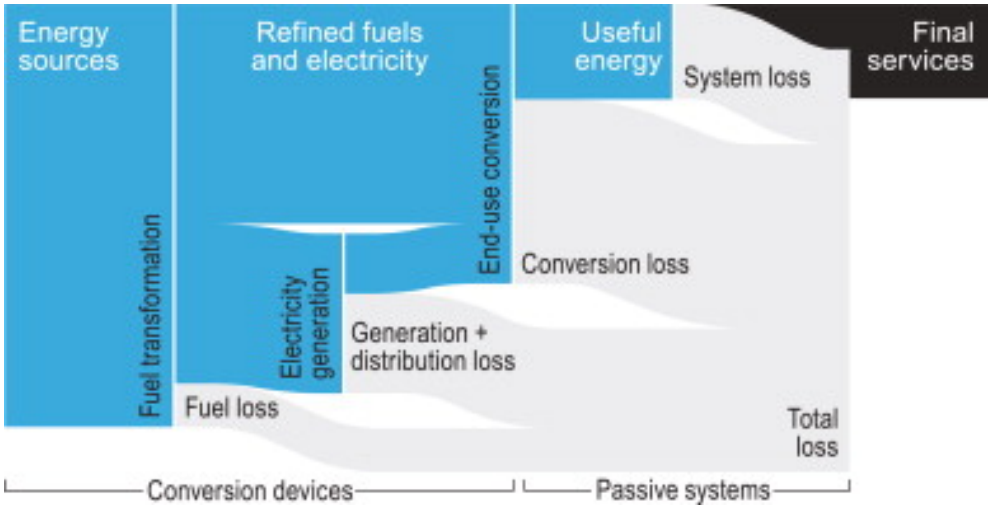

Figure 1.1: Energy conversion from primary sources to end-point devices. [15]

The most popular way to determine the availability of waste heat is by extracting the loss caused by the energy conversion that took part in each of the suggested processes by dedicating their limited efficiency. Depending on the elements that affect and constraint the energy demand, the efficiency target could be divided into three groups: economic potential defined by the market forces, technical potential accounts for the practical efficiency limitations, and the theoretical potential which is the thermodynamic efficiency limits [16–18]. Fig. 1.2 compares three approaches and exhibits the variety of the calculated values on estimating the potential amount of available lost. Since each approach starts from different aspects like economy or technology, there would be some limitations which spread the accuracy widely [19, 20]; however, the variety in the approaches gives the motivations to different fields on which advantages can be taken from these losses. Nevertheless, the reported great potential of waste heat and the curriculum state of the world energy demand has led our groups to research practical methods of taking advantage of these available losses.

World Energy Outlook and historical trend of global energy usage

In detail, the World Energy Outlook (WEO) analysis the trends in world energy demand and supply. The result is based on an approach from the long-term targets on economic potentials, tracking current trends in different

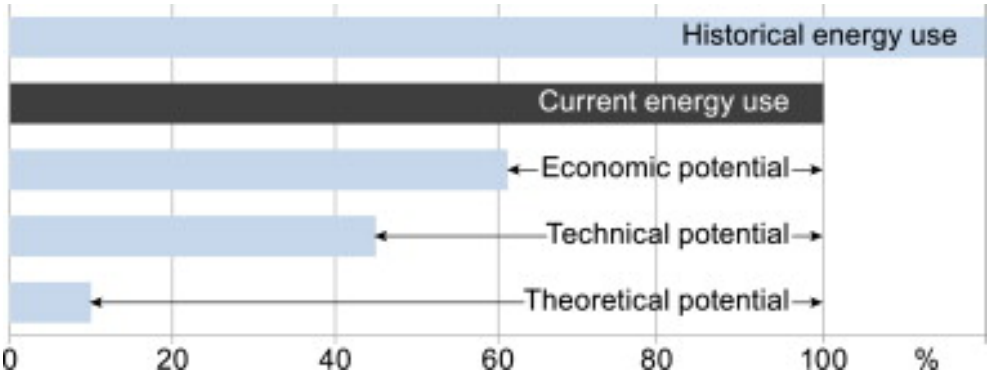

Figure 1.2: Comparison of target efficiency by using economic potential, technical potential, or theoretical potential [11].

efficiency parameters and extending the values into the future, to determine the later potential usages. According to the WEO 2021 report [21], the energy consumption in each sector of industry, transport, buildings, and others in 2020 was 156.1 EJ, 105.1 EJ, 127.2 EJ, and 24.3 EJ accounting for 37.8%, 25.5%, 30.8%, and 5.9% of the total energy consumption. The value takes 70.1% of the 589.1 EJ total energy supply, leaving 29.9%, equal to 176.3 EJ of energy loss including waste heat. Also, in this report, the energy efficiency improvements were expected to save around 5 EJ for advanced economies, and 10 EJ for emerging market and developing economies, which potentially reduce the future overall energy demand by almost 10%. Furthermore, as shown in Table 1.1, since 2010, the fraction ratio of energy loss over the total energy supply has been gradually reduced over the years. In 2010, the loss was 31.2%, accounting for 167.6 EJ; in 2018 the fraction reduced to 30.4%, equivalent to 181.7 EJ; and continuously downed to 30.2% in 2019 with 182.4 EJ, before reaching the 29.9% of 2020 [22–24]. The result corresponded to the development and application of advance technology on improving the energy efficiency including the recovering and recycling of waste heat. The waste energy management technology exhibited its great economic potential and give more motivation on developing techniques to handle the remarkable value and decently growth over years of the remaining non-touched energy loss.

Table 1.1: Evolution of energy loss from 2010 to 2020

Year	2010	2018	2019	2020
Energy supply (EJ)	538.1	598.7	603.2	589.1
Energy consumption (EJ)	370.4	417.0	420.8	412.8
Energy loss (EJ)	167.6	181.7	182.4	176.3
Useful percentage (%)	68.8	69.6	69.8	70.1
Loss percentage (%)	31.2	30.4	30.2	29.9

Theoretical potential estimation

Due to the great economic potential, and the support from governments with efficiency limits regulations, energy loss, and waste heat technology have drawn much attention from researchers [25–27]. Different from the historical trends-based analysis of the WEO, Cullen, and Allwood applied a theoretical model [15], which determined the upper-efficiency limit of the thermodynamics, and defines the absolute target from that. The method compares the working of conversion devices on the same basis of the thermodynamic property exergy (or the availability) which provides a more practical potential to be achieved [28–30]. Using the theoretical model, in 1975, Reistad determined the overall efficiency of the United State to be 21% and was the first exergy analysis of an entire society [31]. Later, in 2010, based on the exergy calculation, Cullen and Allwood created a global map of energy conversion efficiency. The result reported a total of 89% of energy was lost with the technology at that time, leaving only 11% of primary energy actually in use with end-point devices.

Later, in 2016, Forman et al. conducted a novel top-down estimation, calculating thermodynamic efficiency limits from the input side of conversion processes downstream to final energy consumption [32]. The report declares an increase in energy efficiency, up to 28% of the globally consumed energy was converted into 'useful' energy. The reduction of loss compared to the 89% reported by Cullen and Allwood was explained by the different efficiency factors used in the estimation. For instance, a higher overall efficiency of 39% in electricity generation was used compared to the 30%. Although there were some fractions affecting the accuracy of the estimation, the application of

modern technology with improved efficiency could be considered as a factor that strongly impact energy conversion, and raised the sustainability of the global energy demand.

Nevertheless, all of the reports show a significant amount of waste heat in the environment and at the same time revealed the disadvantages of the old-tech system. This encouraged the application of new technology with higher efficiency and enthused the development of reduce, reuse, and recycle systems using the lost waste heat for better energy management.

1.1.2 Waste heat potential by categories

Waste heat potential by sectors

In 2016, Forman et al. the leading group, quantified and reported the availability of global waste heat using a top-down approach [32]. The research covered five sectors: industrial, commercial, residential, transport, and electricity generation. Fig. 1.3 shows the Sankey diagram of world energy use in 2012. Around 44.9% of the primary energy sources were used in electricity generation, producing 23.5% of energy demand for the rest four sectors industrial, commercial, residential, and transport. Among the four sectors, industrial consumed the highest amount of energy, accounting for 22.4%. Following by the industrial sector was the transportation sector with 22.1%, residential with 18.3%, and finally commercial with 9.1%. The remaining 28.0% accounts for the loss during electricity generation.

Fig. 1.4 shows the fraction of energy used and lost in each sector. Transportation has the highest ratio of loss with 81%, 59% of that accounts for waste heat. The second highest one was electricity with 52% of waste heat and 20% of other losses. Finally, commercial generated 33%, residential 35%, and industrial 30% of losses as exhaust/effluents to the environment.

These amounts were slightly improved to 28-29%, 57-59%, 32-34%, 48-55%, and 49-53% corresponding to industrial, transportation, buildings (combining of residential and commercial), electricity, and finally global respectively as reported by Firth et al. based on the 2014 database [33]. Moreover, Firth et al. have also predicted the waste heat trending of 2030 with the 2014 results as shown in Fig. 1.5. Overall, the attribution of industrial and buildings in

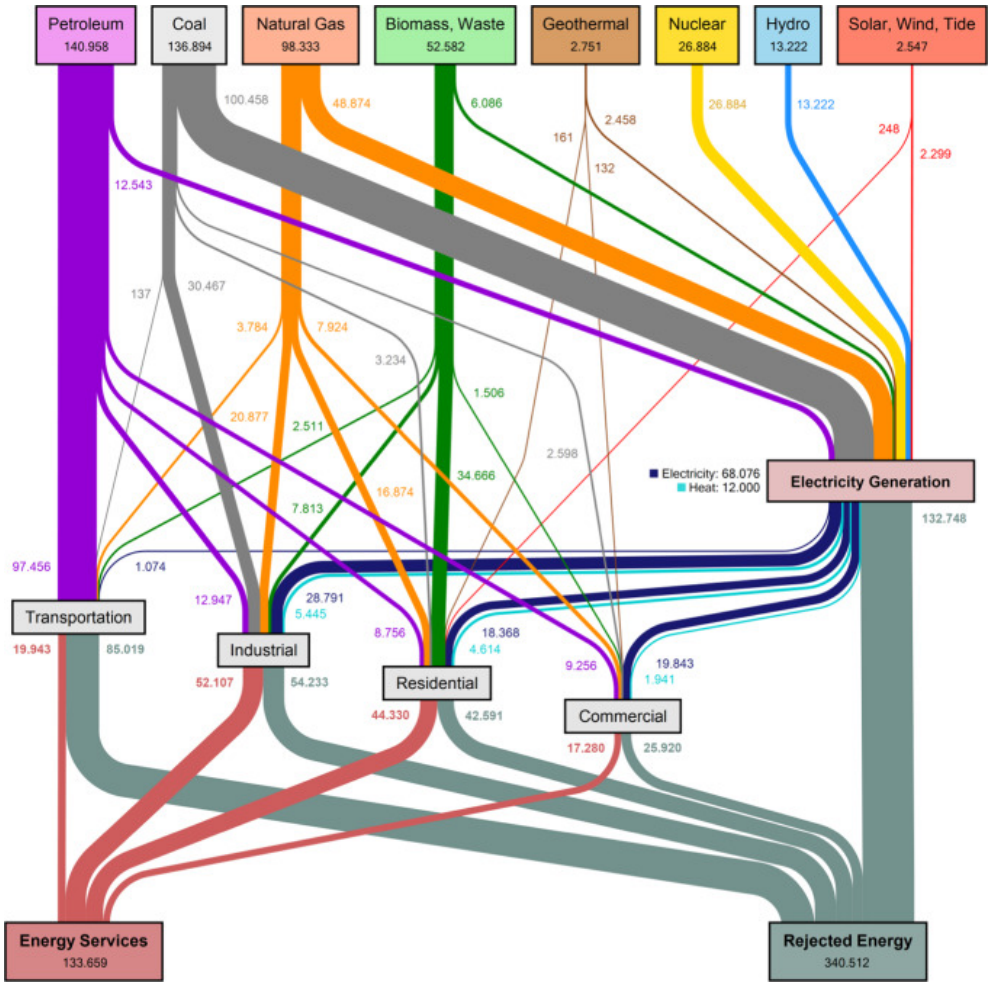

Figure 1.3: Sankey diagram of the global energy use in 2012

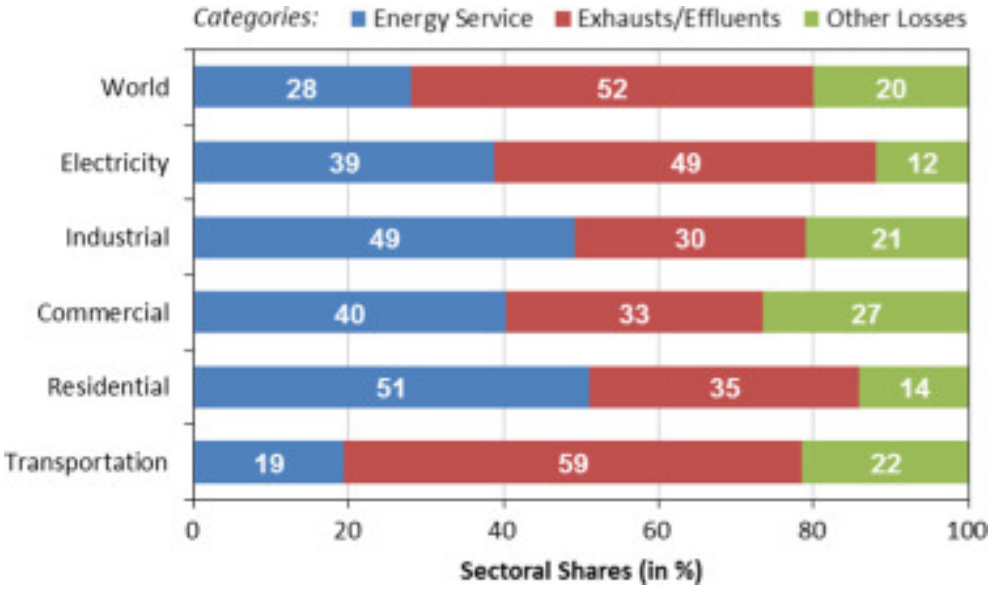

Figure 1.4: Waste heat potential by sectors

total produced waste heat was predicted to increase, while transportation remained almost the same and slight decrease in power generation according to the report.

Waste heat potential by grades

One of the most important factors for designing a recovery system is the temperature of the waste heat. Depending on the level of the target, different techniques have been developed, adapting the aimed efficiency and application environment. Waste heat is divided into three levels: low, medium, and high-grade which corresponds to the temperature $<$ 100 ℃, 100 - 299 ℃, and $\geq$ 300 ℃, respectively. Fig. 1.6 shows the proportion of waste heat by three grades in 2012. Low-grade heat attributes 63% of the total waste heat, 16% belongs to the medium-grade, and the final 21% comes from the high-grade source. Among 63% of the low-grade waste heat, 61% was generated during electricity generation, 18% from transportation, and the rest 21% shares between industrial, residential, and commercial.

In 2014, the fraction of low-grade waste heat grow up to 63.5%, and medium to 31.3%. In contrast, the high grade was reduced to 5.3%. The prediction of

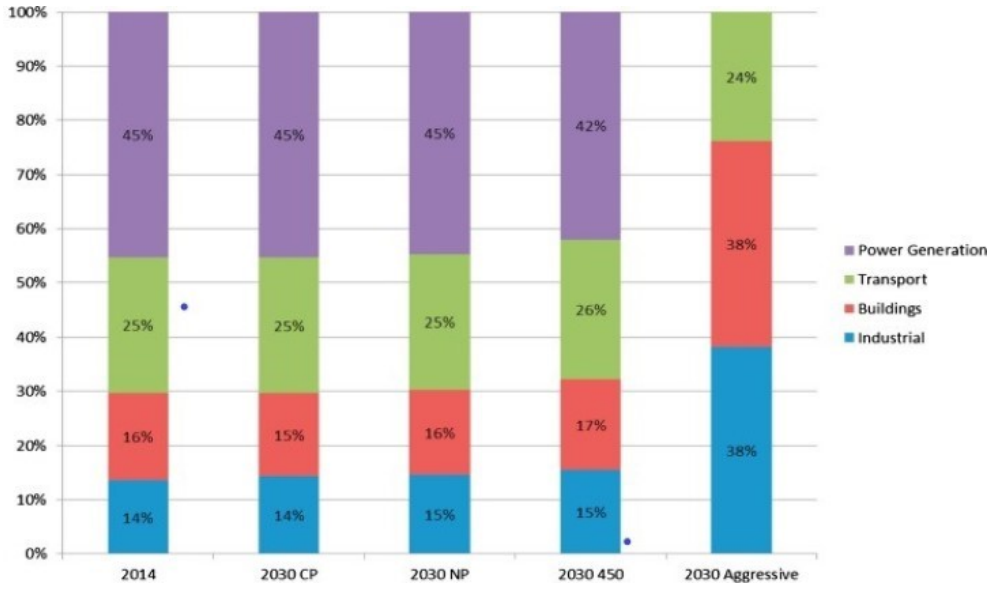

Figure 1.5: Effluent and exhaust losses by sectors in 2014 and 2030

waste heat to 2030 also exhibits an increased tendency in low-grade heat and a slight decrease in medium and high-grade.

Due to the high potential of low and medium-grade waste heat, in this thesis we focused on developing a novel waste recovery method targeting the two suggested areas.

Waste heat potential by regions

United States: As reported by Rattner et al. and by the USA Energy Information Administration, in 2007 more than 60% of the input energy was released as waste heat during the electricity generation process [34, 35]. Among that, low-grade heat share 89.0%, high-grade 7.7%, leaving medium with only 3.3%. In industrial and manufacturing, the temperature of waste heat varies by different fields. In food and beverage production, waste heat was mainly low and medium-grade with low-grade heat sharing more than 60% of exhaust heat in the field. In metal production and non-metallic mineral products, waste heat was 100% high-grade due to all the processes requiring significantly high temperatures. In chemicals, petrochemicals, and plastics/rubbers, the waste heat was varied, with the highest fraction corresponding to the high-

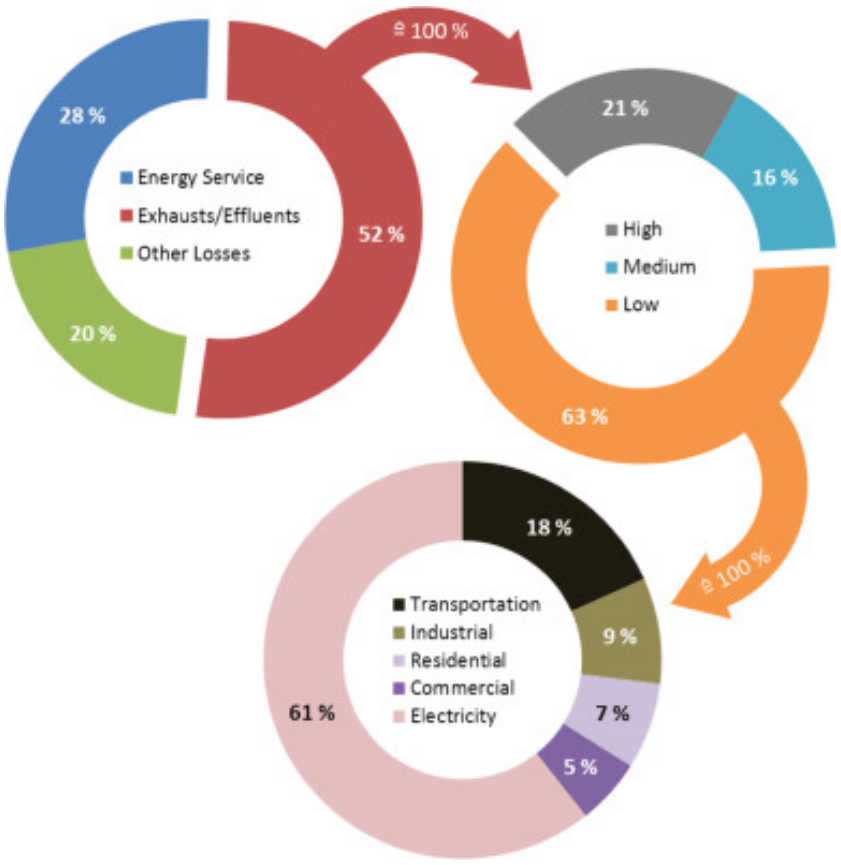

Figure 1.6: Waste heat by temperature. [32]

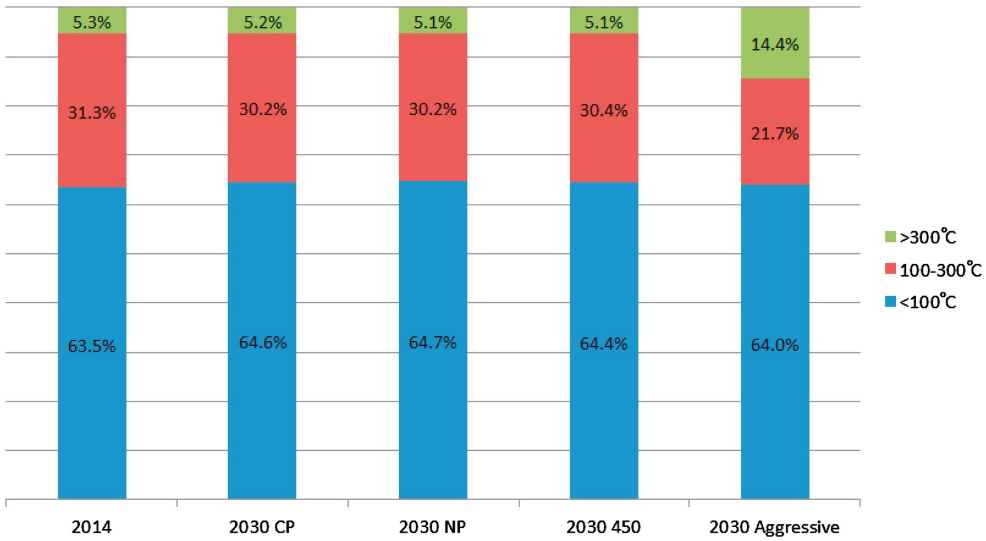

Figure 1.7: The variation in temperature of global waste heat in 2014 and prediction to 2030. [33]

grade heat. Finally, in paper and pulp manufacturing, waste heat is mainly medium-grade with a temperature of less than 200 ℃. In other sectors like commercial, buildings, and residential, waste heat is mostly low and medium grade, approximately sharing an equal amount of 50% the input energy in each sector. Lastly in the transportation sectors, 64.3% waste heat accounts for the low-grade source in engine coolant, and the rest of 35% is relative to the exhaust heat from engines. Fig. 1.8 shows the estimated USA waste heat sources in three sectors: manufacturing, transportation, and power plant by temperature range.

Many waste heat recovery technologies have been applied in the US industry, contributing 1585.3 TWh to the total energy supply and raising the usage efficiency [36]. In detail, the recovered amounts of waste heat in the iron and steel industry, aluminum refining, and metal casting are 13.9 TWh, 0.6 TWh, and 2.3 TWh respectively, which are mainly used in preheating or space heating. A high fraction of recovered energy comes from the industrial boilers, attribute to 1428.7 TWh, and largely in the low-grade range. Fig. 1.9 shows the comparison of energy with and without current waste heat application, declaring a significant role of waste heat recovery nowadays.

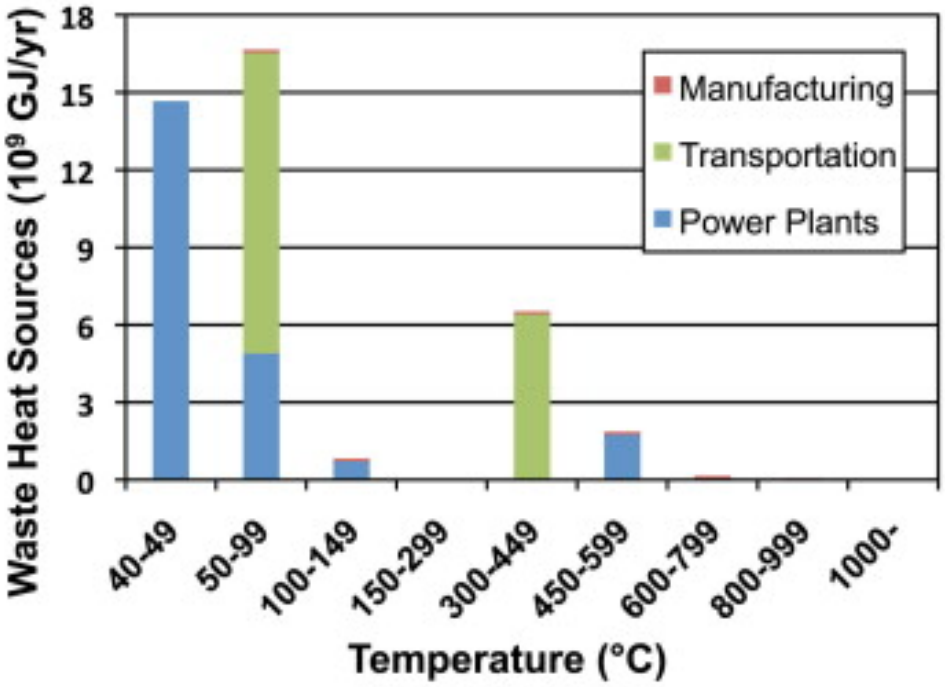

Figure 1.8: Estimated USA waste heat sources in three sectors: Manufacturing, transportation, and power plant by temperature range.

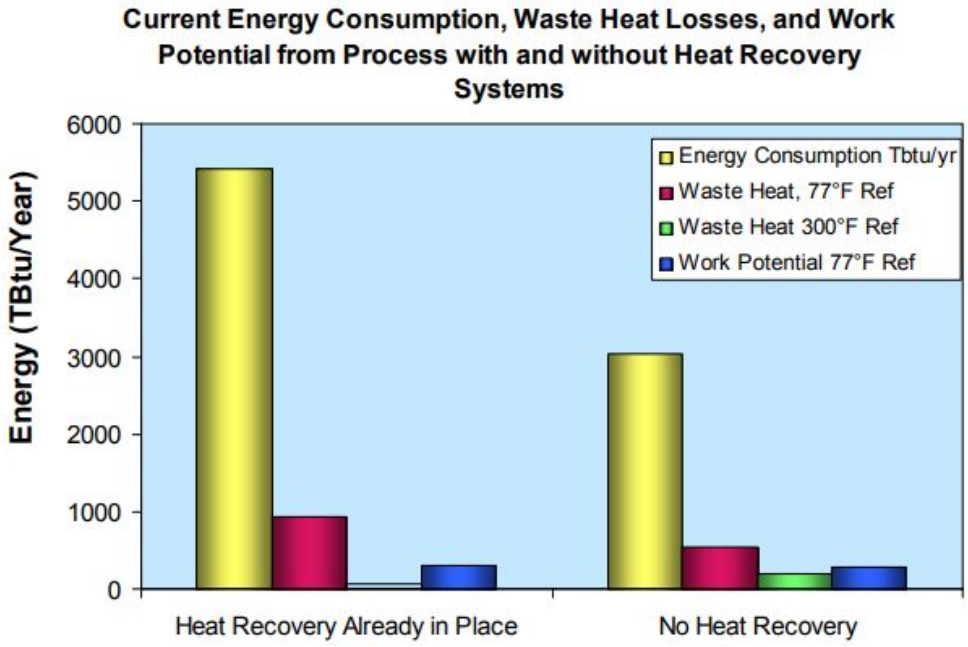

Figure 1.9: Comparison of energy consumption with and without waste heat recovery applications in the US

European Union: In 2018, the waste heat in the power sector of 28 Europe countries (EU28) was estimated to be around 8.6 EJ [37]. 49.5% of the estimated heat comes from nuclear power, which is mainly in the temperature range of 40-90 ℃. The next 39.3% is relative to the coal-fired power plants with temperatures varying from 40 ℃ to below 150 ℃. In contrast, the waste heat in the oil and natural gas sector exhibits a large range of temperatures. In condenser and coolant systems, the waste heat is mainly in the low-grade range with a temperature lower than 100 ℃, while exhaust gas of these sectors usually reaches a high value of up to 600-700 ℃. Fig. 1.10 shows the waste heat temperature in the power sector of EU28.

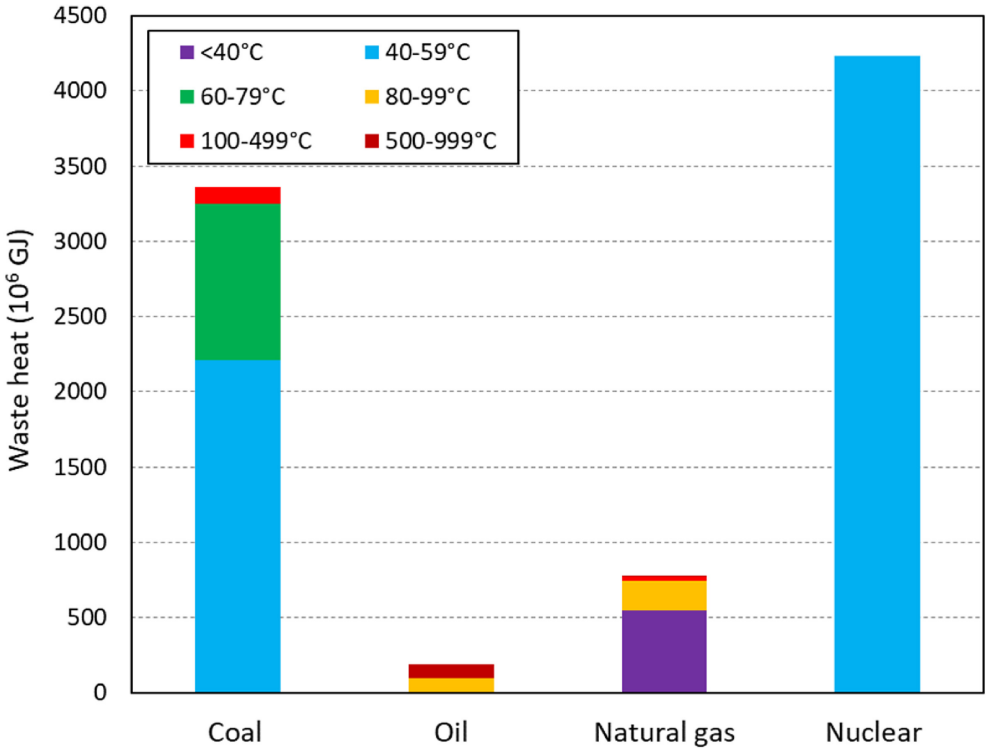

Figure 1.10: Waste heat potential in the power sector of 28 Europe countries

The available waste heat in the industrial sector of the EU was investigated by the six majors: mining, minerals, metals, chemicals, pulp and paper, and food, which accounted for approximately 72% of sold production of EU total manufacturing activities. Firstly, the mining industry consists of waste heat

in a vast temperature range from below 40 ℃, up to around 600 ℃. The waste heat was determined to be around 0.14 EJ, with more than 50% corresponding to the low-grade (Fig. 1.11). Next, the waste heat in the minerals industry was estimated to be 0.45 EJ, mostly at very high-temperature ($\geq$ 900 ℃). The third industry is metal, sharing 0.83 EJ of waste heat. The temperature is high, with the lowest from the sintering process at 350 ℃. For the chemical and, pulp and paper, an amount of 0.04 EJ and 0.09 EJ of low-grade heat was calculated in each industry, respectively. Finally, in the food industry, 0.26 EJ of waste heat was generated, with 89% of them corresponding to the low grade.

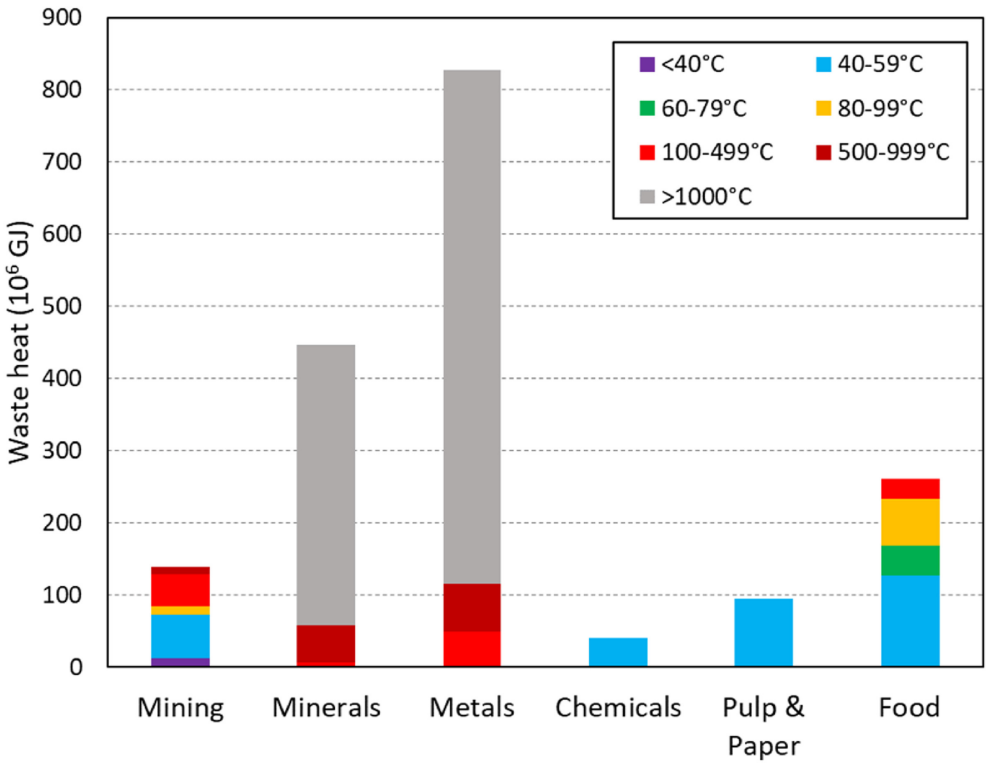

Figure 1.11: Waste heat potential in six main industries of Europe

Utilizing the waste heat technology, in 2018, Europe recovered approximately 12.44 TWh of waste heat, and supply to the total energy demand. Among that, 6-9 TWh comes from the condensing power plants, 0.5 TWh from the incineration power plants, 4.2 TWh in CHP boilers, 0.15 TWh from renewable

energy thermal boilers, 0.03 TWh from data centers, and 0.06 TWh for other installations. Fig. 1.12 shows the total amount of use, and potential for use of waste heat in the district heating CHP plants [38].

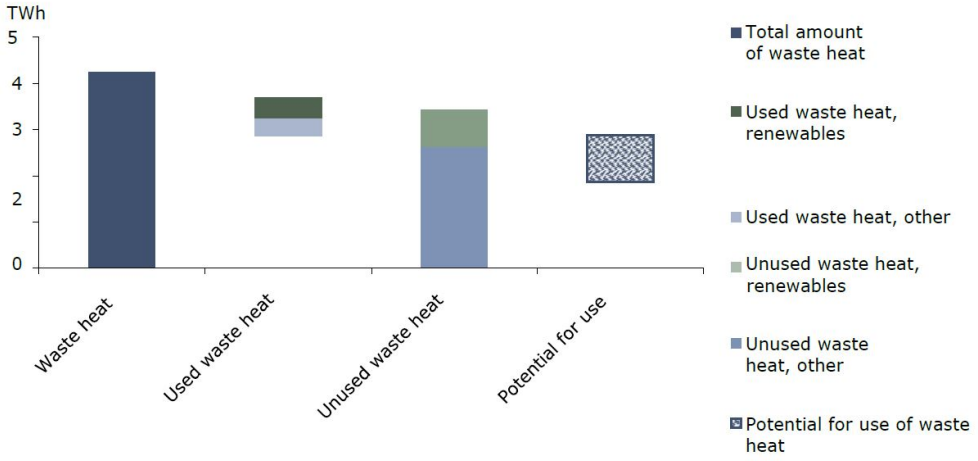

Figure 1.12: Total amount of used, and potential for use of waste heat in the district heating CHP plants of Europe

Japan: In Japan, the power generation sector accounts for the highest fraction of waste heat to the environment (more than 67% of the total exhaust waste heat) [39]. Among that, the low grade took 18.9%, the medium-grade 76.1%, and finally high grade with 5.0%. In the industrial sector, chemicals account for the highest fraction of waste heat: 19.1% of the total waste in the sector, followed by ceramics, clay, and stone products manufacturing with 16.7%, and pulp and paper with 15.9%. For the temperature, ceramics, clay, and stone products manufacturing generate the most low-grade waste heat with 446.8 TJ/year; chemical with the highest medium-grade of 5190.7 TJ/year; and finally the most generated high-grade waste heat accounts for nonferrous metal with 1837.2 TJ/year. Fig. 1.13 shows the Japan waste heat by temperature and sectors.

Currently in Japan, many technologies have been applied, recovering the available waste heat into useful energy. Fig. 1.14 shows the representative waste heat application in Japan [40]. Waste heat recovery boilers were

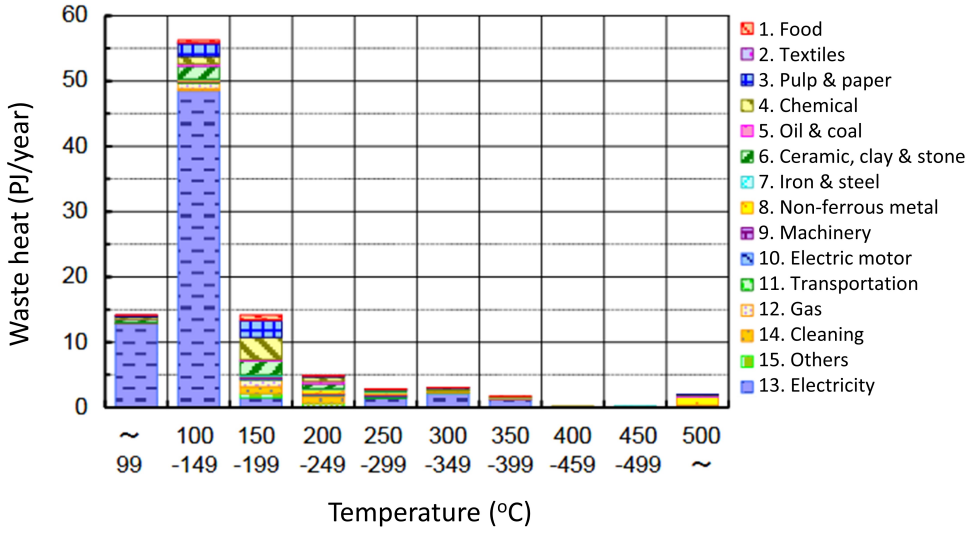

Figure 1.13: Japan waste heat by temperature and sectors

used targeting the source with a temperature higher than 500 ℃, recovered about 0.8 PJ/year. Economizer was applied for a slightly lower temperature, around 450 to above 500 ℃, re-gaining approximately 1.9 PJ/year. Finally, a recuperator (heat exchanger) can recover waste heat at a temperature in the range of 350-399 ℃, supplying around 1.7 PJ to the energy demand.

1.1.3 Thesis target: From low to medium-grade waste heat

The focus target of this thesis is low to medium-grade waste heat, more specifically the temperature lower than 150 ℃. The waste heat below 150 ℃ shows great potential, accounts for more than 60% of the total waste heat, and distribute over various sectors from electricity generation to different end-use areas of industrial, commercial, and so on. However, low-grade waste heat is known as an unstable and fluctuating source which limits its use with some conventional technology. Furthermore, since the efficiency of a thermodynamic cycle is reduced with the temperature difference, the recovery of such a heat source is considered insufficient and hence expensive. Therefore,

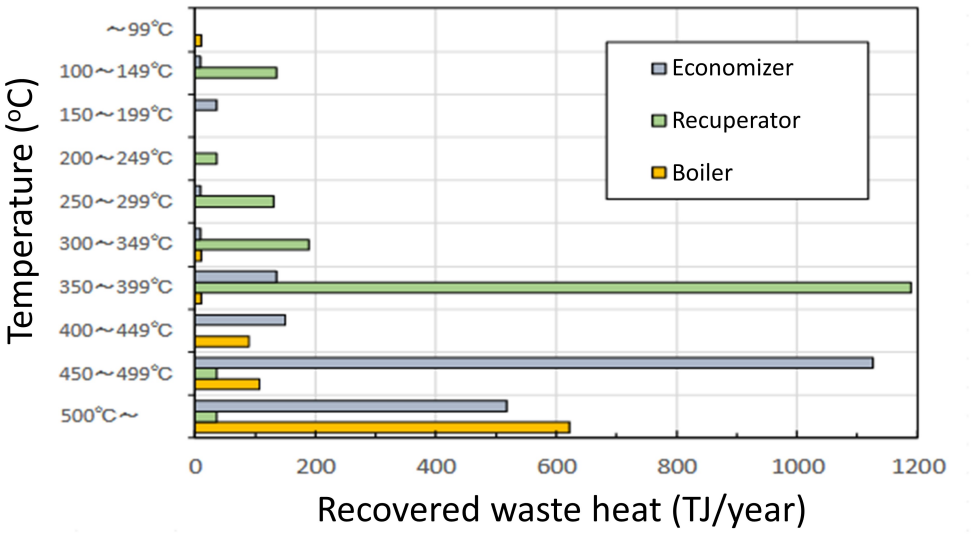

Figure 1.14: Energy saved by waste heat recovery in Japan

currently, most of the waste heat recovery technology is focusing on medium to high-grade sources and ignoring the availability of low-grade heat. The best example is the case in Japan, where most of the technology has an application temperature higher than 350 ℃. This situation opened up the motivation of our group on targeting the high potential low and medium-grade sources for waste heat recovery. Moreover, with the cost of fossil fuels raised over the year, more and more company has paid attention to the field and looking for a solution in the industrial sector. According to a survey conducted in Japan about the need for waste heat recovery technology in different temperature ranges [40]. 59% of the answers account for below 100 ℃ and 34% is corresponding to 100-150 ℃, made the waste heat recover below 150 ℃ most desiring in Japan. Table 1.2 summarized the main characteristic and recovery potential of waste heat of three grades by aspects of proportion, sector, and region approaches.

Overall, the target of our group in this research is to develop waste heat recovery methods in the temperature range from low to medium grade for electricity, commercial, and industrial application.

Table 1.2: Current status and potential of waste heat by grades

		Low-grade	**Medium-grade**	**High-grade**
Proportion		63%	16%	21%
Sector		Mainly in electricity generation. Commercial. Industrial sectors like food, pulp& paper, chemicals	Residential. Industrial sectors like mining, food processing, pulp& paper.	Transportation. Industrial sectors like metal production, non-metallic mineral, and petrochemicals.
Region	US	A large amount of low-grade heat was contributed from industrial boilers.		High-grade heat was recovered in the iron and steel industry, aluminum refining, and metal casting.
	Europe	A total of 12.44 TWh was recovered and contributed to the total energy demand		
	Japan	93% of companies are willing to have waste heat recovery up to 150 ℃	Medium to high-grade heat was captured with economizer, boiler and recuperator	

1.2 Waster heat recovery technology

With the fast development in the economy and the rapid rise of population, the world's energy demand kept escalating over years and years. Furthermore, the Corona SARV virus and war crisis stopped the supply chain, energy became a top-concerned problem more than ever before. To adapt the curriculum state, multiple plans, measures, and regulations have been discussed and seen applied following the overall 3R in management waste: Reduce, Reuse, and Recycle.

1.2.1 Reduce

Electricity generation

Fossil fuels: The Reduce management focuses on improving the efficiency of all the conversion processes from the primary energy supply to the final end-used devices by upgrading and replacing the old high-power consumed facilities. For instance, in electricity generation, technologies like Pulverised coal combustion (PCC) utilize the pressures and the temperatures of the steam cycle, hence, enhancing the thermodynamic efficiency of the coal-fired power plant to a different level from sub-critical to ultra-supercritical. In a natural gas power plant, combining alternative generation technologies, like the natural gas combined cycle (NGCC), can reduce waste at the level of the intermediate output, which achieves a significantly high-available efficiency of 60%. The technology is considered the cleanest source of power generated from fossil fuels.

Besides that, the developed technologies in fuel preparation; furnaces and burners; boilers, turbines, and engines, also significantly contribute to the efficiency improvement of fossil-fuel electricity generation. Table 1.3 shows the technologies corresponding to the respective components.

Renewable energy: On the contrary, under the serve effect of climate change and numerous environmental issues, renewable energy draws much attention, hence, receives a remarkable amount of efficiency improvements. The solar photovoltaic cell's efficiency raised from a maximum of 19% for multi-crystalline silicon to 24.7% for normal, and a possible 40% for sputtering multi-crystalline silicon. More development of the solar photovoltaic cells

Table 1.3: Efficiency-improvement technologies applied in the fossil-fuel electricity generation. [41]

	Technology	**Fuel**
Fuel preparation technologies	Coal gasification	Coal
	Coal pulverisation	Coal
	Coal drying	Coal
Furnaces and burners	Improved burners	Coal, gas, oil
	Fluidised beds	Coal
Boilers, turbines and engines	Improved boilers for steam generation	Coal, gas, oil
	Improved steam engines	Coal, gas, oil
	Super-heaters	Coal, gas, oil
	Improved gas turbines	Coal, gas, oil
	Combined cycles (IGCC, NGCC)	Coal, gas, oil
	Improved compressed ignition engines	Oil
	CHP and co-generation (of electricity and heat)	Coal, gas, oil

continues focusing on the thin-film and the technology of the multi-junction cell to increase and overcome the limitation in efficiency [42].

Similarly, the wind turbines used to generate wind energy also received various improvements in design to achieve better efficiency. The optimization of blades number and tip-speed ratio depending on the environment help reach the best power efficient [43]. The wind turbine sizes also received some significant changes, from 20–60 kW capacity with rotor diameters of around 20 m to 2 MW and above, which significantly reduce the production loss of the system. The recent development of wind energy focuses on the Vertical Axis Wind Turbine for complex urban terrains with non-uniform flows. The technology exhibit remarkable aerodynamic efficiency and performance, regarding flow separation which enables its application without requiring a yawing mechanism in severe condition.

End-use services

Industrial: industrial energy efficiency sees a remarkable improvement in the motor systems, which consume approximately 65% electricity of the sector. The technology focuses on reducing losses in motor windings, enhancing aerodynamics, improving manufacturing tolerances, or upgrading magnetic steel. Furthermore, properly sizing components, while reducing electrical/mechanical transmission losses and optimization of all processes are expected to have the most significant impact, possibly saving up to 30% of the energy consumption. The second most important process in the industry is corresponding to heating. The efficiency improvement in this process relies on continuous production processes to reduce heat loss, and efficient design of heating devices like furnaces, kilns, etc. [44]. Fig. 1.4 shows the future advanced technologies for potential energy efficiency improvement.

Building: In the building sector, the most energy consumption process comes from heating and air-conditioning. Therefore, the thermal-insulation and heating, ventilation, and air conditioning (HVAC) are considered critical technologies in the sector, and directly affect the amount of exhaust heat generated. The future development suggests a building envelopes design, combining advanced thermal insulation materials with passive heating or cooling system for an expectation of 57% energy save. [46]

Table 1.4: Future advanced technologies in various industries for energy saving. [45]

Industry	Identified future technologies
Paper/board (paper drying)	Impulse drying, condebelt drying, dry sheet forming, airless drying
Primary steel production	Smelt reduction, strip casting
Secondary steel production	Combination shaft furnace, strip casting
Ammonia production	Membrane reactors
Nitric acid production	Gas turbine or solid-oxide-fuel-cell integration

Transportation: The history of transport vehicles has seen many significant changes in technology, from the steam engine to diesel, gasoline, and finally electric vehicle trend as we see nowadays. Throughout this long time, transportation has received numerous of technology innovations, improving energy consumption efficiency, as well as limiting the eco-unfriendly exhaust gas. The development advanced by two aspects: enhancing the conversion of the fuel energy to work and reducing the vehicle's loads. Advanced engine technologies such as variable valve timing and lift, turbocharging, direct fuel injection, and cylinder deactivation directly reduced losses in the operation of internal combustion engines; integrated starter/generator optimized fuels used during idling, and finally, automated manual transmissions and low friction bearings play an important role in the efficient drivetrain. In contrast, vehicle load technologies can minimize the dynamic factors during the movement. Optimal shapes and loads significantly reduce the losses caused by friction, aerodynamics, and inertia which contribute to the energy saving [47]. The future of transportation is already going to shift to electric vehicles. The technologies would still focus on raising the engine's efficiency, which is the battery in this case, or the development of an applicable new system like fuel cells for more optimal fuel usage. [48]

1.2.2 Reuse

The "Reuse" management utilizes the unused waste heat by applying these effluents in form of thermal energy to multiple heating processes required in each sector of industrial, building, or transportation.

Heat pump

The heat pump is a thermodynamic cycle-based device, which can transfer heat from a heat source such as waste heat, and deliver it in the suitable form to a heat sink for reusing (Fig. 1.15) [49]. Among that, absorption heat pumps require a comparatively low driven temperature and low electricity consumption and are the main technology for reusing waste heat [50]. Different from a mechanical heat pump which is driven by electric energy, an absorption heat pump operates by using thermal energy, and can be used in different configurations depending on the application targets. The system can utilize the high-temperature input with the low-temperature ambient, hence, producing a medium-temperature heat output with a higher power than the high-temperature input. Or in the absorption heat transformer mode, the heat input in medium-temperature was upgraded to high-temperature thanks to the evaporation and expansion of refrigerant [51].

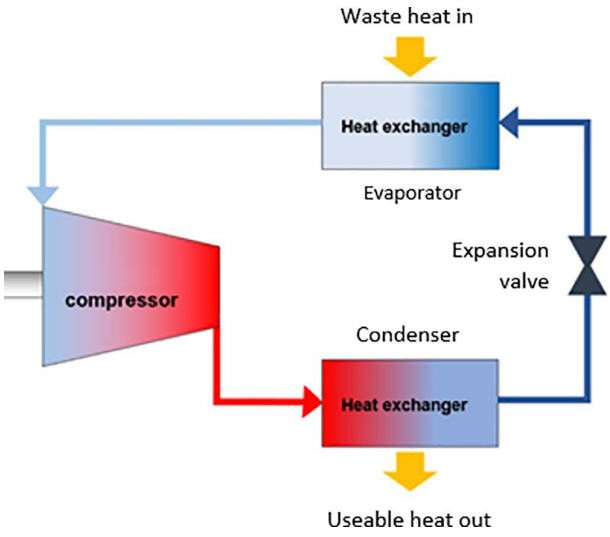

Figure 1.15: Heat pump for waste heat reusing

Currently, the heat pump is available widely from 20 to 100 ℃ commercially and can go up to 250 ℃ with prototype status and laboratory research [52]. The system works at an exergy efficiency ranging from 20% and can go up to around 50% depending on the heat ratio (heat demand divided by the provided heat from waste heat source) [53]. The future development of heat pump targets for multistage cycles which enhance efficiency by 20% by doubling the number of cycles in the conventional single-stage system, or improving the compressor for an experimental energy saving of 80%. Other upgrades such as hybrid systems with solar or geothermal, or replacing the old-fashion chlorine-contained refrigerant HCFC-22 see significant successes in both managing waste heat and protecting our ozone layer [54].

Economizer

Economizer (or finned tube heat exchanger) captures the heat from the exhaust gas by conducting them through a combination of tubes covered with metallic fins, then supply the achieved thermal energy for pre-heating the water [49]. Applying an economizer to a boiler system, the efficiency can be increased by 1% for every 5 ℃ reduction of flue gas temperature, which overall saves around 5–10% of the energy consumption [55]. Table 1.5 shows the application of economizer in lignite-fired power plant for efficiency improvement and power upgrading.

Recent development of economizer uses membrane as fins to increase the surface area of heat absorption, while simultaneously filtering the needed gas out of the contaminated components [57]. Furthermore, the application of ceramic, Teflon, etc., enhanced the resistance from acidic, alkali, corrosion, and high-temperature environment, raising the capability of the technology against harsh ambient conditions [58].

1.2.3 Recycle

Organic-Rankine cycle

The organic-Rankine cycle (ORC) uses a thermodynamic Rankine cycle for converting heat to mechanical energy with the expansion of evaporated working fluid. Analogous to the steam Rankine cycle, the ORC contains all the main components like an evaporator, expansion device, condenser, and pump but replaces the water with an organic compound (i.e. hydrocarbons,

Table 1.5: Application of economizer in lignite-fired power plant [56]

System	Boiler efficiency (%)	Steam turbine plant efficiency (%)	Electric power upgrade (MWe)
Thermal power plant (base)	88.00	44.60	-
Parallel high-pressure economizer	90.16	44.10	26.1
Serial high-pressure economizer	88.78	44.60	0
Low-pressure economizer	89.92	44.33	10.51

refrigerants, ethers, and siloxanes) for a lower phase change (boiling point). Therefore, the ORC is efficient in recovering low-grade heat from biomass combustion, industrial waste heat, geothermal heat, and solar ponds [59].

ORC is applied in the biomass combined heat and power system, saving around 7.5%–13.5% of the energy as electricity [60]. Another efficient application of the ORC is in geothermal binary power cycles. The cycle achieved an efficiency of approximately 5–9% with low-grade heat and 10–15% when using medium-temperature geothermal sources [61]. In solar power cycles, the ORC has an electrical efficiency of 8.6% [62] and can be up to 16% when applied in exhaust heat recovery with gas and steam power cycle [63]. Finally, the system shows an actual efficiency of 13% in internal combustion engines, successfully raising the overall thermal efficiency from 28.9% to 32.7% [64]. Table 1.6 summarizes the efficiency of ORC in each waste heat recovery application.

The future development of the ORC system will continue to target renewable energy and waste heat recovery, helping diminish the effect of economic crisis and environmental problems [65]. However, the high-expected kW scale ORC for waste heat recovery or other domestic applications is currently economically unfeasible due to the comparatively low conversion efficiency.

Table 1.6: Efficiency of Organic-Rankine cycle in different waste heat recovery applications

Application	Efficiency
Biomass combined heat and power	7.5–13.5%
Geothermal binary power cycles	5–15%
Solar power cycles	8.6%
Gas and steam power cycle	16%
Internal combustion engines	13%

Therefore, multiple efforts were made by researchers, trying to improve the efficiency of the mini-ORC to a practicable point to be used as a heat recovery machine in passenger vehicles or domestic combined heat and power [66].

Thermoelectric

Different from the Organic-Rankine cycle, the thermometric is a device that can convert the heat gradient directly to electricity by the mean of the Seebeck effect in semiconductors. A temperature gradient inside the thermoelectric materials is generated by using a combination of high temperature induced by the waste heat source and the low temperature of the built cold sink. Under the Seebeck effect, the high-to-low temperature gradient influences the flow of the electrical carrier and successfully provokes electrical potential difference (voltage) in a similar direction. Particularly, the unused waste heat is recycled into useful electricity [67, 68]. Fig. 1.16 describes the electricity generation from a heat gradient in thermoelectric materials.

The most application of thermoelectric is in transportation, which harvests the energy from the exhaust gas, and can recover around 1-2.5% of the unused heat [70]. Another studies utilize waste heat from an oil pan in the internal combustion engine and achieved an efficiency of 5-9% at a temperature difference of 43 to 76 ℃ [71]. Besides automobiles, thermoelectrics can be applied in other industrial faculties. A thermoelectric integrated heat pipes save around 2.85% of heat to electricity [72], and able to recover 1.1-1.39% of waste heat when applied in a rotary cement kiln [73].

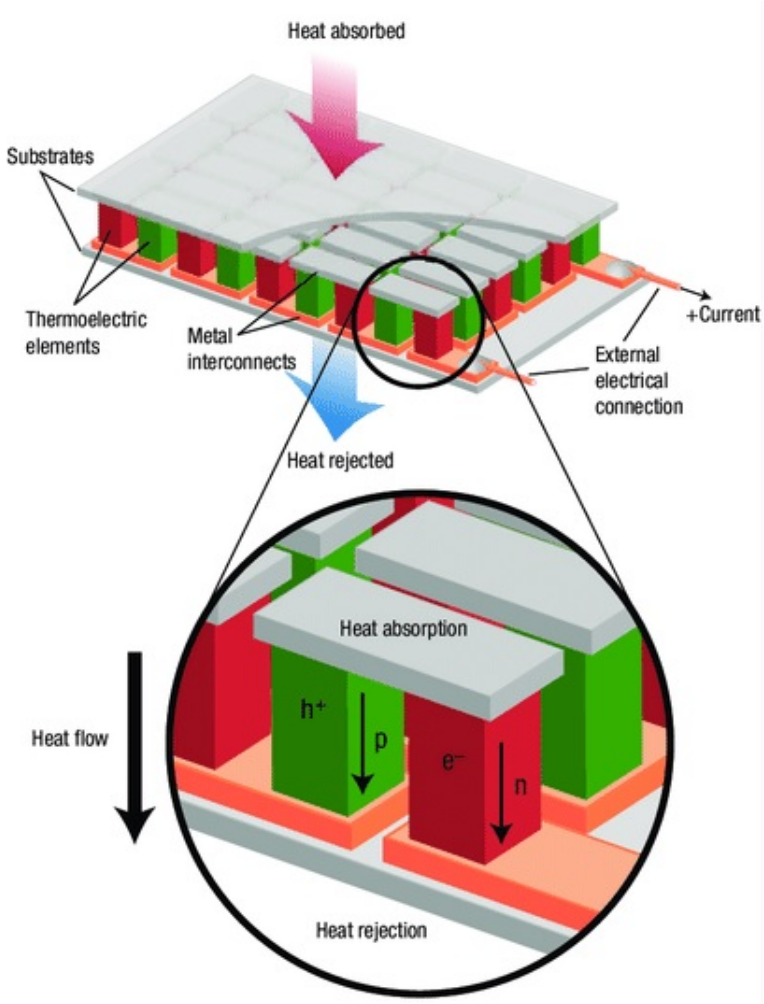

Figure 1.16: Mechanism of direct heat to electricity in thermoelectric device [69]

Although the thermoelectric gathers numerous attention from researchers, it is difficult to achieve high efficiency in the system due to the limited figure of merit [74]. Therefore, nowadays researchers about thermoelectric attempts to improve efficiency by multiple methods like alloying, phonon-glass electron crystal, electron energy filtering, band engineering, and nanostructuring [75].

Pyroelectricity

Pyroelectricity is another system that can convert heat directly to electricity, enabling the applicability of waste heat recovery. However, distinguish from thermoelectric, pyroelectric materials generate electricity from temperature fluctuation rather than the gradient [76]. Utilizing this characteristic, Sultana et al. harvested heat flux from the human body to perform a self-powered temperature sensor with the pyroelectric generator. The system generates 0.034 μW/cm^2 of electricity from the temperature fluctuation of 37-67 ℃, with a response time of 121 ms [77]. Another application of pyroelectric is waste heat recovery from the automotive exhaust gas. Kim et al. reported accumulated energy of 49.12 J/cm^3 from 50-500 ℃ time varied waste heat source [78]. Fig. 1.17 shows the design of a pyroelectric generator used for automotive exhaust gas waste heat recovery.

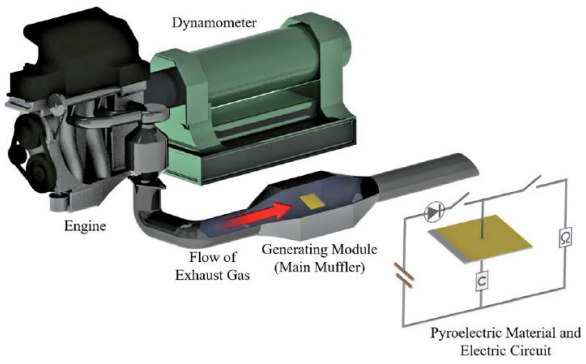

Figure 1.17: Model of pyroelectric generator used for automotive exhaust gas waste heat recovery

Recent advances of pyroelectric materials can achieve a high Carnot efficiency up to 19 % by using a 150 nm PMN–0.32PT thin film in the temperature range 25-115 ℃ [79]. A single crystal is another technology that is applied in

pyroelectric materials, efficiently generating 100 mJ/cm^3 of energy with the fluctuating heat source of 80-170 ℃ when using PMN–0.32PT ceramic [80].

1.2.4 Analysis of 3R thermal management strategies towards the current situation and developing technology

3R thermal management has great potential and a significant effect on resolving the environmental problems and world energy crisis as explained in section 1.1; Potential of waste heat. Each of the strategies has advantages over the others but also exhibits multiple limitations. Reduce is simple and can be proceeded in any system and doesn't require any additional setup, but lost when replaced with a system due to the device-reliant characteristic of the strategy. In contrast, heat-to-heat reuse recovers energy which can be transferred to other processes of manufacturing and pre-heating for uses. However, the strategy required a large-scale setting to compensate for the high loss ratio due to storing and transferring. Finally, the recycle exhibited the best flexibility among 3. Suitable technology can be used to recover heat to optimal form, which then is used, transferred, and stored in separate systems, locations, or production chains. This provides the recycle strategy an enormous potential in future applications, being a secondary power source of modern devices, or a more easy-to-access renewable energy source. Even though the low efficiency of the processes prevents the strategy to be commercial and widespread, future development of technology might overcome the limitation, and make recycling one of the most important strategies for sustainable thermal exploitation. Table 1.7 summarizes the advantages and disadvantages of 3R strategies for application.

Each of the strategies has its advantage over the others, including a ton of successes seen in real-life. However, the flexibility and capability with low-grade waste heat made the recycling strategy the most optimistic method for many modern technologies like the internet of things (IoT), robotics, smart factory, etc. Therefore, a novel approach using the heat to the electricity of pyroelectric material is suggested in this research, developing an eco-friendly waste heat powering method replacing conventional technologies like batteries for an efficient waste management objective.

Table 1.7: Opportunities and obstacles of 3R thermal management strategies

(a) Advantages

Aspects	**Reduce**	**Reuse**	**Recycle**
Application	Since the "Reduce" focus on improving the efficiency limit of the device, the application takes the least space among the 3 strategies. The strategy is applicable in every process without the requirement of an additional set-up. The effect is instant and does not depend on other factors like the surrounding environment compared to 2 other strategies.	Heat to heat strategy is available in almost every place since waste heat is generated in most of the process. Can be stored and transferred to benefit other processes. Extendable to new devices.	Heat is recycled to suitable form with suitable technology for application, which enables the diversity toward multiple targets. Easily to store, transfer, and apply to other devices, especially when in electricity. The target from low to high-grade heat, with scale, varies from small to large.
Development	Multiple aspects like mechanical, electrical, etc., can be proceeded to achieve improvement.	Reuse technology has a high improving rate and profit due to the large-scale characteristic.	Profit/advantage can be earned diversely depending on the integration with other technologies.
Saving rate	High saving potential for new technologies.	Highest achievable efficiency among 3 strategies (Carnot efficiency).	Suitable technology with a decent saving rate for low, medium, and high-grade heat.

Table 1.7: Opportunities and obstacles of 3R thermal management strategies (continued)

(b) Disadvantages

Aspects	**Reduce**	**Reuse**	**Recycle**
Application	The improvement can only be applied to the process itself, and can not be relocated to benefit other steps. The improvement has a built-in characteristic that only generates benefits while being used in the current devices. The replacement of new advanced technology is usually costly.	Size depends strongly on the potential of the waste heat, which en-large the design to earn the necessary profit. Since the potential of the waste heat affects the proficiency, heat to heat is mainly targeted medium to the high-grade source. Heat is hard to store and transfer which generates an additional loss.	Strongly affected by the environment. Require multiple set-ups.
Development	Low improvement rate. Replacement can achieve a high improvement rate but is costly.	Limited on the way of development due to the solitary heat-to-heat conversion method.	Limitation in efficiency is the biggest challenge in developing a recycling system.
Saving rate	Low saving rate with conventional/in-use system.	Significantly drop/hard to earn with low-grade heat	Limited by both the heat absorption and conversion.

Chapter 2

Purpose, approach, and novelty

2.1 Pyroelectricity for low-grade heat to electricity

Table 2.1 summarizes the features of the Organic-Rankine cycle (ORC), Thermoelectric (TE), and Pyroelectric (PE) for waste heat recycling. As a newly developed technology, PE shows the lowest average practical efficiency among the three. However, the recycling process of PE is based on the fluctuation characteristic of the input waste heat which differs from most conventional waste heat recovery including ORC and TE. Low-grade waste heat exhibits an unstable nature, challenging the reliability of many technologies. The efficiency of ORC and TE drops faster at low-temperature, meaning a small variation might cost the whole performance of the system. In contrast, suitably employing PE can generate a decent amount of electricity from a low gradient but fast fluctuating heat source, which is not so promising with ORC and TE.

Another advantage of PE is the simple configuration without a cooling device. In TE and ORC, a cooling device or cold sink is the mandatory part of the system, supplying the necessary temperature gradient to a device for profitable recycling. The setup generates an extra loss during operation, as well as prevent the miniaturization for use in IoT, AI or robotics system, and so on. On the contrary, PE is able to extract the potential from time-dependent characteristics of temperature, meaning both gradient and fluctuation can enhance the conversion rate of the processes. With a single fast fluctuating

Table 2.1: Features of Organic-Rankine cycle (ORC), Thermoelectric (TE), and Pyroelectric (PE)

	ORC	TE	PE
Input	Heat gradient		Heat fluctuation
Output	Mechanical	Electricity	
Grade	Efficient at medium-grade heat	Efficient at medium to high-grade heat	Diversely range depending on the materials
Efficiency	Medium	High	Low

heat source, PE can generate electricity, and combined with a cold sink, a greater efficiency and conversion rate can be achieved. This opens up the applicability to small-scale waste heat recovery systems, which can be used in an electronic circuit like an IoT device or self-powered sensor. Fig. 2.1 shows the configuration of TE and PE for waste heat recovery including the difference in input heat setting.

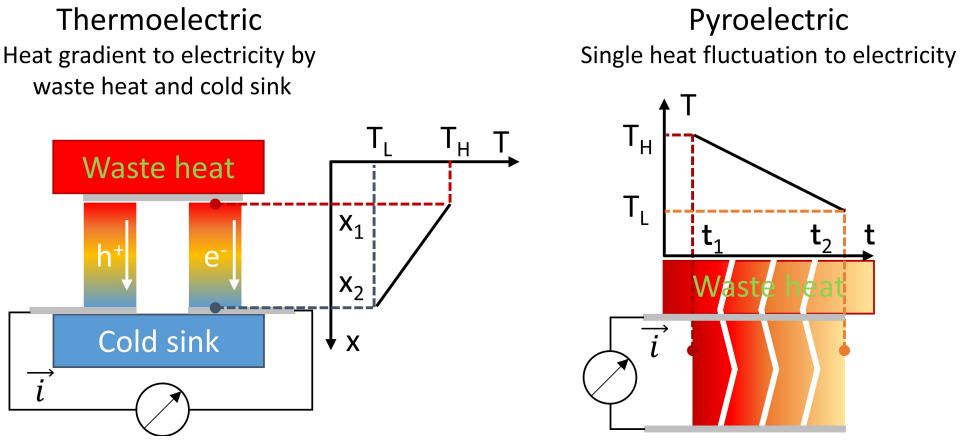

Figure 2.1: Difference in the basic configuration of pyroelectric to thermoelectric in terms of waste heat to electricity recycling. Thermoelectric uses an additional cold sink for heat gradient. Pyroelectric utilizes the natural time variation of waste heat for electricity generation.

Therefore, the PE system with the capability of miniaturization, waste heat's natural fluctuating characteristic to electricity, and simple configuration is the most desired technology to our group and is the main target for this thesis.

2.2 The lack of low-grade solution and environmental issues of conventional pyroelectric waste heat recovery

The conventional perovskite ABO_3 structure-pyroelectric materials substitute the A-site with Pb^{2+} ion (More details will be explained in Chapter 3 Section 1), which leads to two main issues: 1) Medium-high application temperature, and 2) Toxicity of lead.

2.2.1 Medium-high application temperature

Similar to TE, the heat-to-electricity ability of PE materials enhances with the increase of temperature, to an upper limit which is defined as Curie temperature (or Phase transition temperature). The evolution is drastic, where near Curie-temperature generation rate might be 10 times higher than low-temperature ones. Fig. 2.2 shows the power generation ability of a lead-based $Pb(Mg_{1/3}Nb_{2/3})O_3$–$PbTiO_3$ (PMN-PT) and $Pb(In_{1/2}Nb_{1/2})O_3$-$Pb(Mg_{1/3}Nb_{2/3})O_3$–$PbTiO_3$ (PIN-PMN-PT) at difference temperature range for a fix $\triangle T = 40$ ℃. Power generation increased approximately from 0.3 to 3.0 mW/cm^3 in the PMN-PT and 3 times from 1.0 to 3.0 mW/cm^3 in the PIN-PMN-PT materials.

Therefore, the selection of a material with Curie temperature near the application range is necessary. Unfortunately, most of the developed and investigated pyroelectric lead-based materials exhibited a phase transition temperature in the medium-high range. Table 2.2 summarized the most-known lead-based materials: (Pb,La)(Zr,Ti)O_3 - PLZT, $Pb(Mg_{1/3}Nb_{2/3})O_3$–$PbTiO_3$ - PMN-PT, (Pb, La)(Zr, Sn, Ti)O_3 - PLZST,Pb(Nb, Zr, Sn, Ti)O_3 - PNZST, and $Pb(In_{1/2}Nb_{1/2})O_3$-$Pb(Mg_{1/3}Nb_{2/3})O_3$–$PbTiO_3$ - PIN-PMN-PT with the pyroelectric power generation ability published.

The Curie temperature of investigated lead-based material is over 130 ℃, meaning the targeted waste heat needs to be at least 140 to achieve the

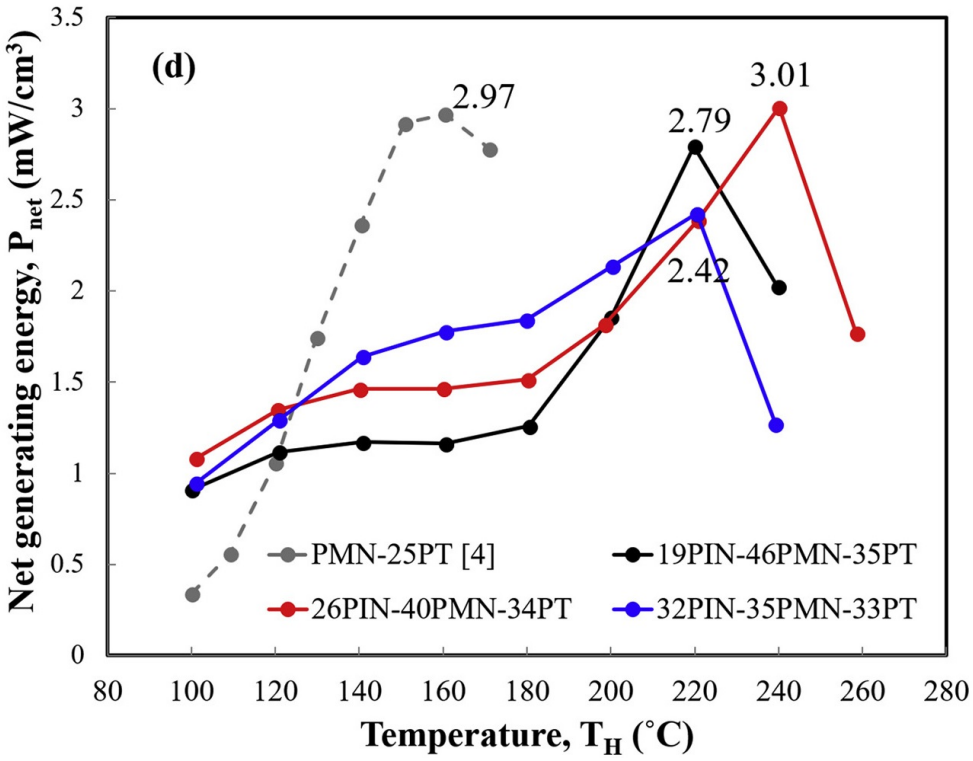

Figure 2.2: Curie temperature dependence characteristic of pyroelectric heat to electricity in lead-based PMN-PT and PIN-PMN-PT [81]

Table 2.2: Curie temperature and power generation of some lead-based materials

Materials	Power (mW/cm^3)	Curie point (°C)	Reference
PLZT	8.74	130	[82]
PMN-PT	8.17	150	[83]
PLZST	10.80	150	[84]
PNZST	11.00	190	[78]
PIN-PMN-PT	3.01	230	[81]

maximum performance. The application at a lower temperature would result in a drastic decrease in power generation. Therefore, a low Curie point is necessary for low-medium grade waste heat recycling.

2.2.2 Toxicity

Lead is a pure toxic substance, which impacts the health of humans, animals, and the natural environment. Low levels of lead exposure results in behavior and learning problems, lower IQ and hyperactivity, slowed growth, hearing problems, and anemia in children, and can cause seizures, coma, and even death in more serious circumstance. Lead exposure in pregnant woman make the baby to be born too early or too small; hurt the baby's brain, kidneys, and nervous system; increase the likelihood of learning or behavioral problems, and put the mother at risk for miscarriage. In adults, lead provoke cardiovascular effects, increased blood pressure and incidence of hypertension; decreased kidney function; and reproductive problems (in both men and women). [85]

In animals, lead also have a serious effect on organs and tissues including the heart, bones, intestines, kidneys, and reproductive and nervous systems, causing some serious problems such as lowering the reproductive ability, inhibiting the activity of anti-oxidative defense system, heart disease, Fanconi syndrome, muscle-mass weakness, tremors, cellular death, etc. [86]

In plants, lead generates similar problems: inhibition of ATP production, lipid peroxidation, DNA damage, preventing seed germination, root elongation, seedling development, plant growth, transpiration, chlorophyll production, and water and protein content. [87]

Lead induces severe issues to every living form in the environment, which makes its name a pure toxic substance. Since lead mining began, humans used to exposure to an amount of lead that is 100 times greater than ever before. This led to the regulation of lead in various industries: the ban on gasoline and paint, monitoring of lead uses in industry and old facilities, etc. Table 2.3 summarizes official lead management directives in 3 countries and areas: Europe, Japan, and China.

The EU directive (RoHS) limited the use of lead in electrical and electronic equipment to under 0.1 wt% including IT & telecommunications equipment. Japan and China's RoHS also set up the maximum lead level to 0.1 wt%

Table 2.3: Official directives about lead regulation in Europe, Japan, and China

Title	Area	Issued	Revised	Ref.
DIRECTIVE 2002/95/EC OF THE EUROPEAN PARLIAMENT AND OF THE COUNCIL of 27 January 2003 on the restriction of the use of certain hazardous substances in electrical and electronic equipment	Europe	2003	2015	[88]
The marking for the presence of the specific chemical substances for electrical and electronic equipment	Japan	2005	2021	[89]
Management Methods for the Restriction of the Use of Hazardous Substances in Electrical and Electronic Products	China	2006	2016	[90]

covering most of the household appliances. Therefore, the lead-free solution is necessary for every industrial and commercial field not only because of the environmental impact but also due to strict regulation of government.

Successfully applying as a self-power source, the pyroelectric device would receive a significant amount of production. Hence, conventional lead-based materials would induce a deleterious effect on the environment and might generate an environmental crisis large enough to force out a banning from the government. For this reason, in this thesis, we investigated and developed a lead-free solution for pyroelectric waste heat to electricity, acting as a self-powering device in IoT, AI, and robotics, and in further future would potentially replace all the conventional lead-based materials for environmental friendly Industry 4.0.

2.3 Purpose of this thesis

The objective of this thesis is to develop lead-free pyroelectric materials with phase transition temperature below 130 ℃ for application in low-grade waste heat to electricity recycling. The system target the self-powering part in

the IoT, AI, and robotics, which requires the power generation of minor power density to operate the working/malfunction monitored sensor, or signal transferring Bluetooth Low Energy (BLE). Furthermore, in a near future, the designed lead-free pyroelectric materials would potentially replace the conventional lead-based ones, contributing to an environmentally friendly smart industry 4.0.

To achieve the designated target, the development of the lead-free pyroelectric materials in the thesis clarified five objectives:

1. Selection of a potential lead-free pyroelectric material with Curie temperature lower than 130 ℃.
2. The synthesis and basic characteristic of selected material toward the heat to electricity conversion.
3. Heat to electricity evaluation for application with single waste heat source configuration.
4. Heat to electricity evaluation for application with heat sink - cold sink combination configuration.
5. Heat to electricity ability enhancement for efficient waste heat recycling.

2.4 Novelty of this thesis in 17 SDGs and smart industry 4.0 points of view

2.4.1 Goal 7 - Ensure access to affordable, reliable, sustainable, and modern energy for all

17 Sustainable Development Goals (SDGs) are shared objectives for all countries to achieve peace and prosperity for people and the planet. SDGs give and encourage the development of technologies a continuous target and responsibility to the future for health and education, reducing inequality, and spurring economic growth [91]. Being the heart of civilization, energy is the top concern for every country. Goal 7 - Ensure access to affordable, reliable, sustainable, and modern energy for all, and enthuse equitable and inclusive communities, where energy can reach and empower everyone's life.

Therefore, the clean and environmentally friendly pyroelectric heat to electricity introduced in this thesis contributes as a key energy harvesting technology for a sustainable smart city. The renewable energy source from pyroelectric low-grade waste heat recovery gives the smart city the flexibility and maintainability to provide people continuous access to information and knowledge, hence constructing a strong education basis and sustainable communities.

2.4.2 Goal 12 - Ensure sustainable consumption and production patterns

Goal 12 - Ensure sustainable consumption and production patterns cover the world's pollution of chemicals and waste, which was and still is doing negative consequences for all living creatures on Earth.

Among that, toxic chemical substances like lead are continuing to contaminate the environment, causing health damage to humans, animals, and plants. The situation is even more crucial in some developing countries. Therefore, chapter 19 in Agenda 21 takes "toxic chemicals" as a topic, and declares that "chemicals should be implemented in ways that lead to the minimization of significant adverse effects on human health and the environment". Moreover, chapter 20 about "management of hazardous wastes" states the key elements of preventing or minimizing the generation of hazardous wastes to achieve the goal "of paramount importance for proper health, environmental protection and natural resource management, and sustainable development".

Consequently, pyroelectric heat to electricity, which is using toxic lead as the main substance, needs and must account the goal 12 as well as chapters 19 and 20 in Agenda 21 as critical issues for developing the technology. This thesis took the reduction and replacement with lead-free as an essential subject, reducing the burden of lead handling as well as the contamination, hence achieving a safer environment for everyone.

2.4.3 Self-powering Internet of Things with pyroelectric waste heat recovery for Smart Industry

Currently, the Fourth Industrial Revolution with the rise of information technology, big data, artificial intelligence (AI), etc., significantly boosts the energy demand, forcing the rapid development of technologies and facilities.

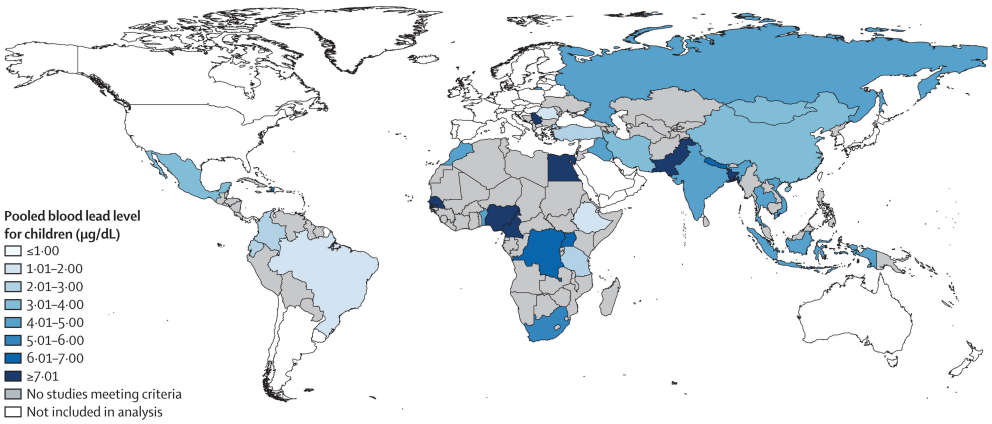

Figure 2.3: Global map of blood lead level for children. Lead contamination and pollution are continuing to a new generation of developing countries [92]

Among that, the Internet of Things (IoT) system which combines a large number of sensors and Bluetooth devices to monitor and efficiently diagnose an automation process, requires a ton of batteries. This rapid rise in maintenance, and replacement costs, as well as the environmental impact of waste batteries, encourage the founding of a new solution with renewable energy.Pyroelectric

heat to electricity, which is flexible with the small-scale for IoT, medium-scale for automotive, AI, to large-scale in 5G towers is considered a promising, worth-investing technology. Therefore, the low-grade waste heat recovery technology introduced in this thesis would take impact and encourage the development and deployment of self-powering IoT, AI, and smart automotive to society.

Chapter 3

Selection of lead-free materials for low-grade waste heat recovery

3.1 Origin of ferroelectricity

3.1.1 Off-centering behavior in ferroelectric materials

The heat conversion ability in pyroelectricity in deep comes from the asymmetry of a ferroelectric material's crystal structure. In detail, a perovskite structure ferroelectric ceramic shares the general chemical formula of ABX_3, where X is usually the anion O^{2-}. Cation A is typically a metallic element or lanthanide, with K^{1+}, Na^{1+}, Pb^{2+}, Ba^{2+}, or La^{3+} being the most common cations. Cation B can be 3d, 4d, and 5d transition metal elements, such as Fe^{3+}, Ti^{4+}, or Nb^{5+}. In an ideal case, cation A in perovskite ABX_3 forms a cubic structure with anion O^{2-} in the center, whereas cation B occupies the corners of the [BO6] octahedra [93–96].

However, because of size effects (doping with different ionic radii components), deviations from the ideal composition (cation/anion vacancy), and the Psuedo Jahn–Teller effect (spontaneous distortions that induce the psuedodegeneracy of vibronic hybridization formed by B and X ion), the perovskite structure under normal conditions is distorted, and the anion X^{2-} is displaced from the center position [98–100]. For instance, a Pb(Zr Ti)O_3 ferroelectric ceramic with a Zr:Ti ratio of 65:35 showed a rhombohedral structure with anion O^{2-} off-centering in the (111) direction. Meanwhile, a Pb(Zr Ti)O_3 ferroelectric ceramic with a different Zr:Ti ratio of 40:60 showed a tetragonal structure

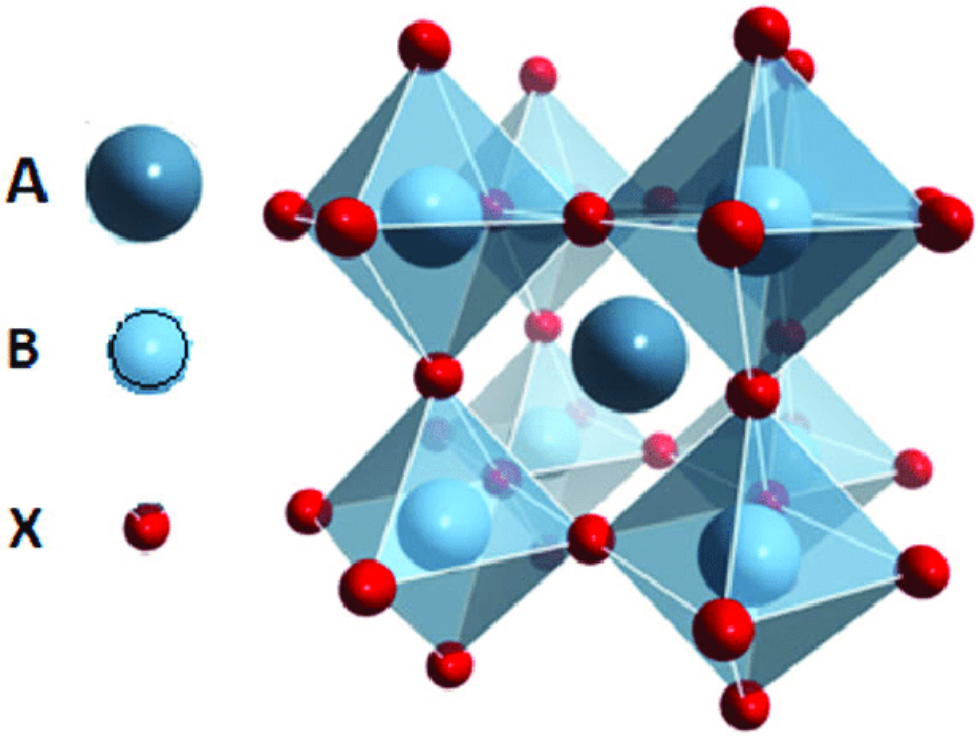

Figure 3.1: Crystal structure of perovskite ABX_3 [97]

with anion O^{2-} off-centering in the (001) direction [101]. Another example is the well-known $BaTiO_3$ perovskite, which has four different phases at different temperatures: Rhombohedral has (111) O^{2-} off-centering, orthorhombic (110), tetragonal (001), and finally, the cubic phase exhibits an ideal perovskite structure with no distortion [102]. The distortion as a result leads to an electrical imbalance in the crystal lattice and induces the formation of electric dipole moments with the direction pointing from the center toward the displaced anion X^{2-} [103–105]. The electric dipole moments are responsible for multiple characteristics in ferroelectric materials, including pyro and piezo-electricity.

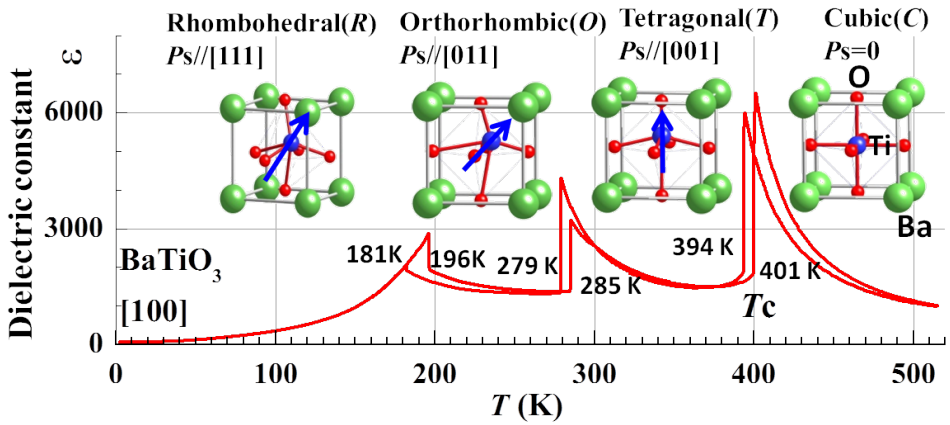

Figure 3.2: Phase transition and O^{2-} off-centering in $BaTiO_3$ composition [106]

Basically, there are 32 point groups of crystals, but only 21 of those are non-centrosymmetric (Fig 3.3). Among that, 10 of the point groups exhibit a high asymmetric, ascending from *hexagonal* $\rightarrow$ *rhombohedral* $\rightarrow$ *tetragonal* $\rightarrow$ *orthorhombic* $\rightarrow$ *monoclinic* $\rightarrow$ *triclinic*. Since the off-centering behavior is responsible for multiple characteristics in ferroelectric, materials in point groups with high asymmetry should be considered favorable targets.

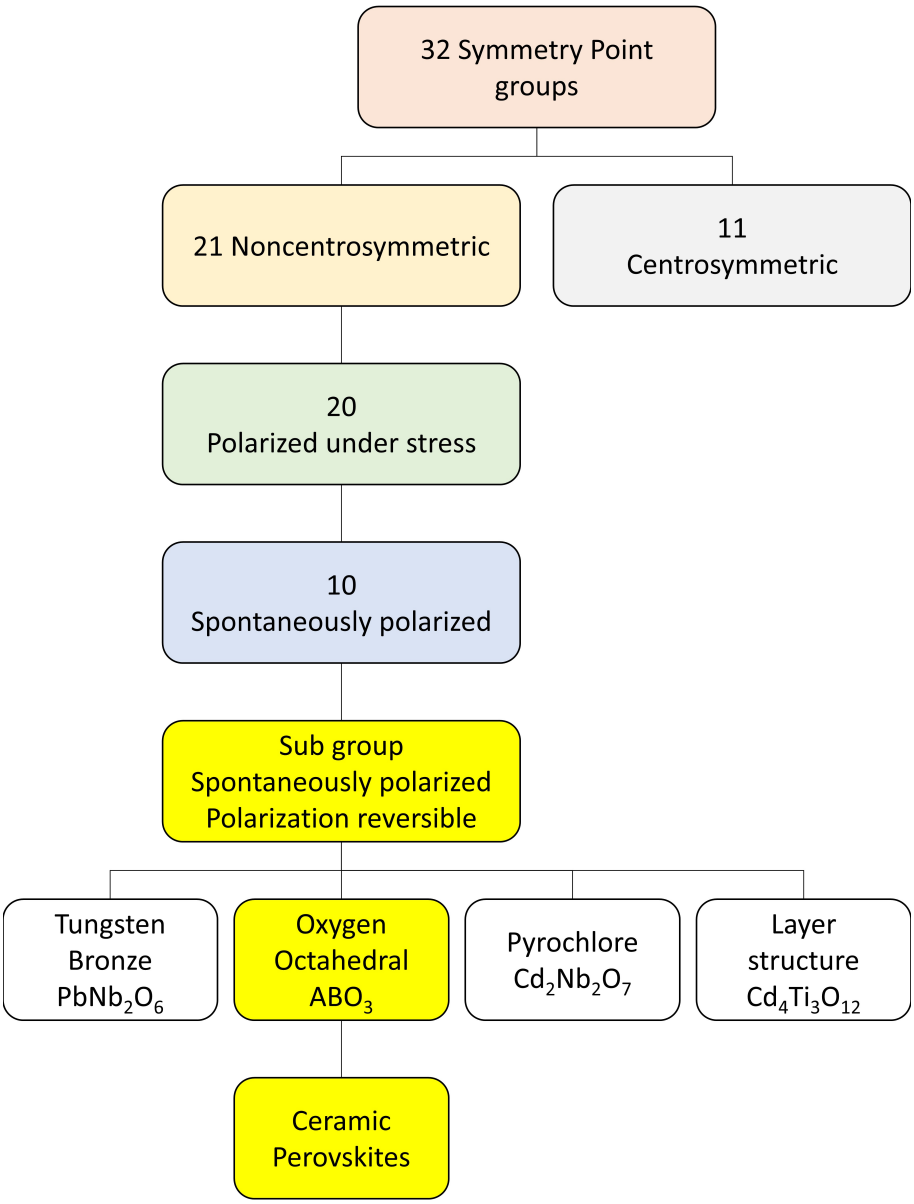

Figure 3.3: 32 point groups of crystals with 10 asymmetric classes for ferroelectric effect

3.1.2 Ferroelectricity for materials selection

Dielectric

Ferroelectricity is defined as materials that possess electric polarization even without an electric field application and can be reversed under the application of an external electric field. Consequently, the ferroelectric materials are comparatively high-resistance against the external field, exhibiting through large dielectric permittivity and ferromagnetic-like hysteresis loop. Fig. 3.4 shows the dielectric constant curve and hysteresis loop of the ferroelectric system.

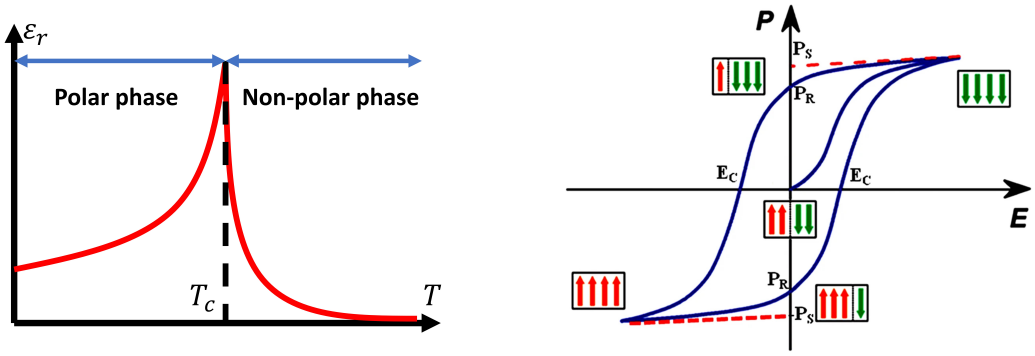

(a) Dielectric constant

(b) Hysteresis loop

Figure 3.4: Dielectric constant curve and hysteresis loop of ferroelectric materials [107, 108]

As the temperature raised, the domain structure which consists of multiple spontaneous polarization in the same direction, became more flexible, leading to the increase of the dielectric constant. However, at a temperature specified as the Curie point, the energy dependence of the nuclear motion surpasses the vibronic coupling, hence the transition to a symmetry phase occurs. Ferroelectric materials start losing their polarization and resulting in a fast drop in permittivity.

In Fig. 3.4b, the hysteresis loop of ferroelectric materials consists of 2 curves without passing through the (0, 0) origin. As the external field reduces to 0, the spontaneous polarization continues existing, causing the hysteresis curve to return to a remanent polarization P_r (meaning the remained polarized

dipole) differs from 0. To reduce the polarization to 0, a further external force application is required and is the so-called coercive field E_c. The hysteresis loop also exhibits a variation with temperature. As the domain structure became more flexible, the remanent polarization P_r and coercive field E_c decreased as temperature rises. Furthermore, the weakening of Psuedo Jahn–Teller effect also leads to the lessening in the displacement level of dipoles, hence reducing the saturated polarization P_s.

Selection of ferroelectric materials can be considered using the dielectric permittivity curve and hysteresis loop as standard. Dielectric permittivity simply exhibits the ability of charge storage in ferroelectric materials, meaning a material with a high dielectric constant value can store more energy at the same applied electric field. However, in terms of electricity generation, this became a limitation. As a high dielectric constant can absorb more energy, it required more energy during the input charging step. Also during the final energy output (discharging), more electricity is held back by the materials, which is lost and consequent a drop in performance.

In contrast, low coercive field, large remnant, and saturated polarization are promising values for the selection of ferroelectric materials for power generation. A low coercive field in ferroelectric help reduce the input energy required for the re-orientation of dipoles and also made the output step consume less power. On the other hand, high saturated and remnant can reduce the unnecessary input charging power, while increasing the potential for polarization-based heat to electricity in the ferroelectric materials.

Therefore, the selection of ferroelectric materials on the dielectric aspect should focus on low dielectric constant, high remanent, and saturated polarization. However, since the electricity is based on heat fluctuation as suggested earlier, temperature-dependent properties like phase transition as well as coercive field, remanent and saturated polarization, and dielectric permittivity under the effect of temperature will be discussed in the later session.

Piezoelectric

Besides the electric field, the domain structure in ferroelectric material can also be affected by inducing strain/stress to the crystal. For instance, when a tetragonal $BaTiO_3$ crystal stands a stress/strain in the z-axis direction, the displacement of anion O^{2-} toward the center position is narrow/extended.

Since O^{2-} off-centering is the origin of spontaneous polarization in ferroelectric materials, the displacement results in the variation of surface charge and generation of electrical current. Fig. 3.5 shows the variation of spontaneous polarization in $BaTiO_3$ when applying stress, and Fig. 3.6 shows the piezoelectric strain loop.

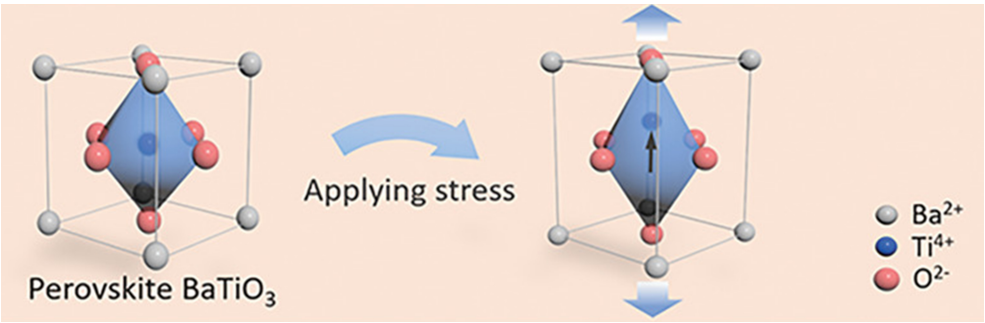

Figure 3.5: Variation of spontaneous polarization in $BaTiO_3$ system when applying stress [109]

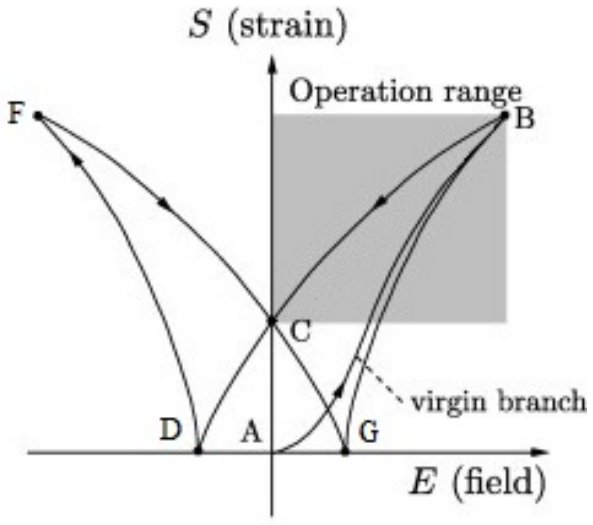

Figure 3.6: Piezoelectric strain loop [110]

When an electric field is applied to the materials, the strain raises from the

non-polarized state toward the curve AB. After reducing the electric field, the strain starts to fall off following curve BC until reaching the coercive field of curve CD. Afterward, the negative field application results in a strain gain of curve DF. The process repeats for the increase of the electric field to the positive coercive field of state FC to CG and then further reaches the maximum value as step GB which forms a butterfly loop featuring piezoelectric. The coupling effect between the elastic (stress T and strain S) and dielectric (electric displacement D and electric field E) parameters in piezoelectricity is described in Equation 3.1 and 3.2 [104, 111].

$$S_p = s_{pq}^E T_q + d_{pk} E_k \tag{3.1}$$

$$D_i = d_{iq} T_q + \epsilon_{ik}^T E_k \tag{3.2}$$

Where, s_{pq}^E is elastic compliance tensor at the constant electric field, ϵ_{ik}^T is dielectric constant tensor under constant stress, d_{iq} is a piezoelectric constant tensor, S_p is the mechanical strain in p direction, D_i is electric displacement in the i direction, T_q is mechanical stress in the q direction, and E_k is the electric field in the k direction. For materials of the 4mm and 6mm crystal class, the equation can be rewritten as:

$$\begin{bmatrix} S_1 \\ S_2 \\ S_3 \\ S_4 \\ S_5 \\ S_6 \end{bmatrix} = \begin{bmatrix} s_{11}^E & s_{12}^E & s_{13}^E & 0 & 0 & 0 \\ s_{21}^E & s_{22}^E & s_{23}^E & 0 & 0 & 0 \\ s_{31}^E & s_{32}^E & s_{33}^E & 0 & 0 & 0 \\ 0 & 0 & 0 & s_{44}^E & 0 & 0 \\ 0 & 0 & 0 & & 0 s_{55}^E & 0 \\ 0 & 0 & 0 & 0 & 0 & s_{66}^E = 2(s_{11}^E - s_{12}^E) \end{bmatrix} \begin{bmatrix} T_1 \\ T_2 \\ T_3 \\ T_4 \\ T_5 \\ T_6 \end{bmatrix} + \begin{bmatrix} 0 & 0 & d_{31} \\ 0 & 0 & d_{32} \\ 0 & 0 & d_{33} \\ 0 & d_{24} & 0 \\ d_{15} & 0 & 0 \\ 0 & 0 & 0 \end{bmatrix} \begin{bmatrix} E_1 \\ E_2 \\ E_3 \end{bmatrix} \tag{3.3}$$

$$\begin{bmatrix} D_1 \\ D_2 \\ D_3 \end{bmatrix} = \begin{bmatrix} 0 & 0 & 0 & 0 & d_{15} & 0 \\ 0 & 0 & 0 & d_{24} & 0 & 0 \\ d_{31} & d_{32} & d_{33} & 0 & 0 & 0 \end{bmatrix} \begin{bmatrix} T_1 \\ T_2 \\ T_3 \\ T_4 \\ T_5 \\ T_6 \end{bmatrix} + \begin{bmatrix} \epsilon_{11} & 0 & 0 \\ 0 & \epsilon_{22} & 0 \\ 0 & 0 & \epsilon_{33} \end{bmatrix} \begin{bmatrix} E_1 \\ E_2 \\ E_3 \end{bmatrix} \tag{3.4}$$

Where the two subscripts describe the direction of stress and strain, with "1", "2", and "3" standing for the x, y, z coordination and "4", "5", "6" are perpendicular to the directions "1", "2", and "3" respectively. Thereby, materials operate at thickness mode under the application of external force F_3 in the

polling direction generating an electrical current i_3 which can be calculated as the following [112]:

$$i_3 = d_{33}\frac{dF_3}{dt} \tag{3.5}$$

Among that the longitudinal piezoelectric coefficient d_{33} expresses the conversion of force to electrical power. As the conversion of strain/stress to piezoelectric power is original from the spontaneous polarization, many researchers believe the selection of materials with a large d_{33} value would also result in a high pyroelectric coefficient for a heat-to-electricity generation.

Pyroelectric

The Psuedo Jahn–Teller effect which induces spontaneous polarization is weakened with the increase in temperature. As a result, exhibiting a temperature variation would quickly cause a drop in spontaneous polarization in ferroelectric materials. In order to maintain electrical neutrality, the surface charge will be released to any connected resistor and perform work. A similar situation would also occur while cooling ferroelectric materials [95, 113–119]. The phenomenon is called pyroelectricity and is the origin of fluctuating heat to electricity in the ferroelectric groups. The continuous repetition of heating and cooling in ferroelectric materials produces the pyroelectric generator as described in Fig. At this time, the generate current i under such condition is calculated using the Eq. 3.6

$$i = -\pi A\frac{dT}{dt} \tag{3.6}$$

Among that, π is the pyroelectric coefficient which directly describes the ability of heat to electricity conversion, A is the sample area, $\frac{dT}{dt}$ corresponds to the temperature fluctuation by time. The selection of materials with high coefficients would be the most optimal strategy for designing a pyroelectric generator. However, besides being beneficial in pyroelectric energy harvesting and temperature sensor, the coefficient parameter rarely sees any play outside the field. Furthermore, the reported coefficient in temperature sensors usually focuses on the room-temperature parameters, which made the database unavailable for the sample selection.

3.2 Phase transition

The heat-to-electricity conversion ability with the pyroelectric effect utilizes the variation of spontaneous polarization versus temperature. When temperature increase, the polarization reduce and vice versa, generating an electrical current in the respective direction. However, the spontaneous polarization can not only change in magnitude but is also able to alternate direction or deplete to 0. This happens during the phase transition at the Curie temperature, where materials change from one crystal class to another with different asymmetry or to a symmetric structure. The most obvious case is the $BaTiO_3$ groups with 4 different phase transitions at 4 distinguished temperatures as introduced earlier. Undergo the phenomenon, the spontaneous polarization exhibit the largest variation, which makes the temperature range near Curie point a promising area for investigating the pyroelectric heat to electricity. The strategies around phase transition focus on 2 patterns: 1. Transition from a high asymmetric crystal structure like monoclinic to the symmetric cubic, or 2. Enhancement due to the nano-domain of the relaxor-ferroelectric phase.

3.2.1 High to low asymmetric phase transition

A ferroelectric material with an asymmetric structure can exhibit multiple phase position before the Psuedo Jahn-Teller effect gets dominated and become a stable centrosymmetric system. For example, the $BaTiO_3$ shows phase transitions from rhombohedral to orthorhombic, to tetragonal, and finally, to the cubic phase for a no-distortion structure. Each of the phase transitions can be utilized, generating a large electric current based on the significant change of the spontaneous polarization during the phenomenon. Therefore, at the beginning era of the field, many different ferroelectric materials were investigated for their specific phase transition which might be effective in applications of both dielectrics, piezoelectric and pyroelectric. Table 3.1 shows some of the first investigated simple materials and their phase transition.

Normally, materials usually exhibit a medium-low asymmetric to a symmetric cubic like in $PbTiO_3$, $PbZrO_3$ or slowly step down from high asymmetric to low and finally to symmetric in $KbNbO_3$ or $BaTiO_3$. To enhance the distortion for a more powerful ferroelectricity, researchers take advances from impurities doping, and substitution to induce size-effect and cation/anion

Table 3.1: Phase transition in some ferroelectric materials

Composition	Phase transition	Ref.
$PbTiO_3$	Tetragonal - Cubic	[120]
$PbZrO_3$	Orthorhombic - Cubic	[121]
$BaTiO_3$	Rhombohedral - Orthorhombic - Tetragonal - Cubic	[106]
$KNbO_3$	Rhombohedral - Orthorhombic - Tetragonal - Cubic	[122]

vacancy. The distortion of the crystal system after the manipulation can be predicted using the Goldschmidt tolerance factor:

$$t = \frac{r_A + r_O}{\sqrt{2}(r_B + r_O)} \tag{3.7}$$

Where r_A, r_B, and r_O are the ionic radii of cation A, cation B, and anion O^{2-}. The factor is used as an indicator for the distortion of the crystal system and the rotation/tilt of the [BO6] octahedra [123–125]. For the ideal cubic structure, the t value is unity. However, as the structure distorts to an asymmetric phase like tetragonal, rhombohedral, or orthorhombic, t is found lower ranging from $0.75 < t \leq 1.0$. Based on the tolerance factor, many researchers substitute cation A with small ionic radii and B with large ones to induce the asymmetric orthorhombic and rhombohedral phase; or reversely A with large and B with small ones for a tetragonal or hexagonal crystal system. For example, the substitution of Zr^{4+} to $PbTiO_3$ would induce the room-temperature phase from tetragonal to rhombohedral with the reduction of tolerance factor [126]. Similarly, the Sr^{2+} doping in $BaTiO_3$ gradually shifts the room-temperature tetragonal to a non-asymmetric cubic phase [102]. Another example is the substitution of ion Sn^{4+} to the $PbZrO_3$ system, which creates a coexistence of tetragonal and orthorhombic phase at room-temperature [127].

The substitution of impurities to perovskite ABO_3 successfully manipulates the distortion level of the crystal system by shifting to a high-asymmetric phase. However, unfortunately, this also means the system requires more energy to transit to a symmetric phase for an effective pyroelectric conversion.

In the Pb(Zr Ti)O_3 system, the high Ti-concentration can raise the Curie temperature up to near 500 ℃. This is totally out of focus for this research. Furthermore, the high-asymmetric phase also leads to a high coercive field, large dielectric permittivity, and ton of leakage current which is an important factor affecting the electricity generation that will be discussed in the later session. Fortunately enough, during the substitution of impurities to the crystal structure, researchers found a coexistence area of multiple phases, leading to many characteristics like Morphotropic Phase Boundary (MPB), or Relaxor phase which sufficiently enhance the ferroelectricity for piezo and pyro application. As MPB is the most efficient method for the piezoelectric, the relaxor phase is the new promising target for pyroelectric development. The next section will discuss the Relaxor phase in terms of material selection.

3.2.2 Relaxor-ferroelectric and nano-domain

Relaxor-ferroelectric is a system where two or more kinds of ions are distributed randomly on crystal [128]. The disorder in ion valence and the instability of multiple phases coexistence, as a result, generate in-homogeneous polar nanoregions (PNRs) [129]. Because of the PNRs, the phase transition from the ferroelectric to paraelectric in such a system is diffused and the dielectric constant shows a broad peak with strong frequency dependence characteristic and a weak remanent polarization [130]. Although, the origin of the relaxor phase, the role of PNRs in the diffusive phase transition, as well as the effect of such mechanism on the pyroelectricity, is still unclear, the combination of weak remanent polarization and the broad dielectric constant peak has seen some success in the pyroelectric energy harvesting [79]. The transition from ferroelectric to relaxor cost less energy than the symmetric cubic, which enables the shift of Curie temperature toward the medium low-grade, while weak remanent polarization together with the high value in normal ferroelectricity can generate a large pyroelectric effect in such a short temperature range. The same mechanism was applied in the lead-based PMN-PT, PLZT, and PLZST [131–133] achieving power generation value over 8 mW/cm^3 at the medium-temperature range (Chapter 2, Section 2.1). Therefore, materials with ferroelectric-relaxor transition would be an ideal composition for pyroelectric generators utilizing medium-low waste heat.

3.3 Ba(Zr Ti)O_3 as a pyroelectric materials for medium-low grade heat to electricity

In summary, a selected material or family is desired to verify as many conditions as shown in Table 3.2

Table 3.2: Summarized of condition for materials selection

Aspect	Condition
Dielectric	Low dielectric constant Low coercive field High remanent polarization High saturated polarization
Piezoelectric	Large piezoelectric coefficient
Pyroelectric	Large pyroelectric coefficient
Phase transition	Ferroelectric - Relaxor Phase transition temperature <130

The Ba(Zr Ti)O_3 - BZT in the BT family is considered the most favorable material that can meet most of the conditions. The substitution of 10 mol% Zr doping to $BaTiO_3$ help reduce the phase transition temperature to 93 ℃, exhibit a remanent polarization $P_r = 7$ μC/cm^2, saturated polarization $P_s = 17$ μC/cm^2, coercive field $E_c = 134$ kV/cm [134]. Furthermore, a mix ferroelectric-relaxor phase was reported in this composition, enabling the potential of high electricity generation in large temperature range [135–137]. Finally, the Ca doping in BZT composition also was reported to help improve the piezoelectric coefficient to a high value of $d_{33} = 604$ pC/N [138]. Therefore, BZT with 10 mol% Zr was chosen as material in this research. Chapter 4 will investigate the fabrication and dielectric properties of the BZT sample. Chapters 5 and 6 will research actual heat to electricity under no cooling-assisted and simulated cooling-assisted conditions. Finally, chapter 7 will investigate the effect of Ca and Sr-doping on the enhancement of the electricity generation ability.

3.4 Novelty of Ba(Zr Ti)O_3

Table 3.3 shows developed lead-free pyroelectric materials in the BT family with Curie temperature below 130 ℃. Bhargavi et al. calculated an energy density of 4.25 mJ/cm^3 for the $Ba(Zr_{0.05}Ti_{0.95})O_3$ using the simulated cooling-assisted conditions.[139]. Ando et al. and Patel et al. reported an energy density of 447 mJ/cm^3 and 108 mJ/cm^3 for the $0.5BaZr_{0.2}Ti_{0.8}O_3$-$0.5Ba_{0.7}Ca_{0.3}TiO_3$, respectively.[140, 141]. Sharma et al. achieved an energy density of 305 mJ/cm^3 using 5% Fe-doped $Ba_{0.85}Ca_{0.15}Ti_{0.9}Ti_{0.1}O_3$.[142]. $Ba_{0.85}Ca_{0.15}Ti_{0.88}Sn_{0.02}Zr_{0.1}O_3$ with 2% Sn reported by Khobragade et al. had an improved energy density per applied electric field and temperature difference value up to 0.169 μJ/(cm^2·K·V) [143]. Finally, the highest energy density calculated in lead-free bulk materials was 486 mJ/cm^3 reported by Fan et al. using the $Ba_{0.72}Sr_{0.28}TiO_3$ materials [144].

The result shows the potential of the BT family for low-grade pyroelectric conversion with diverse temperature ranges and applied electric field. However, none of the reported value was based on an actual test with heat fluctuation. More specifically, the energy density shown in table 3.3 is calculated using two hysteresis loop at constant temperature. Therefore, the phenomenon neglected multiples important factors: thermal factor influencing the temperature adaption, coercive field inducing high-input and loop-cross, finally primary and secondary pyroelectric effect which directly interact with fluctuation behavior (discussed in Chapter 5 and 6). As a result, estimation and measurement shows a large difference leading to applicability barrier and misunderstanding standard for materials selection (Chapter 7).

Therefore, in this thesis, our group will investigate the pyroelectric conversion ability using a proper fluctuating sources to revealed the effect of thermal and electrical factors on the generation behavior. The results give novelty through a reliable standard for system and sample design, and further revealing all the misunderstanding which prevent the application of lead-free system over conventional lead-based ones.

Table 3.3: Calculated pyroelectric conversion behavior of lead-free materials in BT family

Materials	N_D	E_L	E_H	T_L	T_H	$\frac{N_D}{\Delta T \cdot \Delta E}$	P_O	Ref.
$Ba(Zr_{0.05}Ti_{0.95})O_3$	4.25	3.25	7.42	30	125	11	Calculated from D-E hysteresis loop	[139]
$Ba_{0.85}Ca_{0.15}Ti_{0.9}Ti_{0.1}O_3$ - 5% Fe	305	3	90	30	110	44		[142]
$0.2BaZr_{0.2}Ti_{0.8}O_3$ - $0.8Ba_{0.7}Ca_{0.3}TiO_3$	371	0	30	10	150	88		[140]
$0.5BaZr_{0.2}Ti_{0.8}O_3$ - $0.5Ba_{0.7}Ca_{0.3}TiO_3$	108	0	20	30	90	90		[141]
$0.5BaZr_{0.2}Ti_{0.8}O_3$ - $0.5Ba_{0.7}Ca_{0.3}TiO_3$	447	0	30	10	150	106		[140]
$Ba_{0.72}Sr_{0.28}TiO_3$	486	0	70	25	85	116		[144]
$Ba_{0.85}Sr_{0.15}Zr_{0.1}Ti_{0.9}O_3$	300	0	30	30	90	167		[141]
$Ba_{0.85}Ca_{0.15}Ti_{0.88}Sn_{0.02}Zr_{0.1}O_3$	332	1	29	30	100	169		[143]

N_D: Energy density, mJ/cm^3
E_L: Low electric field, kV/cm
E_H: High electric field, kV/cm
T_L: Low temperature, ℃
T_H: High temperature, ℃
$\frac{N_D}{\Delta T \cdot \Delta E}$: Energy density per applied electric field and temperature difference, $\mu J/(cm^2 \cdot K \cdot V)$
P_O: Power density, mW/cm^3, $P_o = N_D \times f$

Chapter 4

Fabrication of Ba(Zr Ti)O_3 and dielectric properties evaluation

4.1 Experimental

4.1.1 Hot-press sintering

Hot-press is the main sintering method used to synthesize samples in this thesis. In this method, the chemical reaction of green powders occurs simultaneously with the densification due to uniaxial high-pressure application [145, 146]. In ceramic synthesis during the molding process, an additional binder such as PVA should be used to increase the success rate of the process, though this decreases the bulk density and increases the rate of impurity phase formation. Hot-press sintering avoids this problem by simplifying the fabrication procedure and enhancing the quality of the sintered pellets. Compared with samples fabricated with conventional methods, samples synthesized by hot-press sintering are expected to have a pore-free, high-density composition.

4.1.2 Synthesis of samples

The $Ba(Zr_{0.1}Ti_{0.9})O_3$ (BZT10) samples were fabricated using a solid-state reaction from solid reagents of $BaCO_3$ (Wako, 99.0%), ZrO_2 (Wako, 98.0%), and TiO_2 (Wako, 99.0%) in the molar ratio of 1:0.1:0.9, respectively. The powders were mixed using a wet ball milling method using Zirconia balls in an ethanol medium for 24 hours. The mixture was then rotary evaporated

and dried in an electric heat at 80 ℃ for another 24 hours. Dry powders were then ground again to obtain a small particle size.

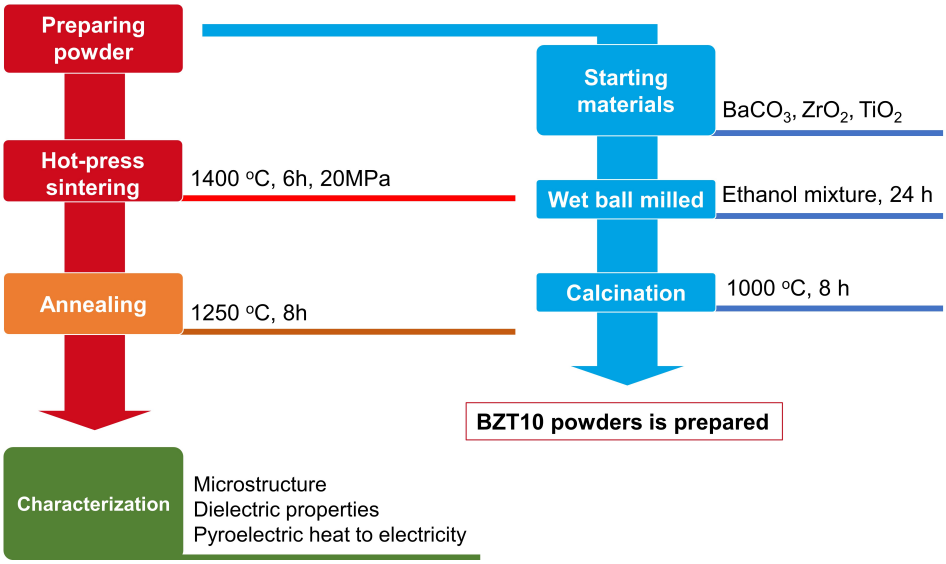

Figure 4.1: Synthesis and evaluation flow of BZT10 sample

The calcination process was performed in air at 1000 ℃, 5 ℃/min step, for 8 hours. The as-calcinated powders were ground again prior to the sintering process with the hot-press method (Fujidemba FVPHP-R-5 FRET-18). During this process, the fine powders were placed in a ϕ44 mm graphite mold covered with a 0.2 mm-thick carbon sheet to prevent adhesion. The sintering happened first at 500 ℃ to remove all the contamination and go to 1400 ℃ with the step of 20 ℃/min, and kept for 6 hours under a vacuum environment. From 500 ℃, a 0.7 MPa/min load was applied up to the maximum of 20 MPa axially to the mold. After that, the as-sintered samples were cut into 8 square plates, with 14 mm in length, and ground to 1 mm in thickness using the nano cutter and nano grinder respectively. The 1 mm thick samples were then annealed in air at 1250 ℃, 5 ℃/min step, for another 8 hours.

Figure 4.2: Hot-press sintering machine

4.1.3 Microstructure and dielectric properties evaluation

Microstructure

X-ray diffraction (XRD, Rigaku RINT-2500HF+/PC) analysis, in $\theta/2\theta$ configuration from 20° to 80°, 1 °/min, 0.01° step, was performed to identify the main crystalline phases of the BZT10 sample after each heating process: calcination, sintering, and annealing.

Additionally, Field emission-scanning electron microscopy (FE-SEM, JEOL JSM-6700F) was used to observe the as-annealed and as-sintering sample's surface and fracture structure. The samples were mirror-polished using sandpaper 100, 240, 600, 1200, and 9 μm, 1 μm diamond slurry. Afterward, the sample surface was coated with osmium to prevent charge-up. The energy-dispersive X-ray spectroscopy (EDS) in point mode was performed to confirm the homogeneity of the fabricated sample.

(a) RINT-2500HF+/PC (b) JEOL JSM-6700F with EDS

Figure 4.3: XRD and FE-SEM with EDS function for microstructure evaluation

Finally, the planimetric procedure in American Society for Testing and Materials (ATSM) standard E112 was used to determine the average grain size of the as-annealed samples from a total of 1737 grains.

Dielectric properties

Sample preparation Prior to the dielectric measurement, the BZT10 sample was ground to 0.8 mm with the nano grinder. The gold electrode

was attached to both sides of the sample using the gold sputtering (Sanyu Electron, SVC-720) in the area of 12 x 12 mm. Afterward, a polling process happened in silicone oil under a DC electric field of 3000 kV/m at 80 ℃ for 30 minutes.

Dielectric constant measurement The dielectric constant curve of BZT10 samples was measured using an impedance analyzer (NF Corporation, ZGA5920) at four frequencies 100 Hz, 1 kHz, 10kHz, and 100 kHz. The temperature condition was controlled using an electric furnace at a heating rate of 2 ℃/min. Prior calibration was performed to ensure adequate temperature recording.

Figure 4.4: Impedance analyzer for dielectric constant measurement

The relative permittivity was calculated using equivalent capacity C_P and resistance R_P of the sample, with an assumptive vacuum capacitance C_0 (same area S and thickness d with the measured sample but have the vacuum permittivity ϵ_0). Therefore, the value of vacuum capacitance C_0 was calculated as:

$$C_0 = \epsilon_0 \frac{S}{d \times 10^3} \tag{4.1}$$

Consequently, based on the measured value of the equivalent C_P and R_P, the complex permittivity ϵ and dielectric loss $\tan\delta$ are calculated as the following:

$$\epsilon' = \frac{C_P}{C_O} \tag{4.2}$$

$$\epsilon'' = \frac{1}{2\pi f C_0 R_P} \tag{4.3}$$

$$\epsilon = \sqrt{\epsilon'^2 + \epsilon''^2} \tag{4.4}$$

$$\tan\delta = \frac{\epsilon''}{\epsilon'} \tag{4.5}$$

Where ϵ' and ϵ'' is the real and imaginary parts of complex permittivity respectively, and f is the frequency.

D-E hysteresis loop The D-E hysteresis loop of BZT10 samples was performed using a general Sawyer–Tower circuit in silicone oil media (Fig. 4.5). An AC electric field of 1250 kV/m, 0.05 Hz was applied using the function generator (NF Corporation, WF1974) and high-voltage amplifier (TREK, 677 B), and hot plate (As One, HP-2SA) to raise the temperature to the appropriate condition for the experiment. The temperature, input voltage, and voltage of the mirror capacitor were monitored using a scope re-coder (YOKOGAWA, DL850E).

The dielectric displacement D and electric field E was calculated as the following:

$$D = \frac{CV_C}{A} \tag{4.6}$$

$$E = \frac{V_i}{d} \tag{4.7}$$

where C and V_C is the capacitance and voltage of the mirror capacitor, V_i is the input voltage, and d is sample thickness.

4.2 Result and Discussion

4.2.1 Microstructure

XRD patterns of the BZT10 samples after each synthesis process are shown in Fig. 4.6. After calcination, a minor peak corresponding to the $BaZrO_3$

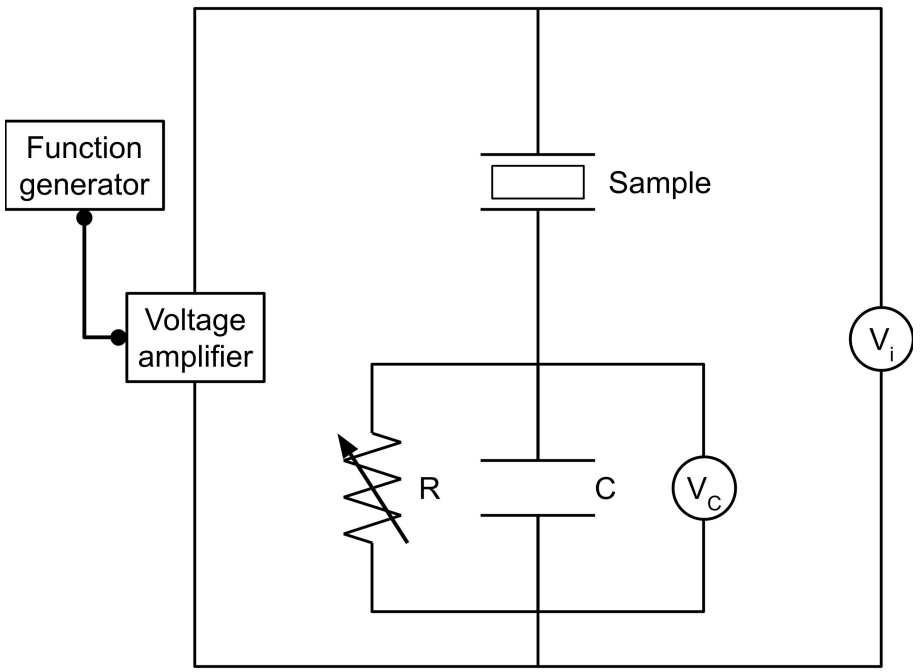

Figure 4.5: Schematic drawing of D-E hysteresis loop measurement circuit

secondary phase was observed. However, it disappeared after the sintering and annealing processes at higher temperatures of 1400 and 1250 °C, respectively. Therefore, the as-sintered and as-annealed sample consisted of a single BZT10 main phase. Furthermore, the peak positions suggested a perovskite structure with an left-right asymmetric main peak (inset figure) indicating coexistence of tetragonal and rhombohedral crystal system. This result agreed well with the results reported by Dong et al. [147]. Since the combination of tetragonal and rhombohedral phases is an important phase that induces the relaxor transition in ferroelectric, successful synthesis of the BZT10 sample in such phase is needed for a potential high-power generation ability.

Fig. 4.7a and 4.7b shows the FE-SEM fracture image of as-sintered and as-annealed BZT10 respectively. Fig. 4.7c shows the FE-SEM surface image of the as-annealed sample. From Fig. 4.7a and 4.7b, the BZT10 sample was synthesized as a high-density bulk material without any porosity. The pore observed in the surface of the BZT10 sample in Fig. 4.7c might come from the polishing process.

The composition analysis with EDS is shown in Fig. 4.8. From the result, the Ba and Zr peaks were observed. Although the Ti peak overlaps with the Ba peak, the peak position and the full width half maximum value suggested the existence of Ti in the grain. Since all three elements: Ba, Zr, and Ti were observed in one grain, the solubility of the reactive oxides as well as the formation of one main phase in the sintered and annealed BZT10 samples was confirmed.

Although there is no difference in the microstructure of the bulk sample after sintering and annealing, a color change from black to white was observed, as shown in Fig. 4.9. The color change is explained by the oxygen vacancy, corresponding to the black color of the sample, and was formed during sintering with a graphite mold under vacuum conditions. After the annealing process in air, the oxygen vacancy was replenished, and samples turned to the typical ceramic's white color.

The average grain diameter of the BZT10 sample was calculated to be $d = 4.5\ \mu$m.

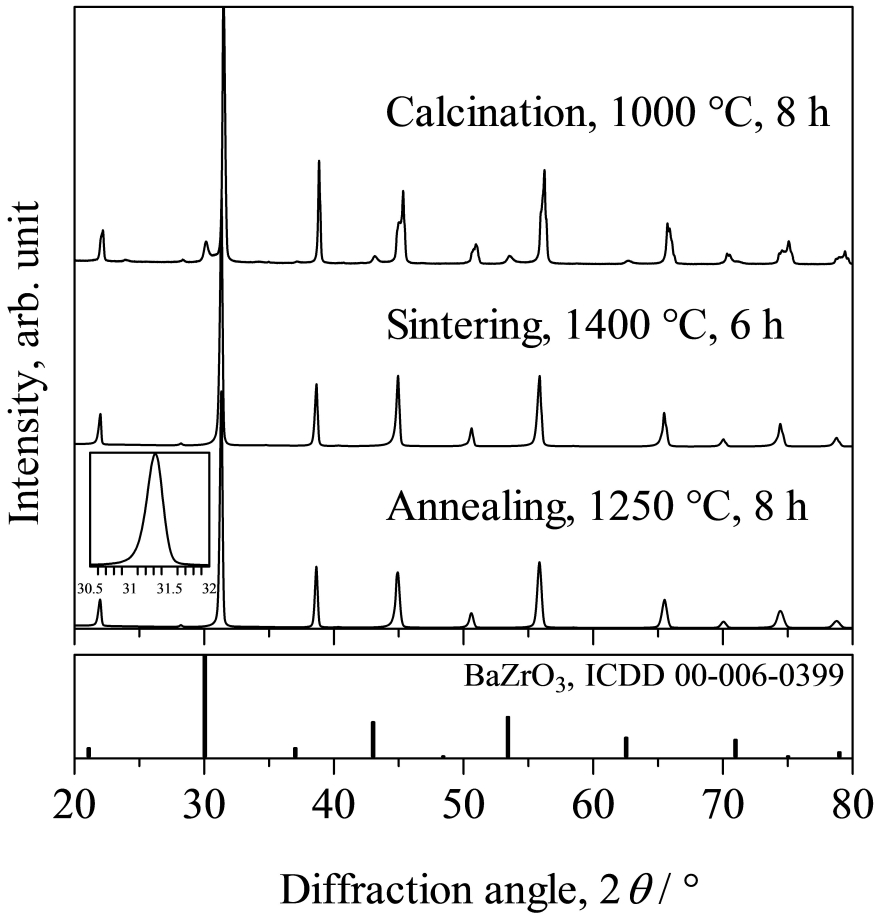

Figure 4.6: XRD pattern of BZT10 indicating a single rhombohedral main phase

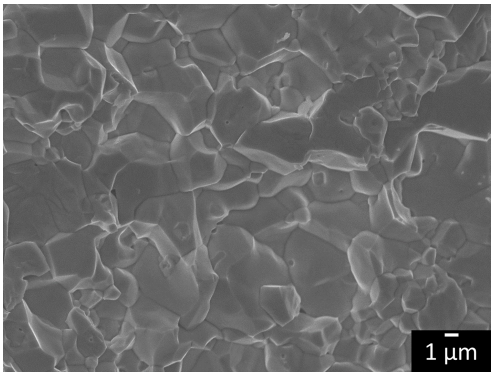

(a) Fracture image - As-sintered

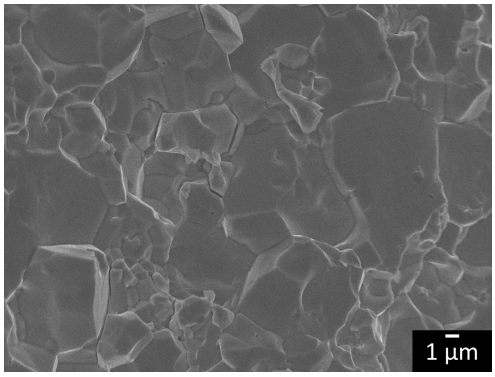

(b) Fracture image - As-annealed

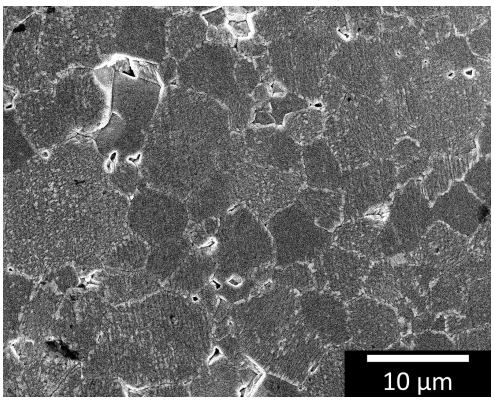

(c) Surface image - As-annealed

Figure 4.7: FE-SEM observation of BZT10 samples

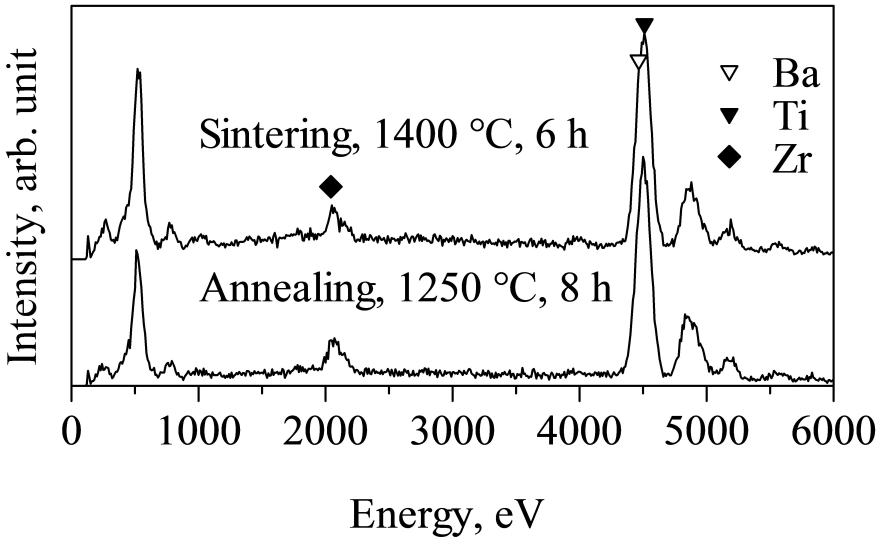

Figure 4.8: EDS pattern of as-sintered and as-annealed BZT10 sample

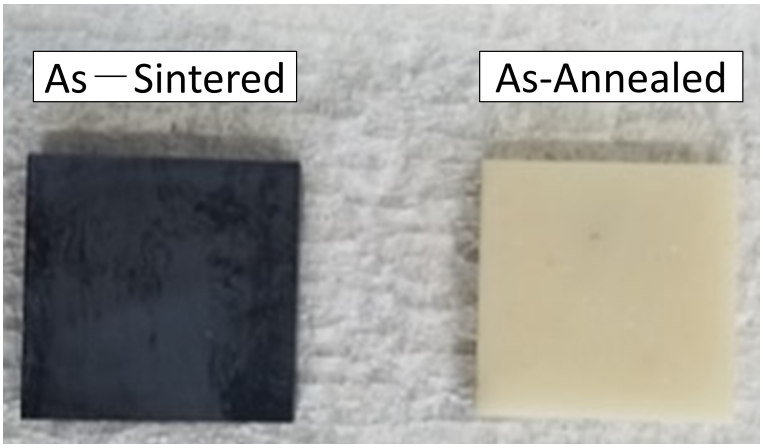

Figure 4.9: Color change in BZT10 sample before and after annealing process

4.2.2 Dielectric properties

The temperature-dependent relative permittivity of the BZT10 sample at different frequencies is shown in Fig. 4.10. The dielectric constant curve for the BZT10 sample shows a single broad peak with a maximum value of 8530 at the Curie temperature 105 for the frequency of 1 kHz. The maximum value and the obtained temperature shifted to the right side of the temperature axis with the increase of measured frequency corresponding to a relaxor phase transition. At 100 Hz, the relative permittivity of the materials reached a maximum value at a Curie temperature of 105 ℃. The relative permittivity peaks shifted toward higher temperatures as the frequency increased. At 10 kHz, the relative permittivity peak was at 110 ℃. The suggested phenomenon indeed was a mix-relaxor-ferroelectric behavior. The replacement of Ti^{4+} with Zr^{4+} in the BZT10 induced the off-centering characteristic of B-site ion in the ABO_3 crystal structure. As a result, the PNRs formed, leading to a weak mix-relaxor-ferroelectric behavior observed in the composition. The behavior was also reported by other researchers [135–137]. Above the Curie temperature, the BZT10 transited to the paraelectric phase maximizing the relative permittivity.

Fig. 4.11 shows the dielectric loss of BZT10 sample. From 70 ℃, the dielectric loss curve at 100 Hz, 1 kHz, and 10 kHz slowly decreases due to the transition of the ferroelectric phase to the relaxor phase. However, at 100 kHz, a dielectric loss peak at 110 ℃ was obtained. At high frequencies, the random PNRs of the relaxor phase received enough energy for polarization, as a result, a sharp relaxor to paraelectric transition was observed as shown in the case of 100 kHz.

Fig. 4.12 shows the hysteresis loop of the BZT10 sample at different temperatures. At room temperature, the BZT10 sample exhibit a slim hysteresis loop with small coercive field $E_c = 178$ kV/m and remanent polarization value $P_r = 4.7\mu C/cm^2$ due to the mix relaxor-ferroelectric phase. The hysteresis loop became slimmer with the increase in temperature, exhibiting a high change in polarization at 70 ℃. The variation of remanent polarization ΔP_r and saturated polarization ΔP_s were 0.8 and 1.1 $\mu C/cm^2$ respectively. This temperature is also reflected in the dielectric loss curve whereas the value continuously drops, corresponding to the gradual transition of the remaining ferroelectric phase to the relaxor phase. Further increase in temperature

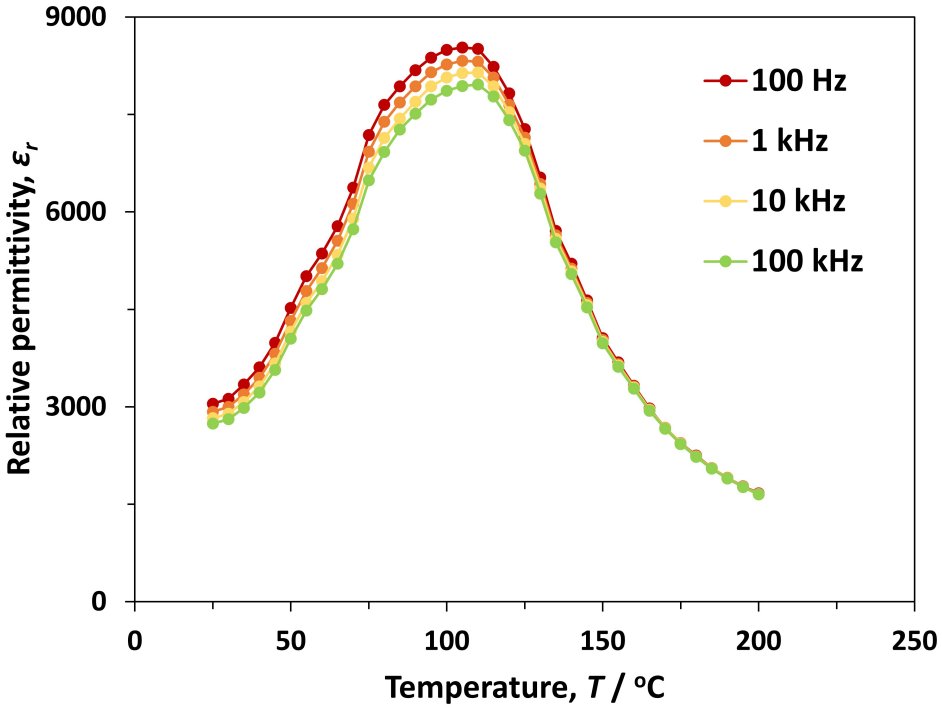

Figure 4.10: Diffusive behavior corresponding to a mix relaxor-ferroelectric phase in the temperature-dependent dielectric constant curve of BZT10 sample

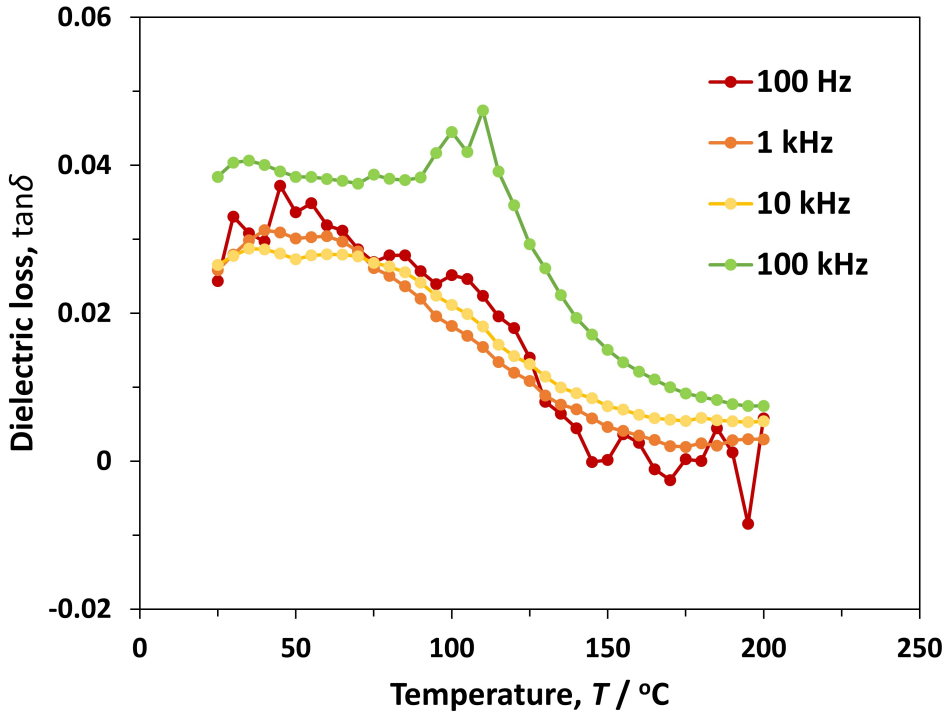

Figure 4.11: Dielectric loss as a function of frequencies of BZT10 sample

turned the hysteresis loop into a slimmer shape with the remanent polarization, and the coercive field continuously decreased. An average variation of 0.60 μC/cm^2 in the sample's remanent polarization and 0.83 μC/cm^2 in spontaneous polarization for each 10 ℃ was observed. At 110 ℃, the loop turned into a non-linear slim shape of the paraelectric phase as observed in the dielectric constant curve and dielectric loss curve at 110 ℃.

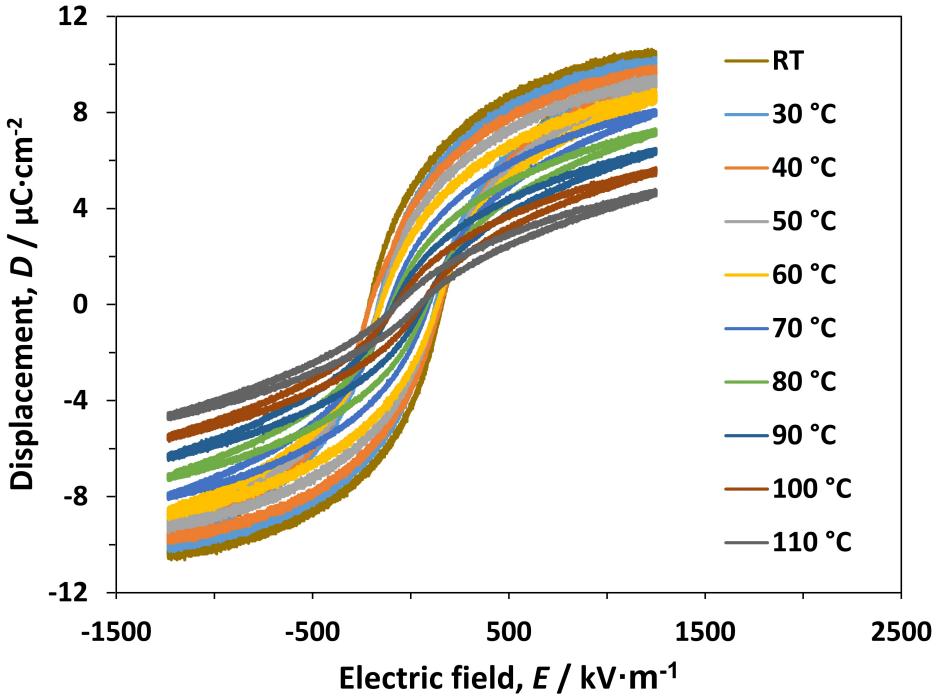

Figure 4.12: D-E hysteresis loop at different temperatures of BZT10 sample

4.2.3 Summary

The BZT10 sample in this chapter was successfully fabricated to the perovskite rhombohedral structure using the solid-state reaction and hot-press sintering. The evaluation of dielectric properties reveals the mix-ferroelectric-relaxor behavior with a diffusive phase transition, low remanent polarization, and low coercive field. At 70 ℃ the remaining ferroelectric phase starts to transit to the relaxor, causing a large drop in remanent and saturated polarization,

and finally, at Curie temperature of 110 ℃ the sample exhibit a transition to the paraelectric phase maximized the relative permittivity.

Chapter 5

Pyroelectric heat to electricity of lead-free BZT10 in a simulated no cooling-assisted fluctuating heat source

5.1 Electrothermodynamic cycle

Pyroelectric materials convert heat to electricity based on the pyroelectric effect calculated using Eq. 3.6. However, the efficiency during this process is very low, to be less than 1% as reported by Fatuzzo et al. [148], van der Ziel [149] and Frood [150]. The actual measurement showed an even more problematic result, as less than 0.1 mW/cm^3, corresponding to 0.001% of the energy was converting back to electricity [151, 152]. Therefore, an electrothermodynamic cycle, which shares the same concept as the thermodynamic cycle in a heat engine, has been developed as a solution. Different from the heat engine cycle that uses temperature and pressure, the pyroelectric cycle was a combination of an electric field application and pyroelectric effect inducing temperature fluctuation. The electric field application accounts for the increase of orientated domain at the beginning; and due to the effect of pyroelectricity, these oriented domain switches efficiently to extract a large amount of electricity. Multiple cycles utilize different combinations of isothermal, isoelectric, isodisplacement, etc. studied by Olsen et al. as shown in Fig. 5.1. However, due to the difficulty of realizing the adiabatic process, the

Carnot cycle for ferroelectric still see no report which is a big limitation of the field in term of efficiency improvement.

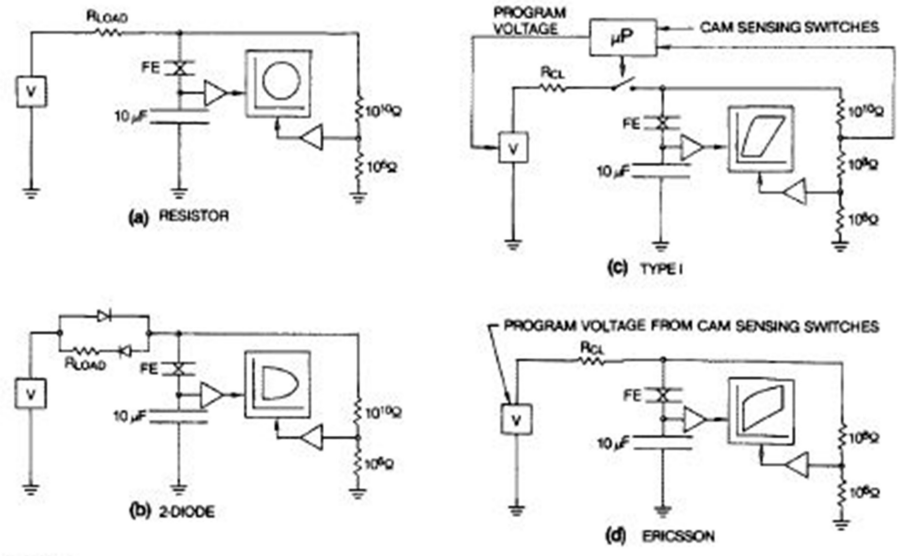

Figure 5.1: Electric circuit and the measured cycles

Among all the cycles, the Ericsson mimic ones (named "Olsen cycle") are the most efficient which can theoretically improve the 1% efficiency to the maximum of 80% of the Carnot efficiency under ideal conditions [153–155]. The Olsen cycle consists of four steps, with timing corresponding to each temperature variation state. The first isothermal step occurs as the materials reach the temperature T_L. A constant external electric field E_H is applied, and the electric field-displacement characteristic of the material changes following the hysteresis loop at the respective temperature. Next, the temperature increases while maintaining the electric field E_H, and the displacement decreases owing to the pyroelectric effect. Subsequently, the step moves to high-temperature isothermal. As the temperature reaches the desired T_H value, the external field is reduced to a lower value. The displacement decreases with a mechanism similar to that in Step 1. Finally, the material is cooled back to the temperature T_L, and the displacement returns to its original value. The conversion energy is corresponding to the closed area of the four steps and is described by Eq. 5.1.

$$N_D = \oint E\, dD \tag{5.1}$$

where N_D is the converted energy density, E is the electric field, and D is the dielectric displacement of the element respectively. Fig. 5.2 shows the Olsen cycle loop with the timing of electric field application, temperature fluctuation, pyroelectric current, and change in polarization.

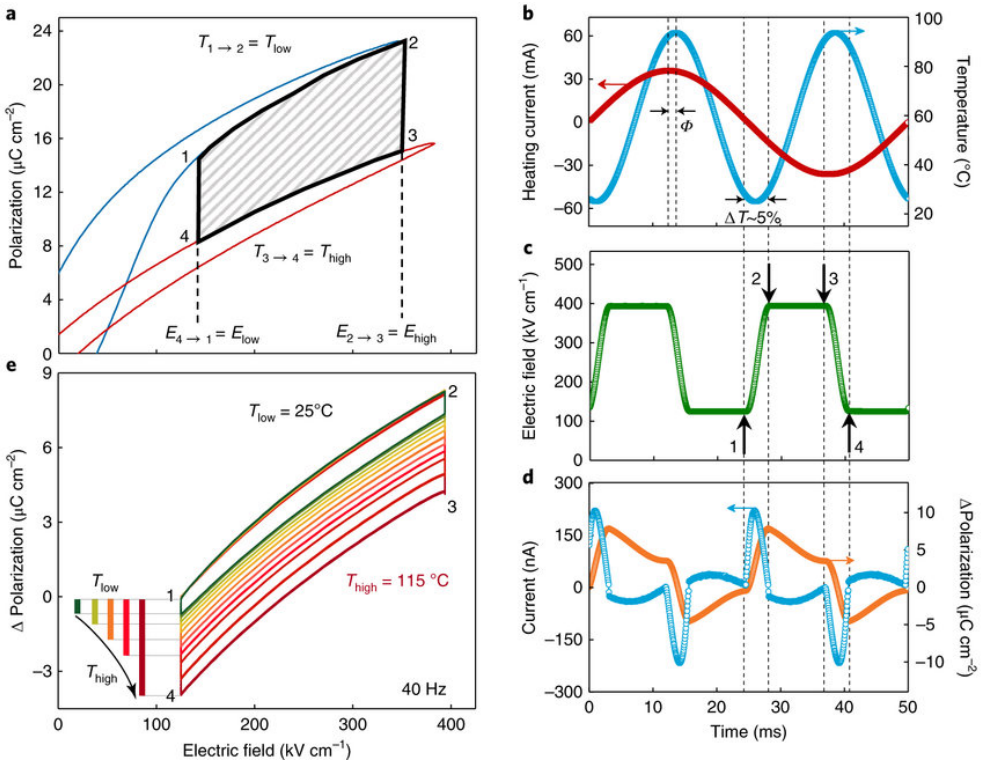

Figure 5.2: Olsen cycle for pyroelectric heat to electricity [79]. a) A schematic for four steps of the Olsen cycle. b) Temperature variation due to current heating. c) Electric field application. d) Pyroelectric current and change in polarization. e) Olsen cycle loop at different fluctuating heat sources

The second best cycle was the type I mimicked the Stirling cycle in the heat engine. Two isothermal steps remain the same as in the Olsen cycle, and two isoelectric steps are replaced with two isodisplacement steps. In detail, the first isothermal works by increasing the displacement of the material to

a value D_H. In sequence, the material disconnects from the circuit, keeping the displacement value constant, and the electric field further increases to E_H owing to the effect of pyroelectricity. The following high-temperature isothermal step occurs with a discharge process to reduce the displacement to D_L. Finally, the material cooling in the electrically isolated condition causes the electric field to return to the start value E_L. Fig. 5.3 shows the four steps with the D-E loop of the Stirling cycle.

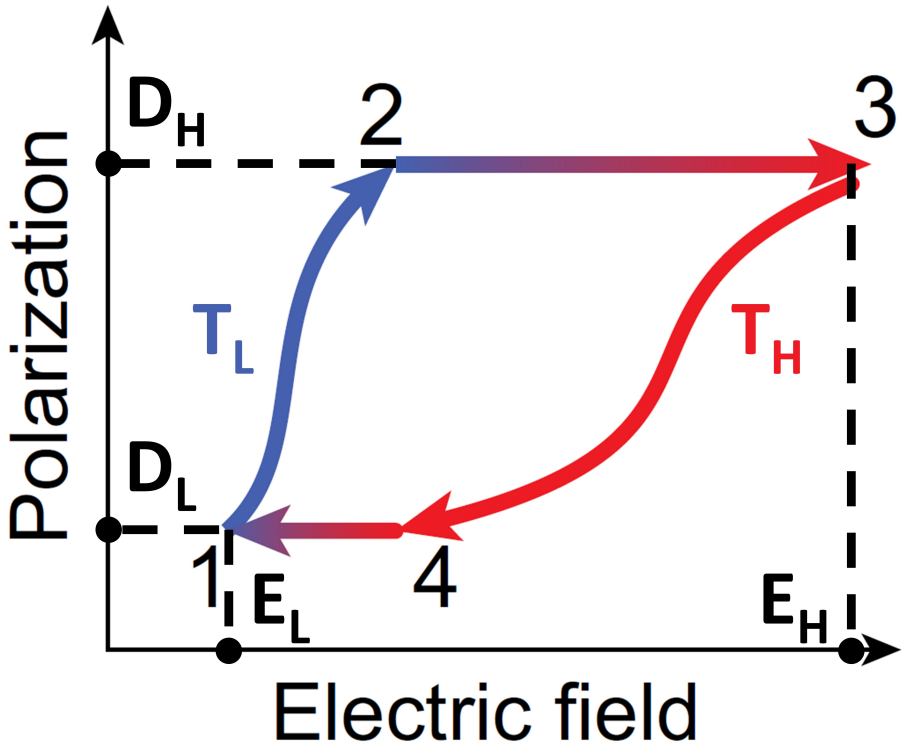

Figure 5.3: Stirling cycle [156]

However, in 2015, Kim et al. developed a new electrothermodynamic cycle that can generate electricity more efficiently from the fluctuating heat source than the Olsen and Stirling cycle [157]. The cycle is a hybrid combination of the Olsen and Stirling cycles, taking the advantage of the low-to-high-temperature isodisplacement process in Stirling and high-to-low temperature isoelectric in the Olsen cycle. Fig. 5.4 shows the mechanism for generating higher power in the Kim cycle.

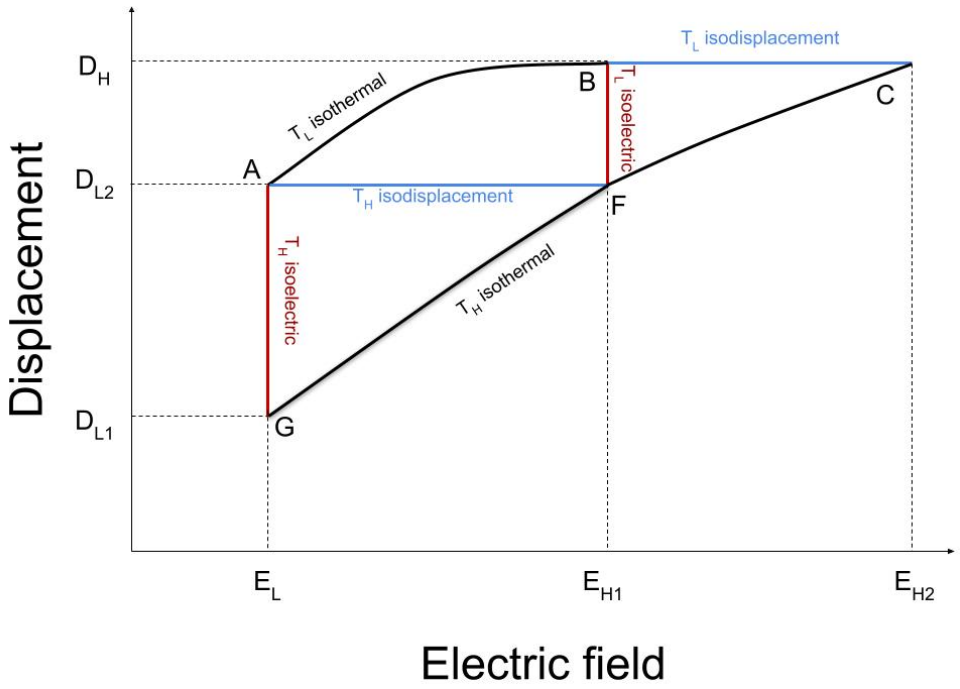

Figure 5.4: Kim cycle utilizing isodisplacement process in Stirling and isoelectric in Olsen cycle for efficient electricity generation

Although Olsen and Stirling's cycles share the same area of ABF as generated energy, the Olsen cycle contains the AFG loop area that takes advantage of the cooling isoelectric step, while the Stirling cycle includes the BFG area generated by the rise of the electric field during isodisplacement process. Kim cycle comprises the specialty of both, and theoretically generates energy from the area ABCG. In an experiment with an actual heat fluctuating heat source, the cycle converts heat to electricity at an efficiency of 0.0034% higher than the 0.0025% of the conventional Olsen cycle in the same condition.

5.2 Factor affect heat to electricity conversion in pyroelectric material

The electrothermodynamic cycle was developed to raise the heat-to-electricity conversion efficiency of the ferroelectric materials and accomplished its mission. However, the current efficiency is still the biggest limitation for the application

of such a system. Therefore, current progress on pyroelectric energy harvesting trying to raise the efficiency in multiple different aspects. Among that, materials development should focus on two major significant factors that affect an efficient pyroelectric heat to electricity: 1) Thermodynamic properties and 2) Electrical properties. Each corresponds to of electrical and thermal process in the conversion cycle

5.2.1 Electrical factor

Primary factor - Dielectric constant and Polarization

The electrothermodynamic cycle generates electricity based on the variation of the D-E loop. More specifically, the maximum potential for the Olsen cycle was generated by the difference between the high-temperature and low-temperature D-E hysteresis curve. Therefore, the reduction in saturated and remanent polarization is important for this cycle. On the other hand, the Kim cycle replaces the heating isoelectric step with an isodisplacement process. The generated energy is based on the change of remanent polarization and the electric field increase by the mean of the pyroelectric effect. The electric field raised during this process can be calculated using the Eq. 5.2

$$\frac{\partial E}{\partial t} = -\frac{\pi}{\epsilon}\frac{\partial T}{\partial t} \tag{5.2}$$

where π is the pyroelectric coefficient, ϵ is the dielectric permittivity, T is temperature and t is time.

Another factor is the dielectric constant value of the materials. As explained in the earlier section, the dielectric constant induces loss by raising the necessary energy for orientating the dipoles. Additionally, as observed in Eq. 5.2, the dielectric constant ϵ is inverse proportionality to the electric field raised during the isodisplacement process. The drawback also reflected in the pyroelectric figure of merit as shown in Eq. 5.3

$$FoMs = \frac{\pi^2}{\epsilon} \tag{5.3}$$

where $FoMs$ is the figure of merit abbreviation. Therefore, a low dielectric constant should be expected, and the broad peak of the relaxor phase should be ideal for the conversion.

In conclusion, polarization, more specifically polarization change as temperature, is the important factor for efficiency, and factors that would affect the polarization should be clarified.

Secondary factor - Leakage current

The leakage current is generated due to the internal resistance of the materials. For an applied electric field E, the leakage current can be calculated as:

$$I_{Leak} = \frac{Ed}{R_{Int}} \tag{5.4}$$

where I_{Leak} is the leakage current, d is the sample's thickness, and R_{Int} is the internal resistance of the material. Therefore, the displacement drop can be calculated as:

$$D_{Drop} = \frac{1}{A}\int I_{Leak}\,dt \;= \frac{1}{A}\int \frac{Ed}{R_{Int}}\,dt \;= \frac{d}{AR_{Int}}\int E\,dt \tag{5.5}$$

with D_{Drop} is the displacement drop, A is the area and t is time. The effect of leakage current is hard to observe in the Olsen cycle since the displacement drop during the isoelectric process. However, in the Kim cycle, during the isodisplacement, the observed loop is smaller than the theoretical as shown in Fig. 5.5.

5.2.2 Thermal factor

Primary factor - Heat conductivity

For a sample with volume S, mass m, density ρ the necessary heat Q (J) to increase the temperature T of the sample is:

$$Q = m \times C_p \times \Delta T_1 = \rho V \times C_p \times \Delta T_1 \tag{5.6}$$

If the heat has the constant power of P (W) the process will take the time t

$$t_1 = \frac{Q}{W} = \rho V \times C_p \times \frac{\Delta T_1}{W} \tag{5.7}$$

to reach the desired temperature. However, in reality, the heat is only contacting with the surface of the sample, which causes the process to take more time due to the thermal conductivity k. The time due to heat conductivity is:

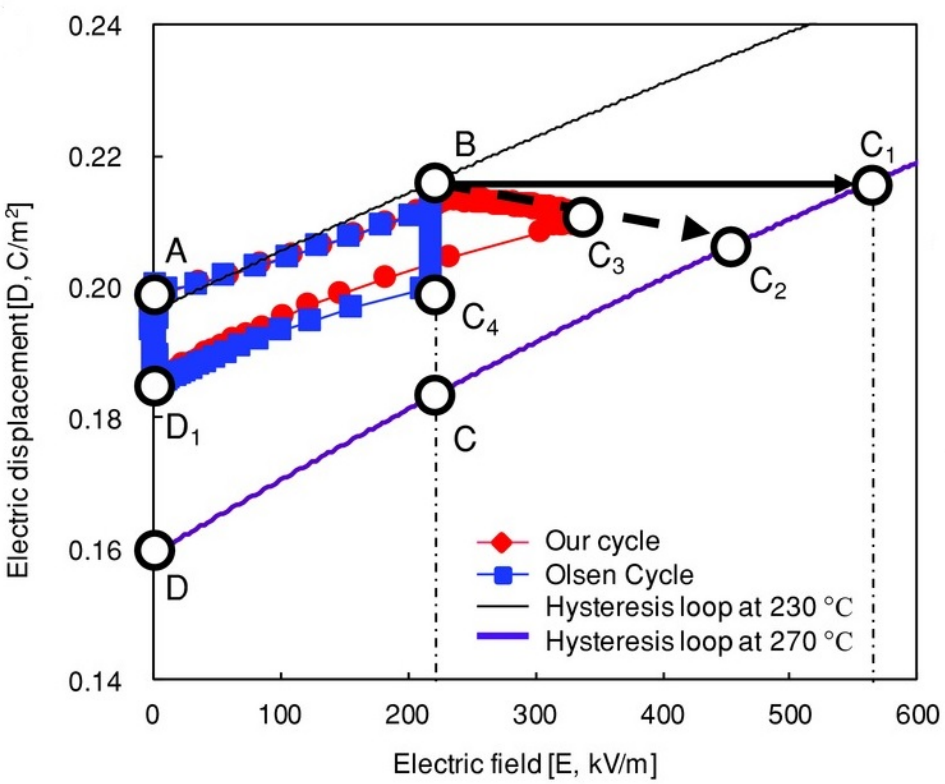

Figure 5.5: Theoretical and practical Kim cycle loop [157]

$$t_2 = \frac{1}{k}\frac{d}{A}\frac{Q}{\Delta T_2} = R_\theta \frac{Q}{\Delta T_2} \tag{5.8}$$

where d is the thickness, A is the area of the sample, Q is the heat flow, T_2 is temperature difference between surface and the internal, and $R_\theta = \frac{d}{k \cdot A}$ is the absolute thermal resistivity.

The effect of heat resistivity caused an in-homogeneous distribution all over the sample, causing a drop in the measured cycle loop as reported by Lee et al. [158] and Siao et al. [159].

Secondary factor - Heat expansion

As the sample was placed in a heat source, and its temperature increased, the sample exhibited volume expansion [160, 161]. As a result, the piezoelectric effect that we discussed in chapter 3, section 1 occurs, which is considered the secondary pyroelectric effect. The secondary pyroelectric coefficient of the rhombohedral crystal was determined using Eq. 5.9 [162, 163].

$$\pi_{sec} = 2d_{31}(c_{11}\alpha_1 + c_{12}\alpha_2 + c_{13}\alpha_3) + d_{33}(2c_{13}\alpha_1 + c_{33}\alpha_3) \tag{5.9}$$

where π_{sec} corresponds to the secondary pyroelectric coefficient, d is the piezoelectric coefficient, α is the coefficient of thermal expansion, and c is the elastic stiffness constant.

Up to date, the direction reported for the secondary pyroelectric effect is different for materials. It was reported to be negative (opposite to the primary ones) in $BaTiO_3$; however, being positive in lead-based PMN-PT. Although the value was reported to be significantly low, it might take as an important factor in enhancing or obstructing the heat-to-electricity conversion in the pyroelectric materials, especially at high applied voltage, and temperature.

5.3 Single heat source configuration for pyroelectric energy harvesting

5.3.1 Objectives

Pyroelectric generates electricity from a fluctuating temperature, which makes its biggest advantage to be able to operate with a single heat source. In

addition to that, the cooling system is also applicable, enhancing the output for high-power consume devices. Fig. 5.6 shows some heat source configurations for pyroelectric energy harvesting.

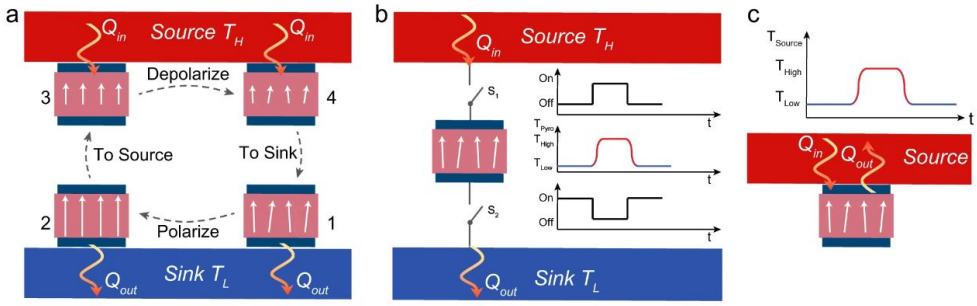

Figure 5.6: Heat source configurations for pyroelectric energy harvesting [156]. a) Mechanical rotation system to induce heat fluctuation, and allow multiple sample work. b) Cooling-assisted system for high output energy. c) Operation under a single fluctuating heat source.

In this chapter, we discuss the pyroelectric ability of the BZT10 sample for usage with a single fluctuating heat source (low-temperature span, different frequencies). And in chapter 6, the configuration adapts high-temperature span, corresponding to the cooling-assisted system will be investigated.

Four D-E loops corresponding to the four different processes are necessary to enclose the loop area. The D-E loops during the isothermal process strongly depended on the temperature at which the step occurred. In contrast, the isoelectric and isodisplacement (two isoelectric steps for the Olsen cycle) were appropriate for the temperature fluctuation-pyroelectricity of the materials. Because natural waste heat is in various forms with different combinations of temperature ranges and frequencies, it is necessary to understand these aspects of the temperature factor on the conversion ability of the material and optimize the application of the cycle according to the features of each parameter. Therefore, firstly we will investigate the effect of thermal and electrical factors on the power generation ability of BZT10 samples at different heat spans and fluctuating frequencies. Secondly, from the obtained results, we suggested an appropriate sample design with thicknesses and efficiency-boosting using a circuit with an electric field application.

5.3.2 Novelty

Although being able to operate with a single fluctuating heat source is the biggest advantage of pyroelectric materials, the conventional test with a lead-free system neglected the merit and calculated a meaningless energy density from significant high and low constant temperature hysteresis loops. The experiment ignored the adaptability of materials in such conditions and the energy cost of a refrigeration system to reach the significantly low temperature which is impractical in most of the application scenes.

Therefore, in this thesis instead of focusing on the meaningless significant high energy density with the impractical design, we investigate the BZT10's pyroelectric conversion using a single fluctuating heat source setup. The result enables deep studies on electrical and thermal factors in each aspect of the isothermal, isoelectric, and isodisplacement processes of the electrothermodynamic cycle. Furthermore, the investigation allows a reliable design of the sample and circuit toward application with a single heat source used for optimized conversion efficiency.

5.4 Experimental

The power generation ability of the samples was evaluated using the Kim cycle and Diode and Switches circuit (DSW circuit). The circuit was based on the Sawyer–Tower circuit, but a diode D and two switches SW1 and SW2 were added, as shown in Fig. 5.8a. A heat fluctuation was created by controlling two cylinder motor-controlled shutters (Oriental Motor, ELECM4E10MK-AP) covering or uncovering two heat guns (Leister, HOTWIND SYSTEM), running at different temperatures located on two sides of the sample. The plus side of the sample was partially painted with a black body spray and measured the temperature using a radiation thermosensor (Keyence, FT-50A). The experimental configuration of the sample setting and heat gun operation is shown in Fig. 5.7.

The schematic drawing of the DSW circuit is shown in Fig. 5.8 with the timing of switches, applied electric field, and element's temperature.

The Kim cycle consists of four steps, heat guns, and cycle loop work as follows:

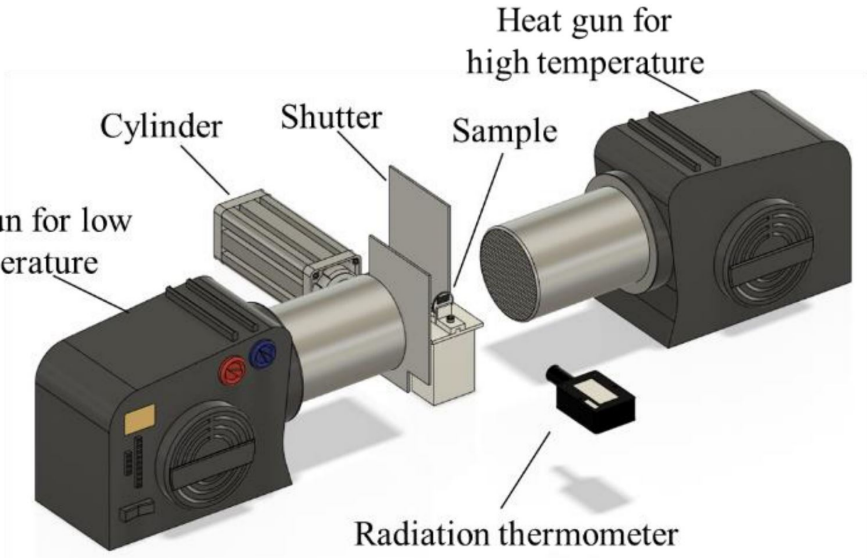

(a) Overview

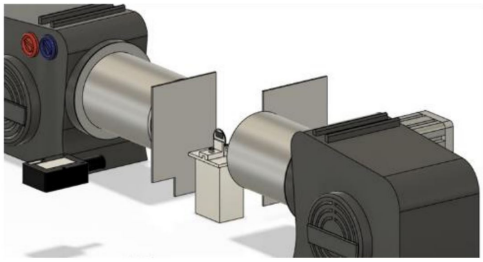

(b) Shutter covers high-temperature side

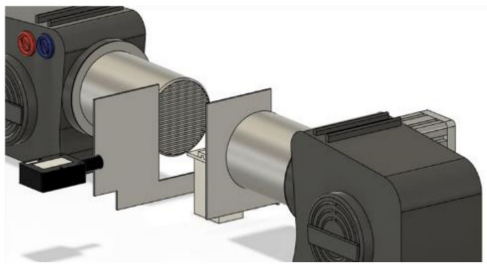

(c) Shutter covers low-temperature side

Figure 5.7: Experimental configuration of sample setting and heat gun operation

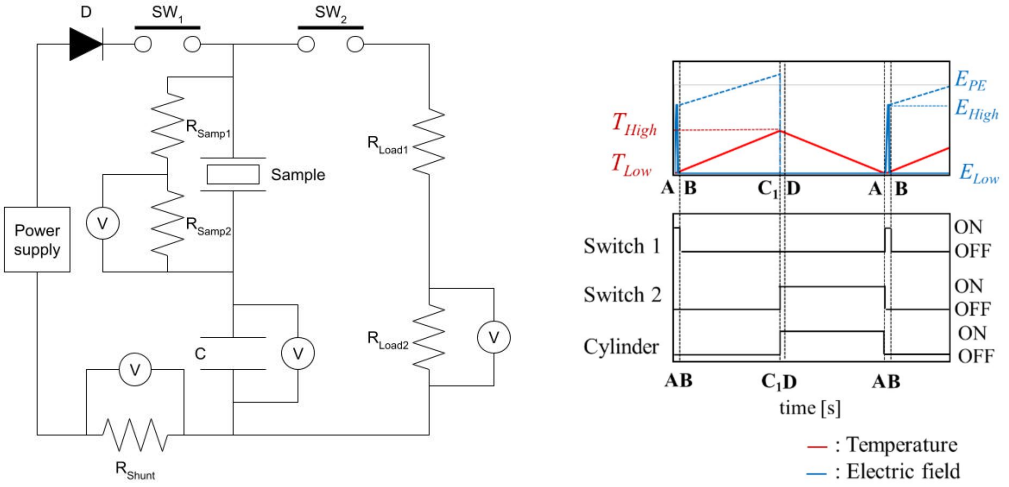

(a) DSW circuit (b) Parameter timing

Figure 5.8: The schematic drawing of the DSW circuit

- **Step 1 (A → B)**: When the sample temperature reaches T_L, SW1 is closed, SW2 is opened, and an electric field $\overrightarrow{E}$ is applied to the sample for 0.3 s. The sample D–E loop at this time is the curve at temperature T_L.

- **Step 2 (B → C)**: The temperature of the sample is gradually increased from T_L to T_H by using shutters to uncover the high-temperature side and cover the low-temperature side heat guns. Both SW1 and SW2 are opened, and the sample is kept in an electrically isolated state. The sample's electric field continues to increase due to the pyroelectric effect, as shown in Eq. 5.2.

- **Step 3 (C → G)**: When the temperature of the sample reaches T_H, SW1 is opened, and SW2 is closed. The energy stored in the sample is quickly discharged to resistors R_{Load1} and R_{Load2}. The sample D–E loop at this time is the curve at temperature T_H.

- **Step 4 (G → A)**: The sample's temperature gradually decreases from T_H to T_L by uncovering the low-temperature side and covering the high-temperature side heat guns with shutters. SW1 remains open and SW2 remains closed during this step.

The energy density N_D was calculated using the D–E loop area enclosed by the four steps of the Kim cycle. However, the power density was calculated with the load resistance to investigate the practical potential of the sample in the application.

$$P_{out} = (\frac{V_R}{R_{Load1}})^2(R_{Load1} + R_{Load2}) \tag{5.10}$$

BZT10 samples were ground to different thicknesses of 0.8 mm, 0.7 mm, 0.6 mm, 0.5 mm, and 0.4 mm, and the power generation ability of each sample was evaluated at two temperature ranges ΔT = 20 ℃, 40 ℃ and three different frequencies f = 0.05, 0.067, 0.1 Hz.

5.5 Power generation as a function of fluctuating frequency

Fig. 5.9 shows the cycle loop and Fig. 5.10 shows the energy and power density calculated using Eq. 5.1 at 2000 kV/m electric field application of the three frequencies.

As the fluctuating frequency increases, the cycle loop shrinks in the displacement axis but expands in the electric field axis. The different areas between the two hysteresis loops at low and high temperatures decreased due to the effect of heat conduction reducing the internal temperature adaptability of the sample. Assuming the value $\Delta T = T_H - T_L$ in Eq. 5.8 is constant, as the frequency increase, the time for heat conduction would be less. As a result, the total amount of heat Q transferred to the T_L side is reduced. Substitute this to the Eq. 5.6, and the change of temperature will decrease.

Therefore, the rise of internal temperature due to heat conductivity will be lower with the increase of fluctuating frequency. As a result, a higher frequency cycle correlated with the cycle area of the low-temperature side, resulting in a smaller cycle area. This phenomenon significantly affected ferroelectric materials in the high-temperature range since the thermal conductivity constant is also a temperature-dependent parameter [157, 164, 165]. Based on this phenomenon, increasing the fluctuation frequency beyond a

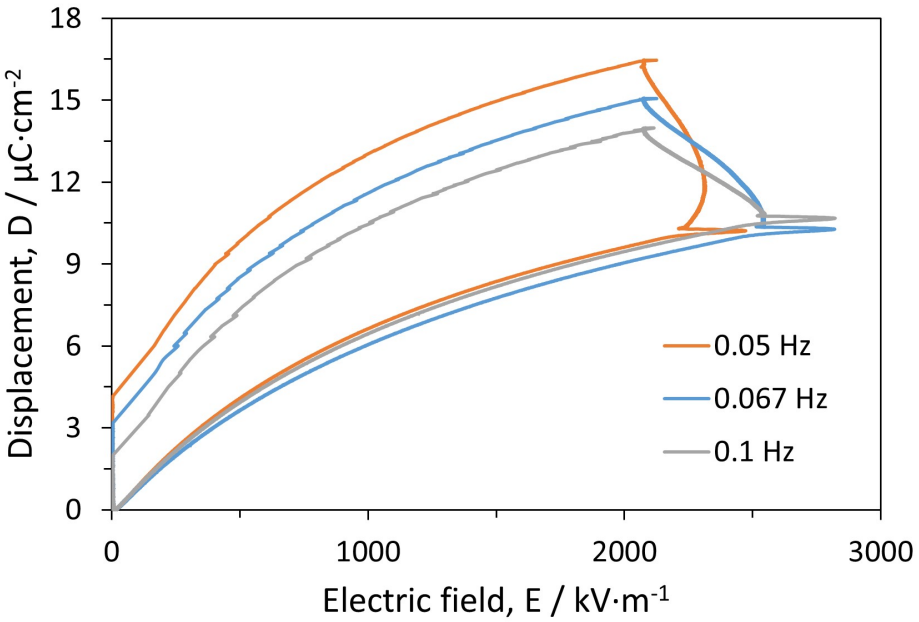

Figure 5.9: Cycle loop of the BZT10 samples at three different frequencies: f = 0.05 Hz, 0.067 Hz, and 0.1 Hz.

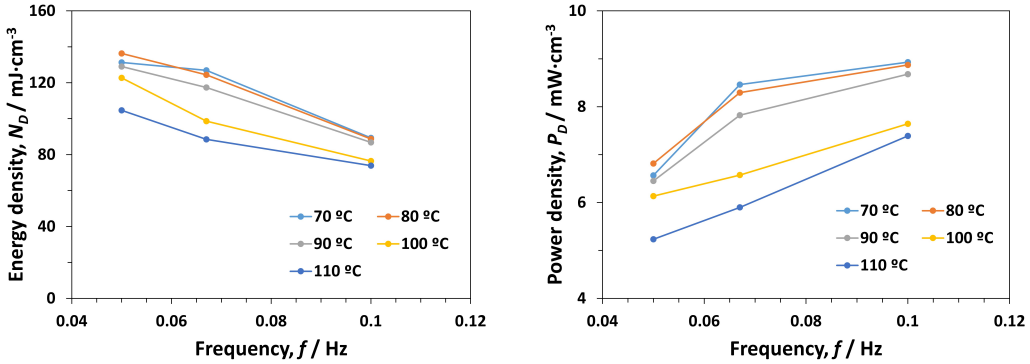

(a) Energy density (b) Power density

Figure 5.10: Power density and energy density of the BZT10 sample calculated using the cycle loop at different fluctuating frequencies.

limit would possibly lower the achievable power density of the sample (when the decrease fraction is more significant than the frequencies increase).

However, in the Kim cycle, the expansion in the electric field axis corresponds to the extension of the BCF area during the isodisplacement process resulting in an enhancement of energy density. Increasing the fluctuation frequency enhanced the time variability of the pyroelectricity, hence, increasing the electric field of the material faster and making it reach a further point in the cycle. This phenomenon is in good agreement with Eq. 5.2, which explains the increase in the proportion of the electric field with the time variation of the temperature.

The increase in the electric field during the isodisplacement process was proportional to the increase in frequency, which could compensate for the reduction in the heat conduction aspect. As a result, the power density of the BZT10 sample increased with frequencies and reach 8.9 mW/cm^3 at the temperature 70-90 ℃, frequency 0.1 Hz. Therefore, the Kim cycle is more suitable for application in highly fluctuating environments than the conventional Olsen cycle.

5.6 Power generation as a function of temperature span

The advantage of the Kim cycle over the Olsen cycle was once again expressed through the adjustment of the temperature span. At higher temperatures range the hysteresis curve of 2 respective T_L and T_H temperature shifted to new corresponding values, hence expanding the $D - E$ cycle loop. Moreover, according to Eq. 5.8, temperature variation by time $\frac{\Delta T}{\Delta t}$ was also improved, enhancing the electric field rise during the isodisplacement process. The power generation measure while optimizing the temperature spans is shown in Fig. 5.11 (Cycle loop) and Fig. 5.12 (Energy and power density).

As shown in Fig. 5.12, increasing the temperature range significantly increased the output power density of the sample. The energy density was improved, from 136.3, 124.4, 88.7 to 207.7, 180.0, 149.8 mJ/cm^3 corresponding to an enhancement in power density of 6.8, 8.3, 8.9 to 10.4, 12.0, 15.0 mW/cm^3 at frequencies of f = 0.05 Hz, 0.067 Hz, and 0.1 Hz, respectively. When

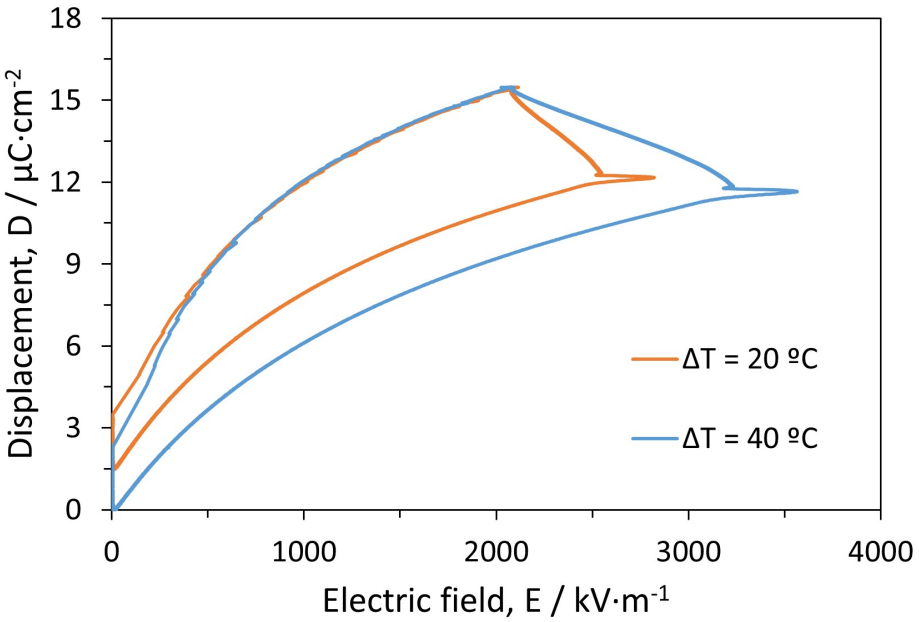

Figure 5.11: Cycle loop of the BZT10 samples at two different temperature spans: $\Delta T = 20$ and 40 ℃, $f = 0.01$ Hz

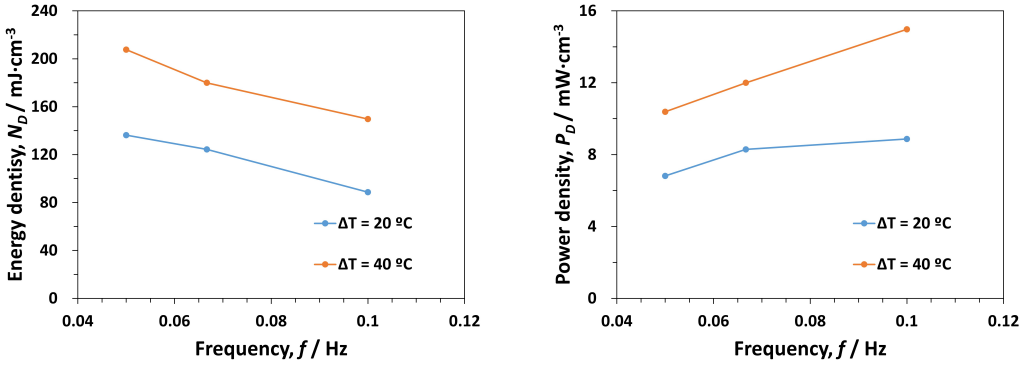

(a) Energy density (b) Power density

Figure 5.12: Power density and energy density of the BZT10 sample calculated using the cycle loop at different temperature spans.

increasing the temperature span, the CG line, which corresponds to the high-temperature discharge D-E loop, shifted to a lower position with respect to the new set temperature. This phenomenon expanded the loop area, enhancing the power density of the materials. Furthermore, the BC line, which expresses the electric field increase during the isodisplacement process, expanded to a higher value, indicating an enhancement in the energy density of the material. The temperature range ΔT in Eq. 5.8 also predicted an increase in energy density by improving the parameter. Compared with the conventional Olsen cycle, the new Kim cycle was more effective and sensitive to the temperature factor when considering the time variation heat-energy conversion process.

5.7 Designing the sample thicknesses

Heat conduction strongly affected the power generation behavior of the BZT10 system by limiting the achievable temperature hence induced a loop shrinkage. Therefore, improving the factor was considered an effective method to for sample designing against a selected waste heat condition. According to Eq. 5.8, the thermal resistivity can be manipulated with the sample thicknesses to achieve a better heat conduction, hence improving the pyroelectric conversion ability.

Fig. 5.13 shows the temperature adaptation of BZT10 samples when evaluated at temperature range $\Delta T = 20$ ℃, frequency $f = 0.05$ Hz and 0.1 Hz, and thicknesses of 0.5 mm and 0.8 mm. By decreasing the sample thickness the absolute thermal resistivity of the sample also reduced according to Eq. 5.8. This resulted in an improvement of heat conduction which synchronize with the fast raise of temperature in the 0.5-mm thick sample. However, as the temperature span stayed constant, the temperature tendency started to saturate toward the end of the heating process.

The high increasing rate of temperature was synchronized with the significant increase in the electric field and extension in the displacement axis, which is shown in the power loop of Figs. 5.9 and 5.14. Improvement in heat conduction enlarged the achievable average temperature difference in the 0.5-mm thick sample, hence shifting both the T_L and T_H hysteresis curves. Furthermore, the fast variation of temperature-induced improved pyroelectricity, which led to the significant rise of the electric field during the isolation.

However, as the temperature tendency started to decrease, the effect of temperature dependence on pyroelectricity weakened, and the increase in the electric field became negative, inducing a loss in the achieved power. In contrast, the stability of temperature change in the 0.8-mm thick sample resulted in a steady increase in the electric field during the isodisplacement step (Fig. 5.15) without any loop loss caused by pyroelectricity reduction.

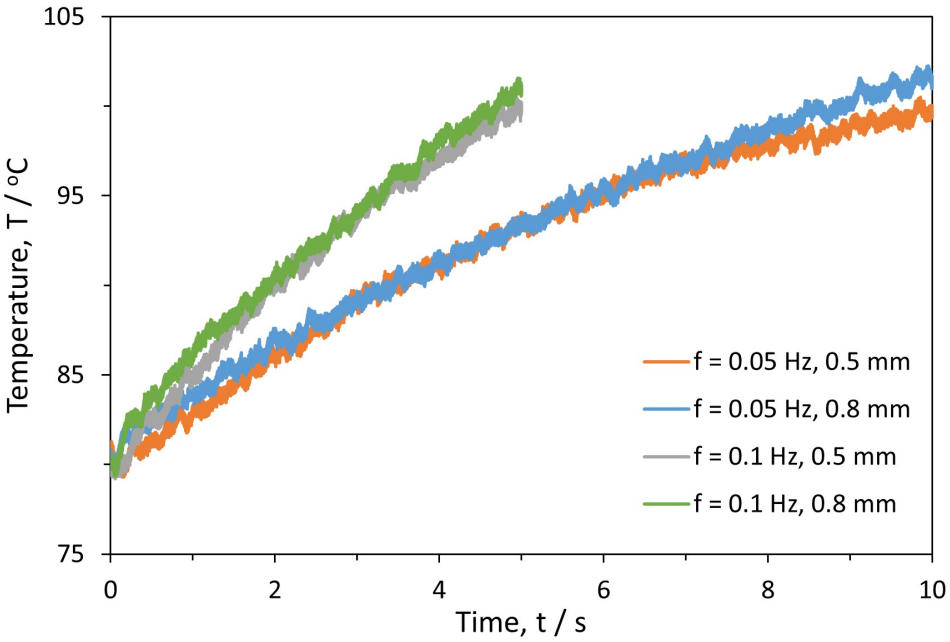

Figure 5.13: Temperature adaptation of the 0.5-mm and 0.8-mm thick BZT10 samples measured at $\Delta T = 20$ ℃, $f = 0.05$ Hz and 0.1 Hz.

Fig. 5.15 shows the calculated energy and power density of the BZT10 sample at two thicknesses $d = 0.5$ mm and 0.8 mm, the power density of the 0.5 mm-thick sample increased at a higher rate, 17.719 mW/cm^3 per Hz, 1.3 times larger than that of the 0.8-mm thick sample, whose increasing rate was 10.715 mW/cm^3 per Hz.

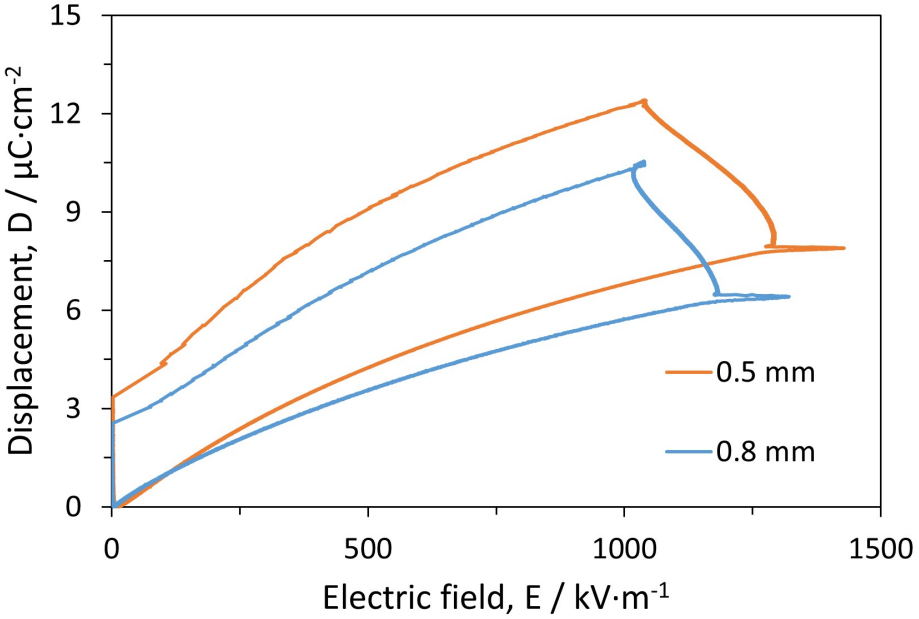

Figure 5.14: Cycle loop of the 0.5-mm and 0.8-mm thick BZT10 samples measured at $\Delta T = 20$ ℃, $f = 0.1$ Hz.

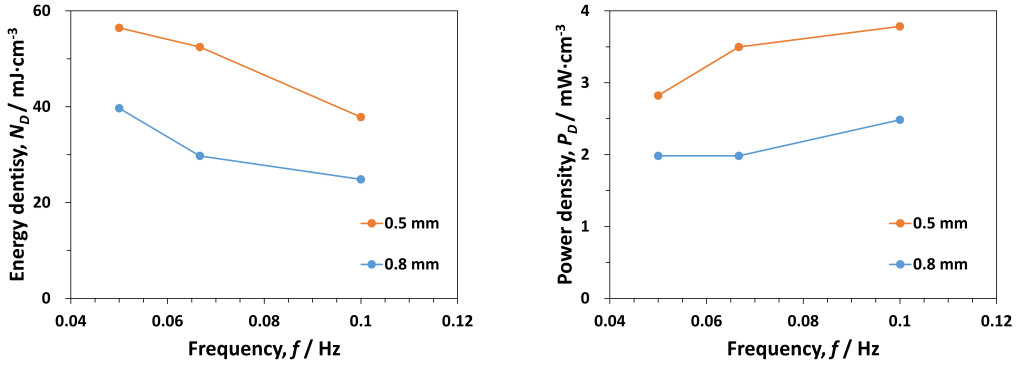

(a) Energy density

(b) Power density

Figure 5.15: Power density and energy density of 0.5-mm and 0.8-mm thick BZT10 samples measured at $\Delta T = 20$ ℃, $f = 0.05$ Hz, 0.067 Hz and 0.1 Hz.

5.8 Electric field application with DSW circuit

Besides the temperature factor of frequencies, differences, and thicknesses, electric field application was another mechanism helping improve the conversion by efficiently inducing the orientation of polarization. Fig. 5.16 shows the cycle loop area of the sample when applying different electric fields. The electric field application successfully increased the displacement value of the BZT10 sample, effectively orientating the domain structure. As a result, the observed D-E curve expanded, improving the achieved output power density. In contrast, increasing the applied electric field to 2000 kV/m slightly lowered the electric field's increase-tendency of the isodisplacement process. Although the effect was not significant, it suggested a saturation point in which the domains reached an orientation limit, thereby lowering the effectiveness of electric field application on the power density enhancement. Fig. 5.17 shows the linear fitting and the increasing tendency of the output power density by the external electric field application. At 0.05 Hz, the power density increased at an upward inclination of 0.002 mW/cm^3 per kV/m electric field applied, meaning the output density increased by an amount of 1 mW/cm^3 for every 500 kV/m. The tendency was improved up to 0.0046 mW/cm^3 per kV/m at the frequency $f = 0.1$ Hz.

5.9 Electrical factor

5.9.1 Polarizaiton and coercive field

Large hysteresis loop variation was responsible for efficient conversion. As a result, the highest power and energy density was achieved in the temperature range of 70-90 ℃ or 80-100 ℃ where the ferroelectric-relaxor phase transition appeared. The behavior was predicted using the variation in remanent and saturated polarization with a hysteresis loop. Nevertheless, there was still a minor difference between the prediction and measurement (temperature was slightly off the phase transition) due to the effect of thermal factor, which motivated us for an actual measurement with fluctuating source.

On the other hand, the design of materials with low coercive field allowed us a low loss during the E_L isoelectric process. As reported in many previous pieces of research, a high coercive field led to large loss and even loop cross [132, 133] which significantly reduced the converted energy. However, in

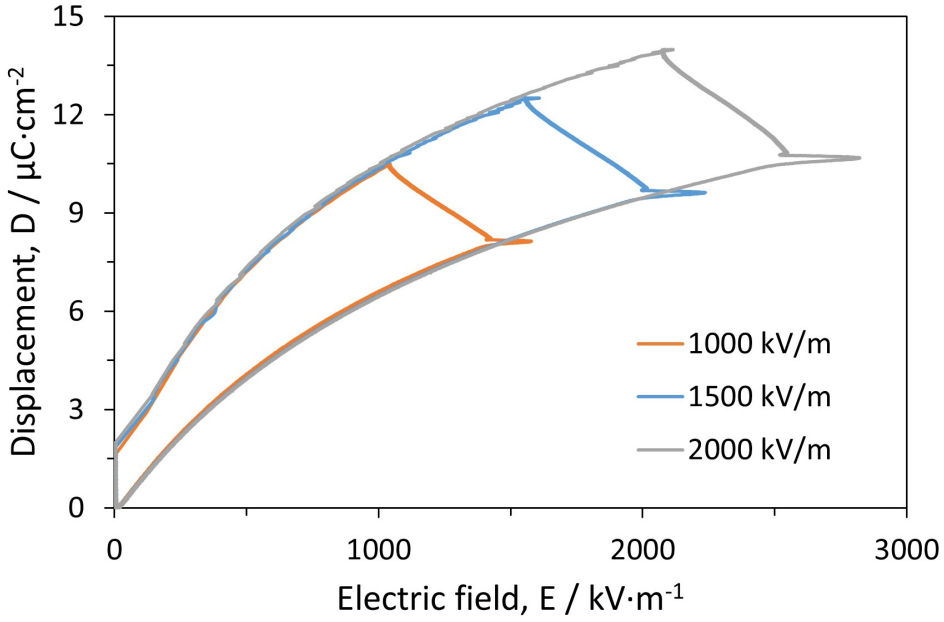

Figure 5.16: Cycle loop of the BZT10 samples as a function of the applied electric field.

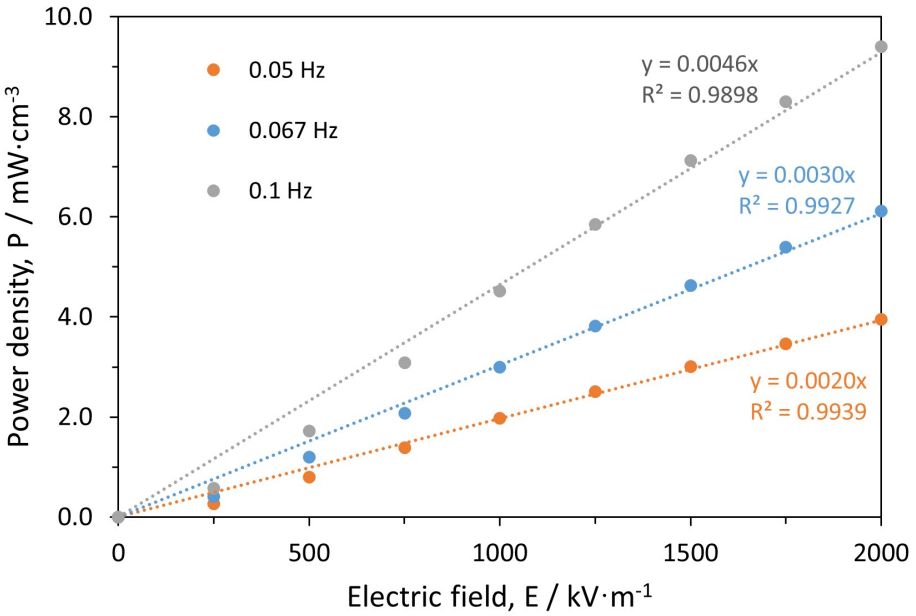

Figure 5.17: Linear fitting of the output power density of BZT10 samples as a function of the applied electric field

our case, a complete discharge to almost zero was obtained during the T_H isothermal step, providing a loss less conversion with BZT10.

5.9.2 Leakage current

Leakage current was the factor that accounted for the energy density loss observed in all the cycle loops. During the isodisplacement step, the displacement value D of the sample reached the maximum point and then started to decrease, regardless of the continuous increase in temperature. This reduction was different from the theory, where D must stay constant due to the isolating process. This was caused by the leakage current through the internal resistance of the sample and expressed by the Eq. 5.5. As a result, the received energy density was lower, and the maximum achievable electric field also got limited. Leakage current stay as an important factor that needs to be improved for further development of pyroelectric heat to electricity.

5.10 Thermal factor

5.10.1 Heat conduction

The thermal factor that affects pyroelectric conversion the most was heat conduction. According to the temperature factor results, vast temperature differences and rapid fluctuations are ideal for achieving a high power density in pyroelectric materials. However, this conflicts with the natural characteristics of the materials, particularly the heat conduction properties. Heat transfer obstructs the temperature adaptation of the sample toward such an ideal condition, which is a good example of loop area reduction when increasing the fluctuating frequencies. As a result, calculation using two isothermal hysteresis loops induce large errors compared to the actual experiment. Therefore, understanding the effect of heat conductivity on different system designs is necessary.

In previous sections, the effect of heat conduction was discussed as a primary factor in the degradation of the loop cycle when increasing the frequencies and reducing thickness. As the frequencies increased, less heat was conducted on the low-temperature side due to the reduction of transferring time, as a result, the internal temperature was lower compared to the low-frequencies cases.

On the other hand, the thickness reduction enhanced the temperature adaptability of materials. As the thickness d decreases, the heat took less time to conduct to the T_L side, hence, the thin sample reaches the high temperature faster than the thick ones. However, as the thin sample reached the desired temperature fast, the fluctuation-induced pyroelectricity got weaken causing a loss in the observed cycle loop.

5.10.2 Heat expansion

As the heat was injected into the samples, expansion followed by the secondary pyroelectric effect would appear, lowering the primary effect. Although all processes result in a positive electric field rise, meaning the BZT10 sample resulted in an overall minus pyroelectric effect, the small loss observed in the cycle loop of the 0.5-mm thick sample might correspond to the heat expansion secondary pyroelectric effect. At the temperature adapted near the desired temperature, the primary effect got weakened and the secondary ones took over, leading to the minus electric field rise. However, in this case, the effect was minor compared with the great extension of the BGF area which can be bypassed.

5.11 Output power density of BZT10 sample in single heat source configuration

Fig. A.2 in the appendix shows the output power density and Fig.5.18 summarizes the maximum value of BZT10 samples at three different frequencies f = 0.05, 0.067, 0.1 Hz; temperature spans ΔT = 20, 40 ℃; thicknesses d = 0.4, 0.5, 0.6, 0.7, 0.8 mm.

An increasing tendency was observed at the low-temperature range when reducing the sample thickness from 0.8 mm to 0.7 mm and 0.6 mm. The power density was enhanced owing to the improvement in heat conductivity, distributing the heat fluctuation uniformly toward the sample overall. The loop areas of the 0.7-mm and 0.6-mm thick samples were larger than that of the 0.8 mm-thick sample. Another factor that contributed to the enhancement was the improvement of the spontaneous polarization and coercive field as the sample thickness decreased. This phenomenon was previously reported by You et al. in a study on ferroelectric film $BiFeO_3$.[166]

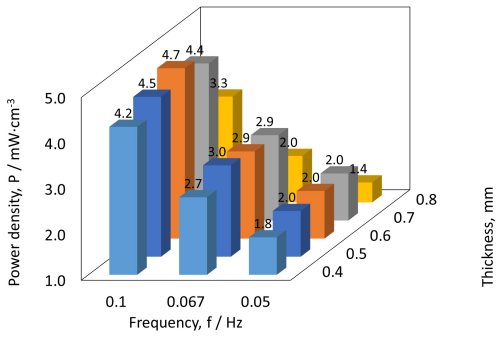

(a) $\Delta T = 20$ ℃, $E = 1000$ kV/m

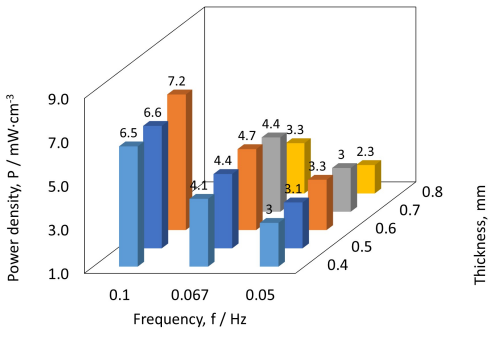

(b) $\Delta T = 40$ ℃, $E = 1000$ kV/m

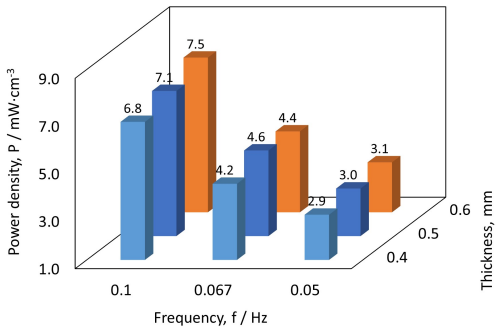

(c) $\Delta T = 20$ ℃, $E = 1500$ kV/m

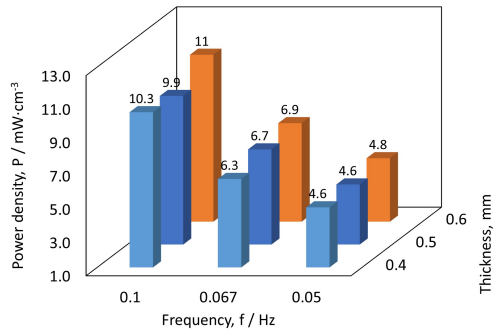

(d) $\Delta T = 40$ ℃, $E = 1500$ kV/m

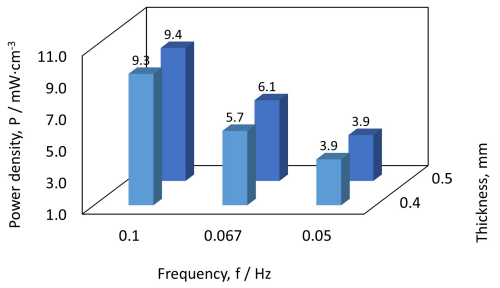

(e) $\Delta T = 20$ ℃, $E = 2000$ kV/m

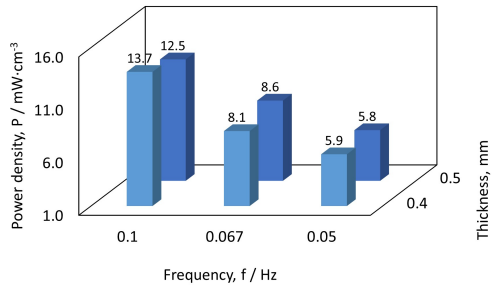

(f) $\Delta T = 40$ ℃, $E = 2000$ kV/m

Figure 5.18: maximum power density of BZT10 samples with different thicknesses and frequencies

However, as sample thicknesses reduced to 0.5 mm and 0.4 mm, a drop in the electric field occurred due to the poor temperature adaptation at high temperatures. Therefore, a loop area loss similar to that of the 0.5-mm thick sample was induced, which reduced the power generation ability.

Furthermore, by enhancing the heat fluctuation properties to a high rate and a considerable difference (ΔT = 40 ℃, f = 0.1 Hz), and applying a high electric field (2000 kV/m), the poor temperature adaptation was successfully overcome. The spontaneous polarization of the 0.4-mm thick sample was improved, and the power density reached a maximum of 13.7 mW/cm^3.

Table 5.1 shows the comparison of BZT10 under a single fluctuating heat source configuration with other conventional lead-based materials. The BZT10 sample exhibited a lower energy density of 137 mJ/cm^3 due to the natural behavior of single source configuration but the highest energy density per applied electric field and temperature difference of 0.171 μJ/(cm^2·K·V) among bulk materials in BT family. The value suggests a high potential of the BZT10 sample to be applied in low-grade waste heat recovery using single heat source, or investigated for its future energy harvesting ability with the novel Kim cycle.

Table 5.1: The comparison in energy density, power density, and energy density per applied electric field and temperature difference of the BZT10 sample with other lead-free bulk materials.

Materials	N_D	E_L	E_H	T_L	T_H	$\frac{N_D}{\Delta T \cdot \Delta E}$	P_O	Ref.
$Ba(Zr_{0.05}Ti_{0.95})O_3$	4.25	3.25	7.42	30	125	11	Calculated from D-E hysteresis loop	[139]
$Ba_{0.85}Ca_{0.15}Ti_{0.9}Ti_{0.1}O_3$ - 5% Fe	305	3	90	30	110	44		[142]
$0.2BaZr_{0.2}Ti_{0.8}O_3$ - $0.8Ba_{0.7}Ca_{0.3}TiO_3$	371	0	30	10	150	88		[140]
$0.5BaZr_{0.2}Ti_{0.8}O_3$ - $0.5Ba_{0.7}Ca_{0.3}TiO_3$	108	0	20	30	90	90		[141]
$0.5BaZr_{0.2}Ti_{0.8}O_3$ - $0.5Ba_{0.7}Ca_{0.3}TiO_3$	447	0	30	10	150	106		[140]
$Ba_{0.72}Sr_{0.28}TiO_3$	486	0	70	25	85	116		[144]
$Ba_{0.85}Sr_{0.15}Zr_{0.1}Ti_{0.9}O_3$	300	0	30	30	90	167		[141]
$Ba_{0.85}Ca_{0.15}Ti_{0.88}Sn_{0.02}Zr_{0.1}O_3$	332	1	29	30	100	169		[143]
$BaZr_{0.1}Ti_{0.9}O_3$	137	0	20	70	110	171	13.7	This

N_D: Energy density, mJ/cm^3
E_L: Low electric field, kV/cm
E_H: High electric field, kV/cm
T_L: Low temperature, ℃
T_H: High temperature, ℃
$\frac{N_D}{\Delta T \cdot \Delta E}$: Energy density per applied electric field and temperature difference, $\mu J/(cm^2 \cdot K \cdot V)$
P_O: Power density, mW/cm^3, $P_o = N_D \times f$

Chapter 6

Pyroelectric heat to electricity of lead-free BZT10 in a simulated cooling-assisted fluctuating heat source

6.1 Cold-sink assisted configuration for pyroelectric energy harvesting

6.1.1 Objectives

In chapter 5, the pyroelectric conversion behavior under a single heat source configuration of the lead-free BZT10 was investigated, showing novelty in the simple setup and feasibility with many application scenes from natural waste heat. In this chapter, we focused on the conversion ability to combine waste heat with a cooling system to generate large electricity. Although, the cold-sink assisted configuration required multiple sets up and additional energy consumption, some of the application scenes, which have a built-in cooling system (supercomputer9 or simply exposure to the cold surrounding environment (during winter), can be utilized to achieve the best potential of waste heat recovery with pyroelectric. The situation motivated us to investigate each aspect of the system design for cold-sink, heat input, and output to achieve the best practical potential using a fluctuating source.

6.1.2 Novelty

Compared to the single heat source configuration, materials working under a cooling-assisted setup experience higher temperature differences, hence the corresponding pyroelectricity will be more sensitive, affecting conversion behavior. Therefore, an practical measurement using a proper fluctuating heat source is necessary to understand the behavior of each isothermal, isoelectric, and isodisplacement process. The discovery will enable the materials design with the selected waste heat and cold-sink setup to achieve the targeted high potential.

Furthermore, in the cooling-assisted mode, heating and cooling rate are adjustable parameters. This gives flexibility over the single heat source configuration where waste heat was an uncontrollable aspect. Therefore, understanding the influence of heating and cooling rate on the conversion behavior allows an efficient conversion without any additional investment in the cold-sink design which is costly.

Overall, chapter 6 exhibited its novelty to be the first research using an actual fluctuating heat source to investigate the practical waste heat recovery of lead-free BZT10 under a cooling-assisted configuration and adapt the distinguished heating/cooling rate control to achieve an optimized design with pyroelectric conversion.

6.2 Experimental

Similar to chapter 5, the power generation ability of BZT10 in a cooling-assisted configuration was evaluated using the DSW circuit and Kim cycle. The cycle loop was first investigated using different heating and cooling rates. Afterward, the effect of low-temperature and high-temperature induced by the heat source and cooling devices respectively was evaluated, and the maximum achievable potential of the BZT10 samples was revealed.

6.3 Heat to electricity in a simulated cooling-assisted temperature source

6.3.1 Effect of heating rate

Figs. 6.1 and 6.2 show the $D - E$cycle loop evolution and harvested energy density of the BZT10 sample at different heating rates. From fig. 6.1, as the heating rate increased, the maximum value of the electric field rise was enhanced corresponding to the increase in the temperature variation by time parameter $\Delta T/\Delta t$. Substituting the condition to Eq. 5.2, the increase of the electric field can be predicted.

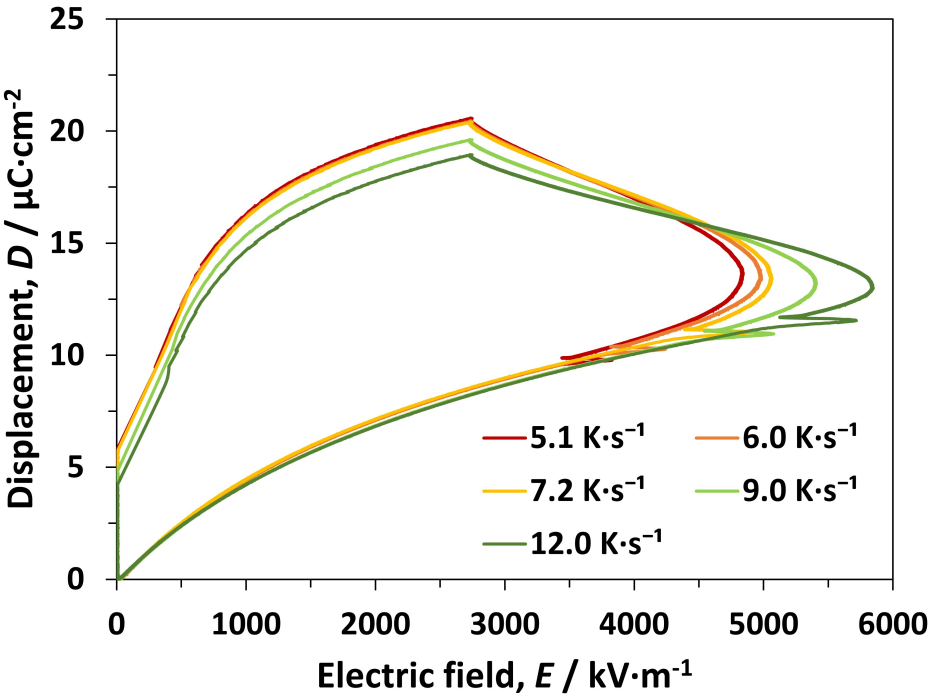

Figure 6.1: Cycle loop of the BZT10 samples as a function of heating rate. The test was conducted at E_L = 0 kV/m, E_H = 2632 kV/m, T_L = 30 ℃, T_H = 120 ℃, and a cooling rate of 7.2 K/s.

However, the fast heating also reduced the stability of the temperature's equilibrium state in the BZT10 system. The heating time decreased affected

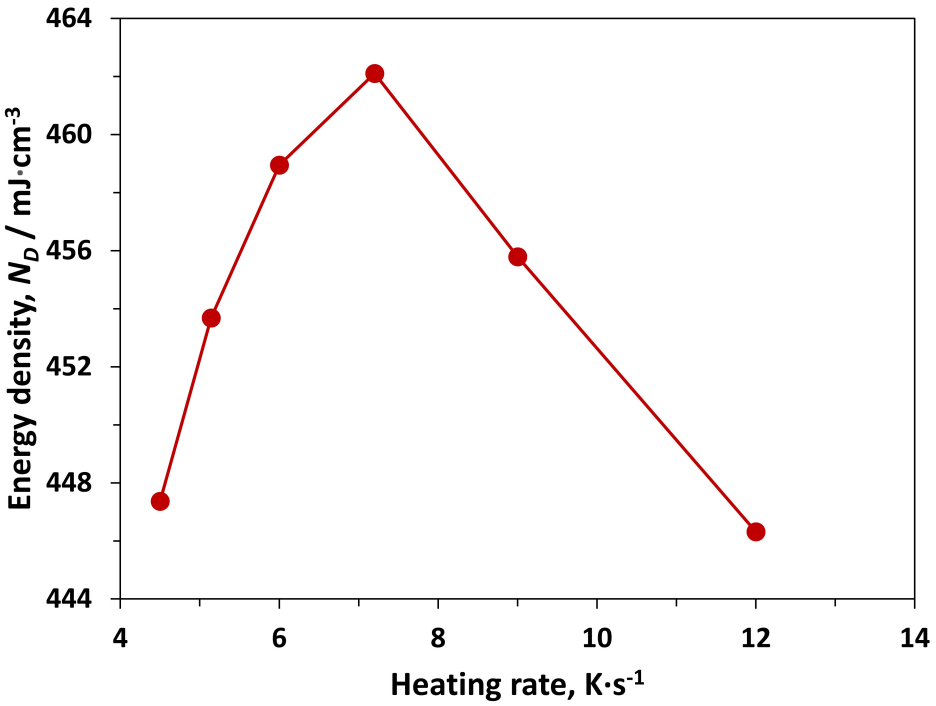

Figure 6.2: Energy density of the BZT10 samples as a function of heating rate.

the heat flux transferred by heat conduction to the internal section (Eq. 5.8). The average temperature was lesser and the cycle loop exhibited a quasi-equilibrium with the height continuously dropping down. The same phenomenon has been observed for the Olsen cycle in many previous reports [158, 159, 164].

In Fig. 6.2, as the heating rate increased from 4.5 to 7.2 K/s (heating time reduced from 20 to 12.5 s), the extra energy density dominated the reduction, resulting in an enhancement of the energy density of BZT10 from 447 to 462 mJ/cm^3. However, a further rise in the heating rate decreased the energy density due to quasi-equilibrium states.

In Fig. 6.2, at low heating rate of 4.5 to 7.2 K/s (heating time reduced from 20 to 12.5 s), the pyroelectricity improvement dominated the reduction by bad heat conduction, and the energy density of BZT10 continuously rise from 447 to 462 mJ/cm^3. However, upon 7.2 K/s, the unstable quasi-equilibrium of temperature was more effective, hence reduced the energy density.

6.3.2 Effect of cooling rate

Similar behavior was also observed when manipulating the cooling rate. Fig. 6.3 shows the evolution of the loop area and Fig. 6.4 shows the reduction of energy density as the cooling rate increased. As the cooling rate increased from 4.5 to 7.2 K/s (cooling time reduced from 20 to 12.5 s), the effect of heat conduction kicked in similar to the cases of heating rates, the system's temperature shifted to a quasi-equilibrium state of less average temperature, which thinned the loop area and the obtained energy density. The pyroelectric effect was also induced due to the improvement of temperature variation over time, but with a minor impact. Therefore, the isoelectric step of the Olsen cycle is not effective against fluctuating behavior, hence gradually causing a drop in energy density with the increase of cooling rate. The maximum achieved energy density was 475 mJ/cm^3 at 20 s and 22.5 s cooling time.

6.3.3 Waste heat temperature T_H

Therefore, a heating time of 12.5 s and a cooling time of 22.5 s were considered the optimized conditions to maximize the potential of BZT10 samples. Applying these conditions, we evaluated the energy density at different low

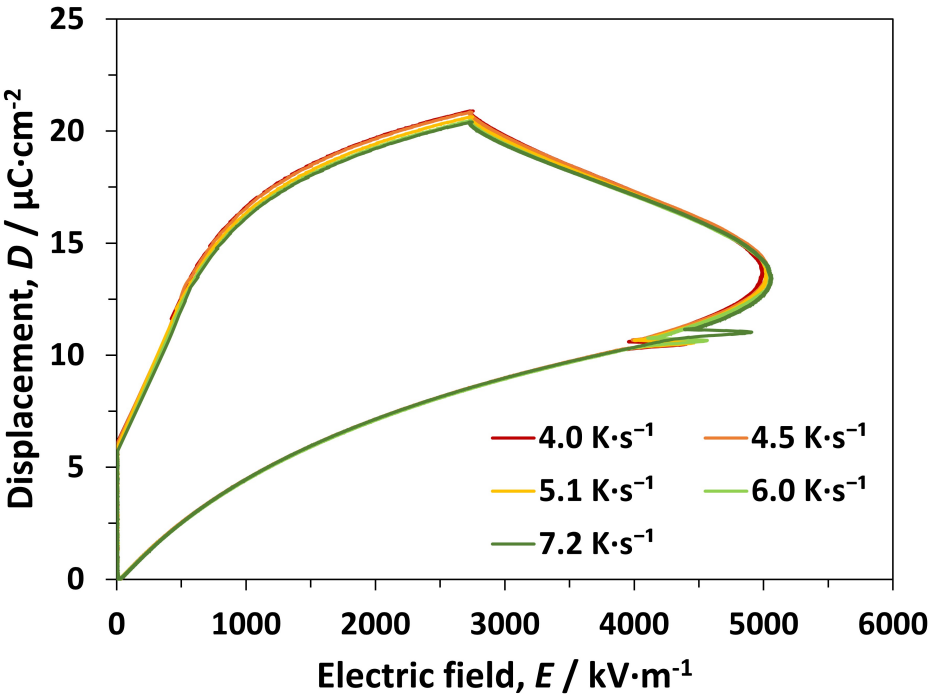

Figure 6.3: Cycle loop of the BZT10 samples as a function of cooling rate. The test was conducted at E_L = 0 kV/m, E_H = 2632 kV/m, T_L = 30 ℃, T_H = 120 ℃, and a heating rate of 7.2 K/s.

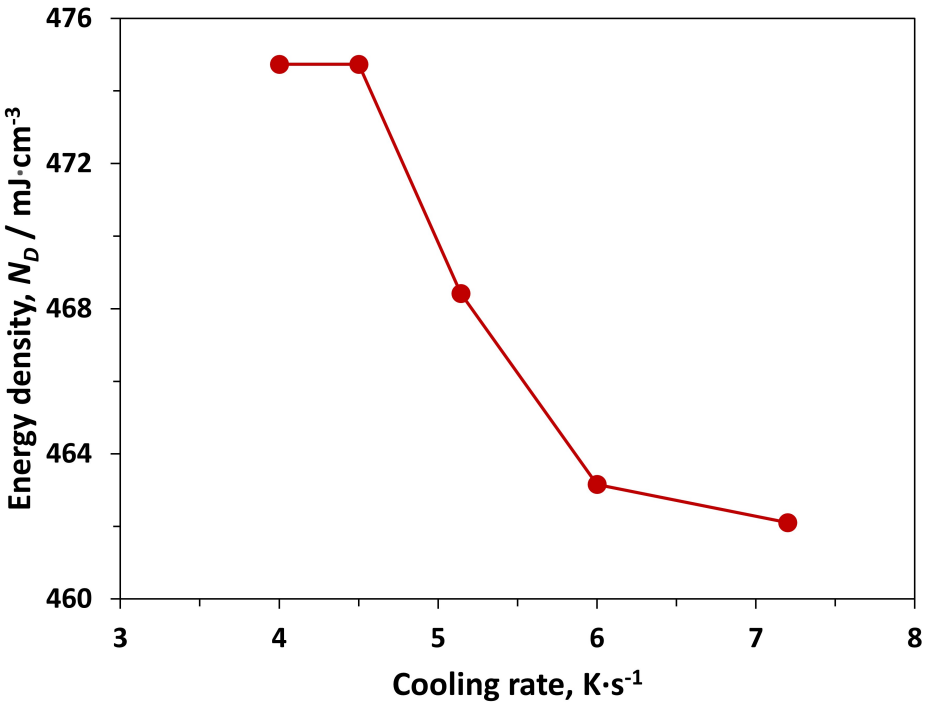

Figure 6.4: Energy density of the BZT10 samples as a function of cooling rate.

temperatures T_L and high temperatures T_H using the Kim cycle. Fig. 6.5 shows the cycle loop and fig. 6.6 shows the energy density for the BZT10 sample at different T_H values of 90, 100, 110, 120, and 130 ℃. As T_H increased, the energy density increased from 383 mJ/cm^3 at 90 ℃ to 495 mJ/cm^3 at 130 ℃. The rise in T_H enhanced the temperature difference ΔT in Eq. 5.2 and increased the loop area in the electric field axis direction during the isodisplacement process. Increasing T_H also shifted the T_H hysteresis curve to a new position, expanding the $D-E$ cycle loop in the displacement axis direction. BZT10 samples exhibit a decent improving rate with the increase of high-temperature T_H but started to saturate at 110 ℃ due to the phase transition to paraelectric with a lower polarization variation. Therefore, the BZT10 materials exhibited their best potential during the relaxor-paraelectric phase transition at 110-120 ℃ under a cooling-assisted configuration rather than the ferroelectric-relaxor phase at 70-80 ℃ with single heat source setup.

$$\frac{\partial D}{\partial t} = \epsilon \frac{\partial E}{\partial t} + \frac{\partial P}{\partial t} = \pi \frac{\partial T}{\partial t} \tag{6.1}$$

where D is dielectric displacement, E is electric field, P is the polarization induced by pyroelectric effect $\pi \frac{\partial T}{\partial t}$ and t is time.

6.3.4 Adjusting cooling temperature T_L

Finally, the energy density behavior of the BZT10 sample with the Kim cycle reached the maximum of 504 mJ/cm^3 as low temperature T_L reached 20 ℃. Fig. 6.7 shows the loop area and Fig. 6.8 shows the energy density as a function of T_L. Similarly, the relocation of T_L hysteresis loop and pyroelectricity due to the increase of temperature variation over time was the two main factors for the expansion of the $D-E$ cycle loop and the continuous increase of energy density.

6.4 Potential of BZT10 under cooling-assisted configuration

The BZT10 samples under cooling-assisted configuration exhibited the maximum energy density of 504 mJ/cm^3 using simulated waste heat at 120 ℃ with

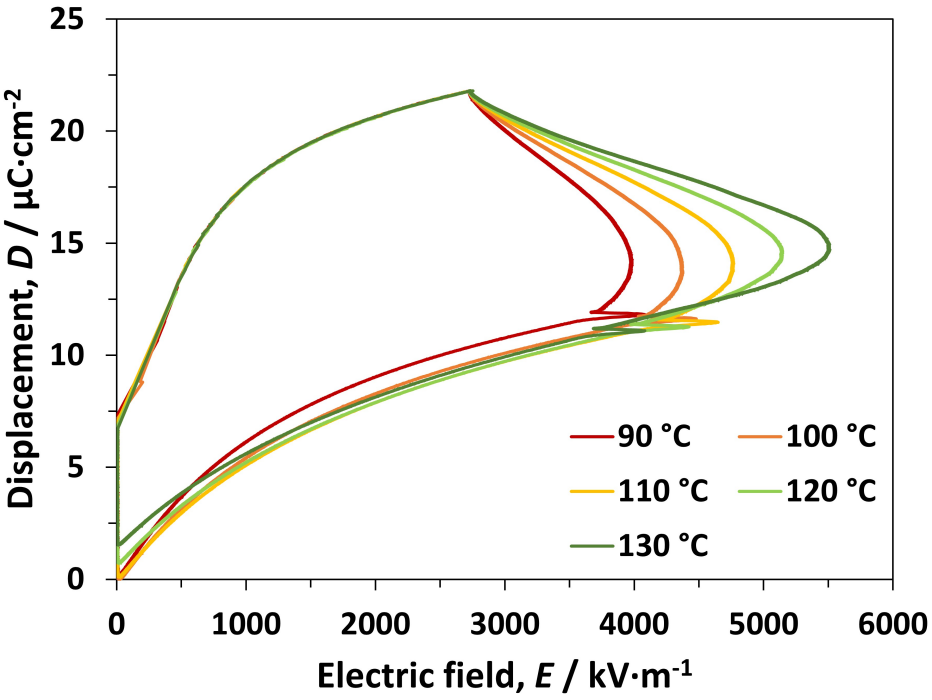

Figure 6.5: Cycle loop of the BZT10 samples at different high-temperatures T_H. The test was conducted at $E_L = 0$ kV/m, $E_H = 2632$ kV/m, heating time 12.5 s, cooling time 22.5s, and $T_L = 25$ ℃.

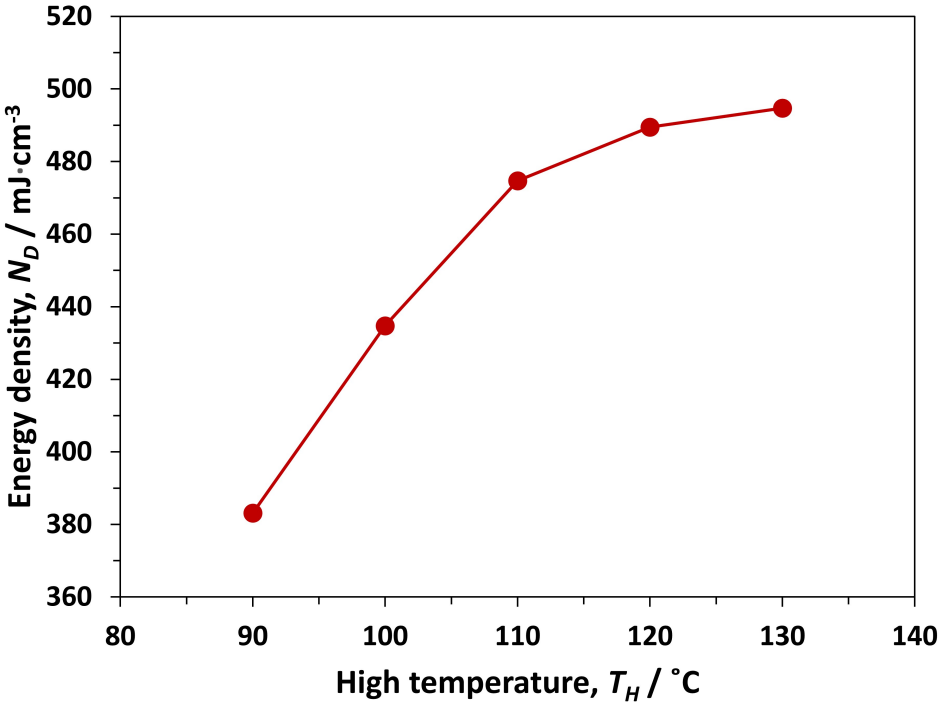

Figure 6.6: Energy density of the BZT10 samples at different high-temperatures T_H.

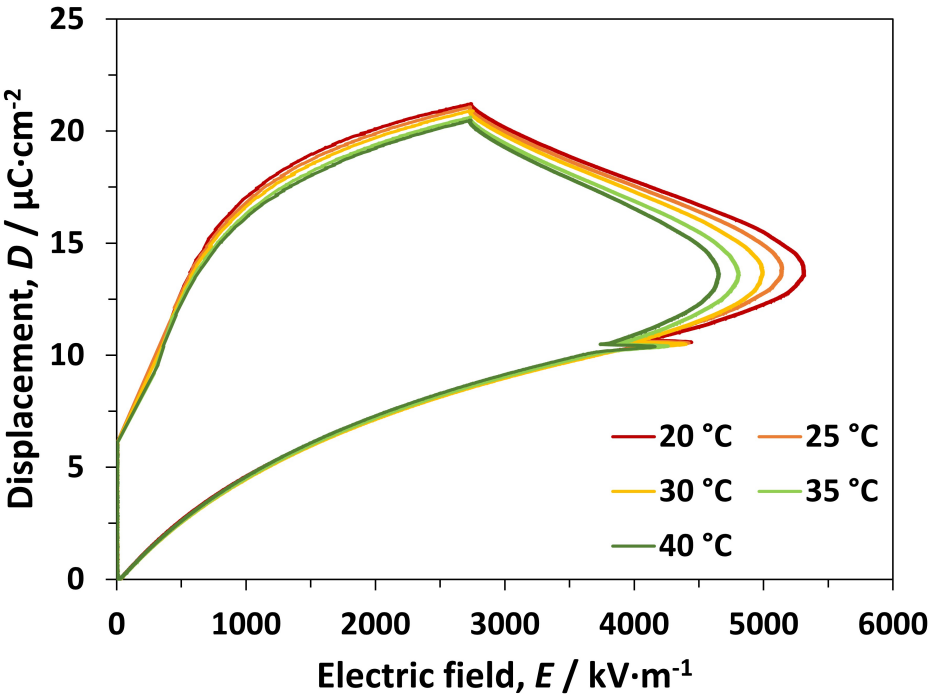

Figure 6.7: Cycle loop of the BZT10 samples at different low-temperatures T_L. The test was conducted at $E_L = 0$ kV/m, $E_H = 2632$ kV/m, heating time 12.5 s, cooling time 22.5s, and $T_H = 120$ ℃.

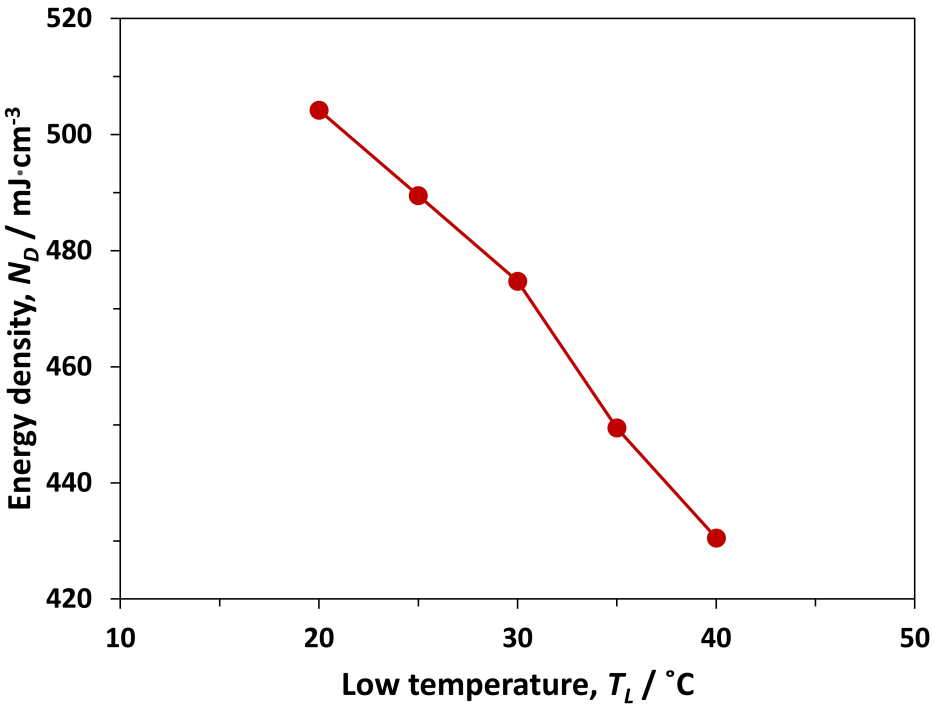

Figure 6.8: Energy density of the BZT10 samples at different low-temperatures T_L.

cooling support for a low temperature of 20 ℃, heating time of 12.5 s and cooling time of 22.5 s. This value is so far higher than any theoretical result reported in the soft-type lead-free bulk ferroelectric materials. Furthermore, the energy density divided by the applied electric field and temperature difference of the sample was 0.192 μJ/(cm^2·K·V), roughly two times higher than the well-known BZT/BCT composition. The value suggested that under the similar condition of applied electric field and temperature difference, BZT10 would have a better performance than any other materials in the same BT family. Therefore, BZT10 composition is a potential and novel discovery for soft-type lead-free bulk ferroelectric materials used in energy harvesting applications.

Chapter 7

Isovalent doping of Ca and Sr for enhancing pyroelectric heat to electricity of lead-free BZT10

7.1 Limitation of the Ba(Zr Ti)O_3 composition

Pyroelectric conversion using ferroelectric materials exhibits its best potential during the phase transition. As shown in the Ba(Zr Ti)O_3 composition, the power generation under a single waste heat source configuration reaches the highest value upon transition to the relaxor phase at around 70 ℃. Similarly, at the Curie temperature of 110 ℃, the energy density under cooling-assisted setup showed a saturated tendency.

To achieve the best practical conversion efficiency, we want to utilize the waste heat conversion at the phase transition. Therefore, in this chapter, we modified the Ba(Zr Ti)O_3 composition, shifting the Curie temperature to lower than 110 ℃ to efficiently recovering waste heat at lower temperature band.

7.2 Isovalent dopants

Strontium (Sr) and Calcium (Ca) are two elements in the same group 2 - alkaline earth metal as the A-site Ba. Ba belongs to period 6, while Sr and Ca are in periods 5 and 4, respectively. Therefore, Sr and Ca have smaller

ionic radii than Ba. Table. 7.1 shows the ionic radii of the three-element Ca, Sr, and Ba.

Table 7.1: Ionic radii of Ba, Sr, and Ca

Element	Ionic radii
Ba	1.61
Sr	1.44
Ca	1.34

According to the Goldschmidt Tolerance Factor discussed in chapter 3, doping of Ca, or Sr would reduce the r_A, hence, decreasing the tolerance factor t. The phenomenon kick in the side effects, shrinking the unit cell and the [BO6] octahedron. As a result, the available space for Ti^{4+} distortion followed by ferroelectricity is reduced. Therefore, isovalent doping of Ca and Sr into the A-site Ba was reported to efficiently reduce the Curie temperature and dielectric constant for low input energy.

Furthermore, doping of Ca and Sr into the structure enhances the PNRs structure of the relaxor phase. The bond length difference which is original for the relaxor phase formation is improved due to the variation in A-O bond length with dopants, resulting in the improvement of our important relaxor characteristic, enhancing the pyroelectric conversion with low-grade waste heat.

7.3 Purpose and novelty

7.3.1 Purpose

In this chapter, we investigate the effect of the isovalent Strontium (Sr) and Calcium (Ca) doping in the BZT10 system, to reduce the Curie temperature for low-grade waste heat recovery, enhancing the mix-relaxor behavior for a more efficient pyroelectric conversion.

7.3.2 Novelty

Although there were reports about the effect of isovalent dopants like Ca and Sr on the ferroelectric properties as well as pyroelectric conversion calculation using hysteresis loops, the actual measurement considering all the thermal and electrical aspects was undiscovered. Besides the improvement of the primary factor like dielectric constant, polarization, leakage current induced by internal resistance, loop loss by secondary pyroelectric effect, or even the inefficient heat conduction would strongly affect the behavior hence limiting the ideal approach. Therefore, this chapter shows the novelty of clarifying all of the suggested factors and investigating the total effect on the actual recovery which give the true idea of which dopants and strategies are suitable for improving the pyroelectric conversion in the future.

7.4 Experimental

7.4.1 Synthesis

The Sr and Ca doped BZT10 sample was fabricated using the same route explained in section 1 of chapter 4. The reactive oxide used for the synthesis was $SrCO_3$ (Wako, 99.0%) and $CaCO_3$ (Kojundo Chemical Lab., 99.99%).

A molar ratio of 2.5 mol% and 5 mol% was fabricated with each dopant of Ca and Sr.

7.4.2 Evaluation

The dielectric constant of each sample was measured using the impedance analyzer, the hysteresis loop with the ST circuit, and power generation using the DSW circuit.

7.5 Microstructure of Sr and Ca-doped BZT10

Fig. 7.1 shows the XRD patterns of Sr, Ca, and un-doped sample after each fabrication processes.

Similar to the un-doped sample, Ca and Sr-doped samples showed a secondary peak of $BaZrO_3$ after the calcination process. However, the peak disappeared

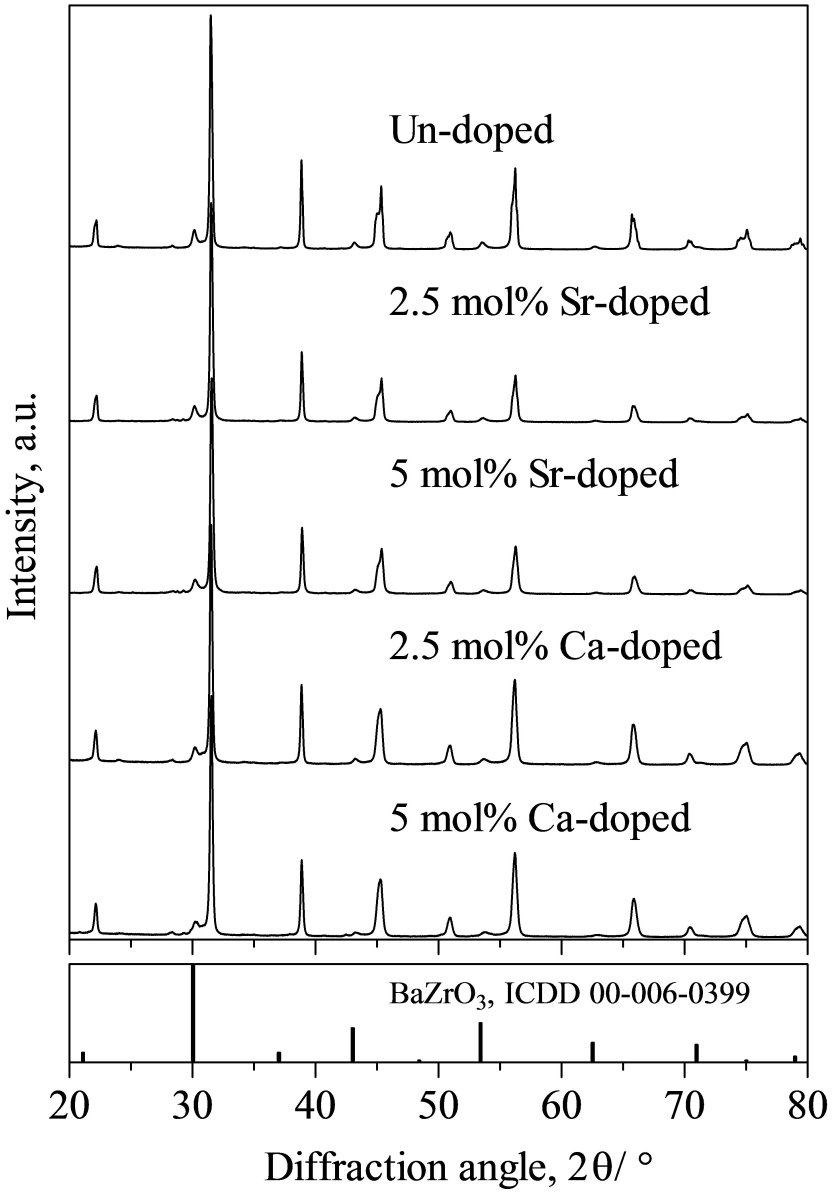

(a) As-calcinated, 1000 ℃, 8h

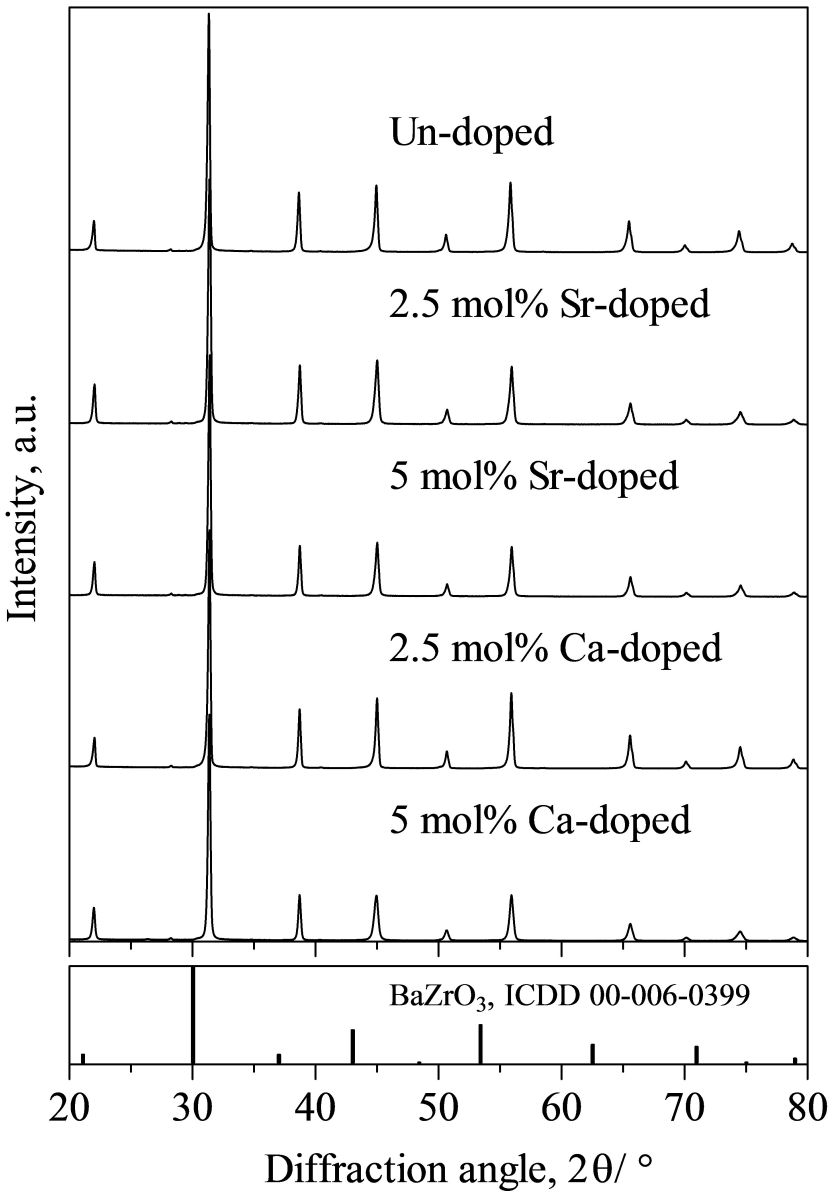

(b) As-sintering, 1400 ℃, 6h

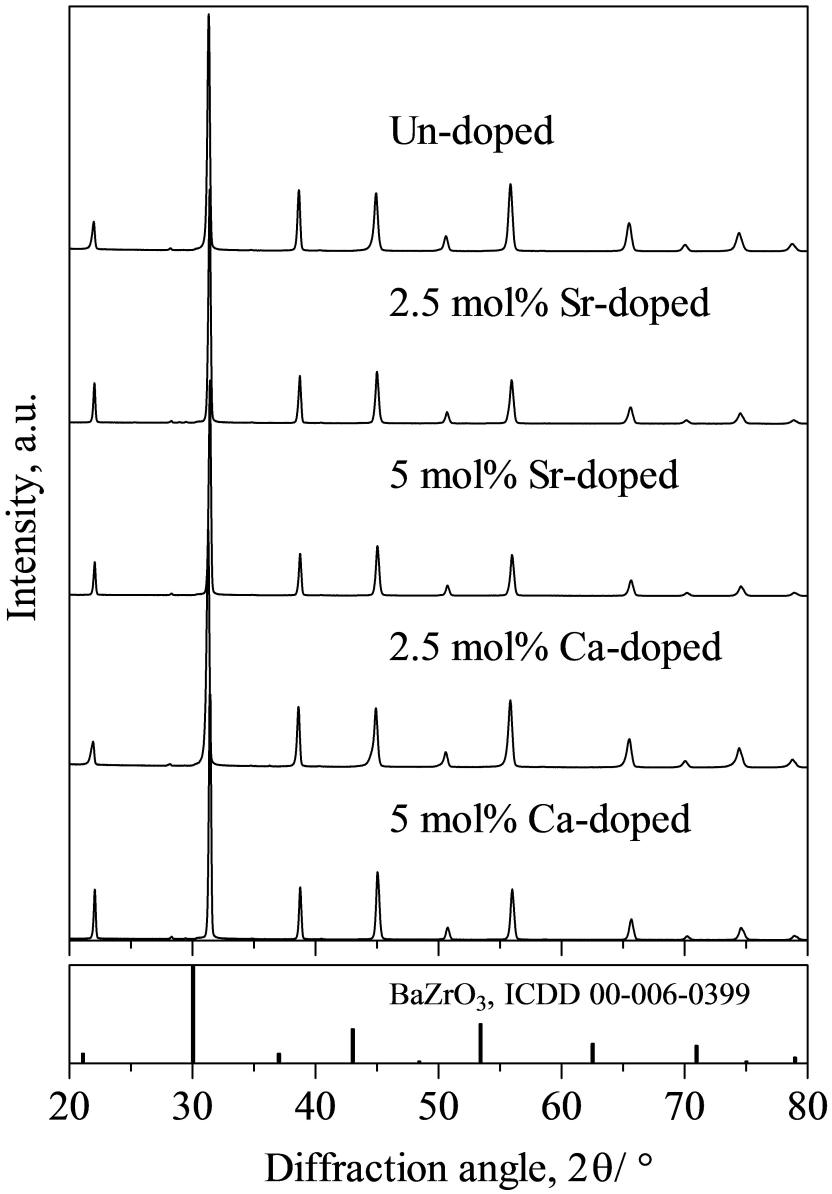

(c) As-annealed, 1250 ℃, 8h

Figure 7.1: XRD patterns of Sr, Ca, and un-doped BZT10 samples

after the sintering and annealing. All sample was crystallized to the perovskite. Fig. 7.2 shows the peaks shifting to high diffraction angle of doped samples. Doping with small ionic radii elements shrink the unit cell, hence lead to peak shifting as observed. Similar to the un-doped sample, Sr and Ca-doped BZT10 show left-right asymmetric main peaks of tetragonal and rhombohedral phases.

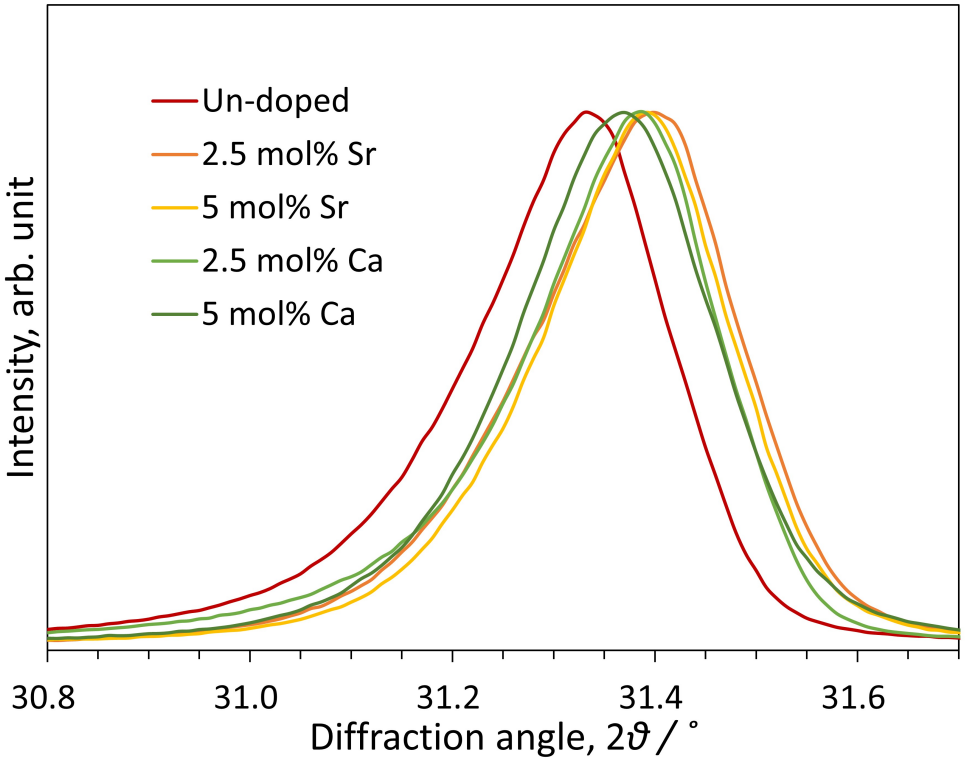

Figure 7.2: Main peaks shifting in doped BZT10 samples

Figs. 7.3 to 7.7 shows the fracture image observation of un-doped and 4 doped samples. The BZT10 sample was synthesized as a high-density bulk material, however, it exhibited a minor amount of closed pore when doped with Sr and Ca.

Figs. 7.8 shows the EDS patterns of each sample. From the result, the dopants dissolute into the sample and form a single phase with other components.

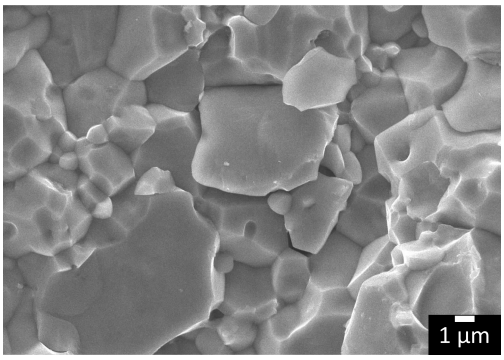

(a) As-sintered

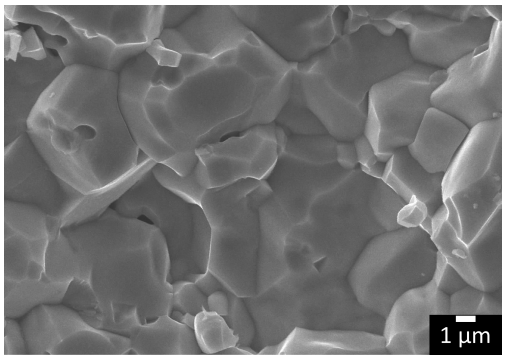

(b) As-annealed

Figure 7.3: Fracture image of un-doped BZT10 samples

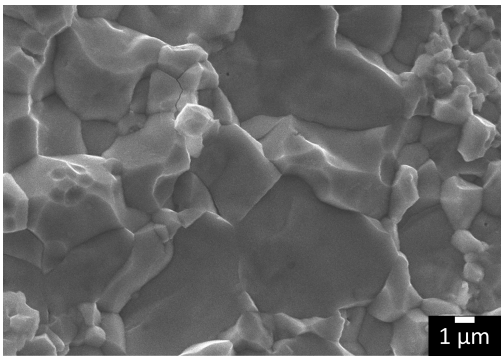

(a) As-sintered

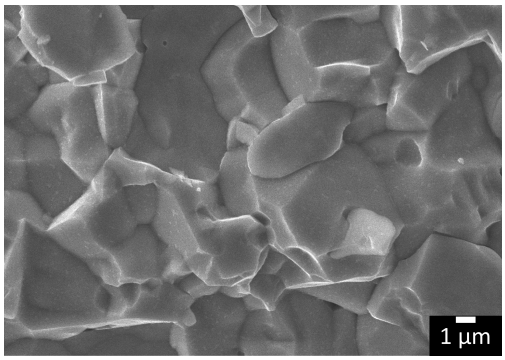

(b) As-annealed

Figure 7.4: Fracture image of 2.5 mol% Sr-doped BZT10 samples

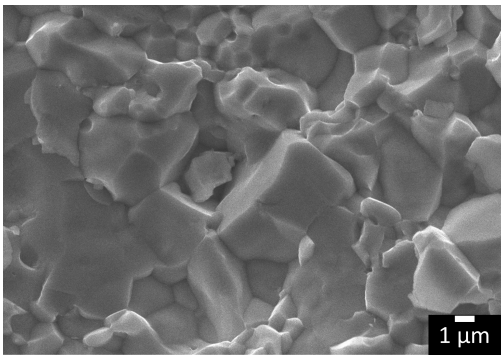

(a) As-sintered

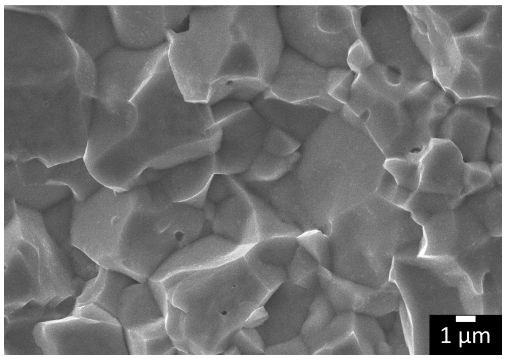

(b) As-annealed

Figure 7.5: Fracture image of 5 mol% Sr-doped BZT10 samples

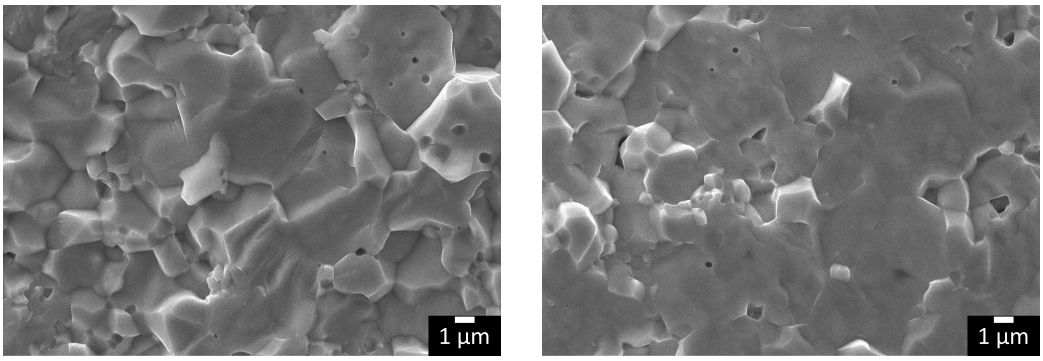

(a) As-sintered (b) As-annealed

Figure 7.6: Fracture image of 2.5 mol% Ca-doped BZT10 samples

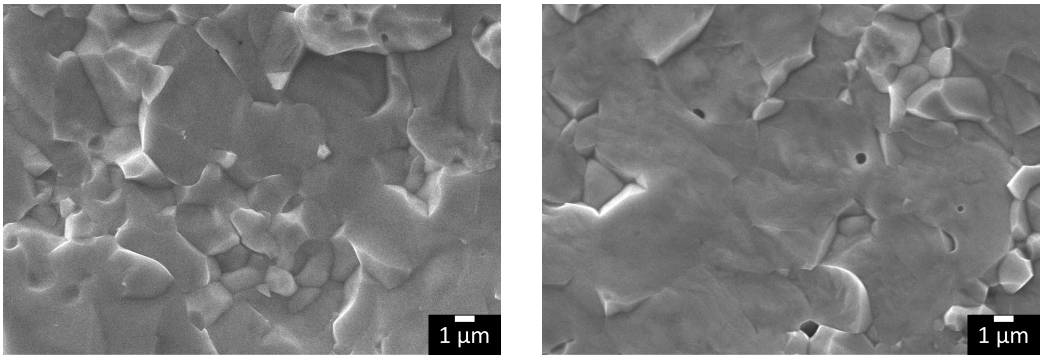

(a) As-sintered (b) As-annealed

Figure 7.7: Fracture image of 5 mol% Ca-doped BZT10 samples

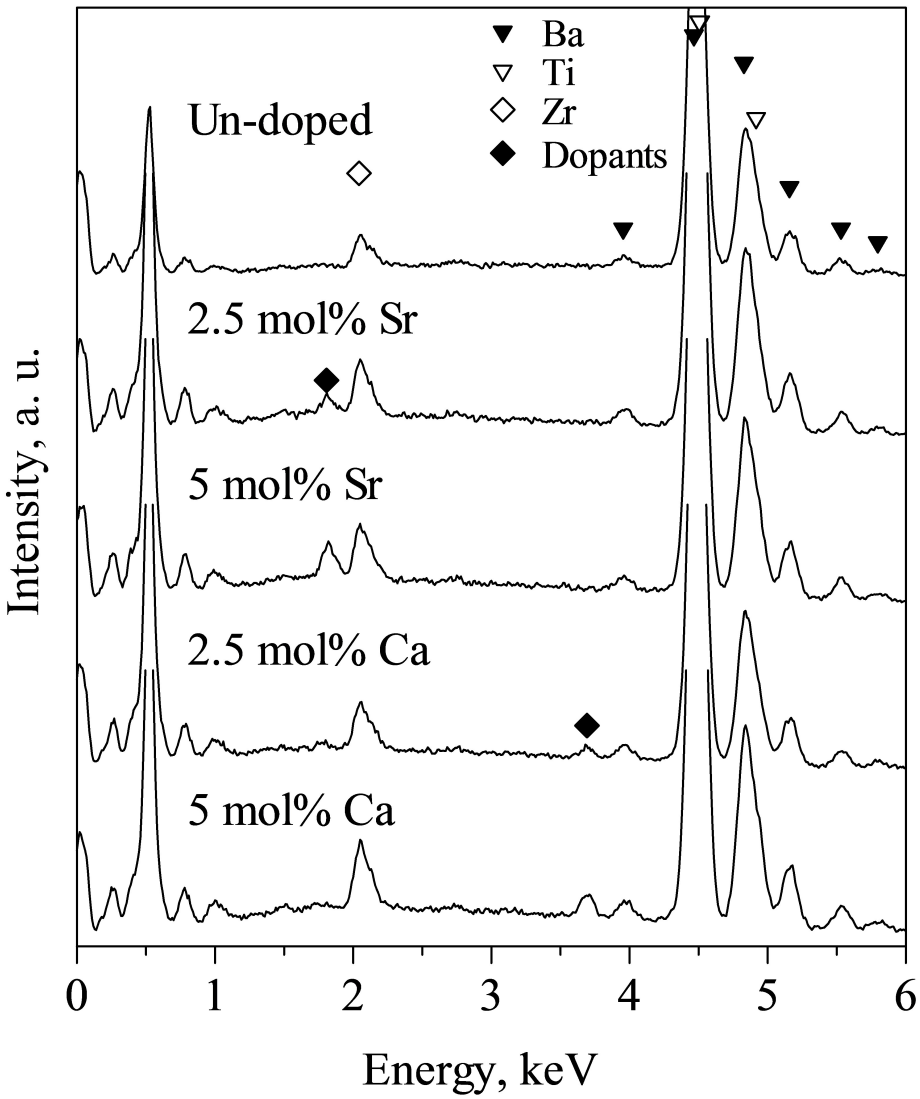

(a) As-sintering, 1400 ℃, 6h

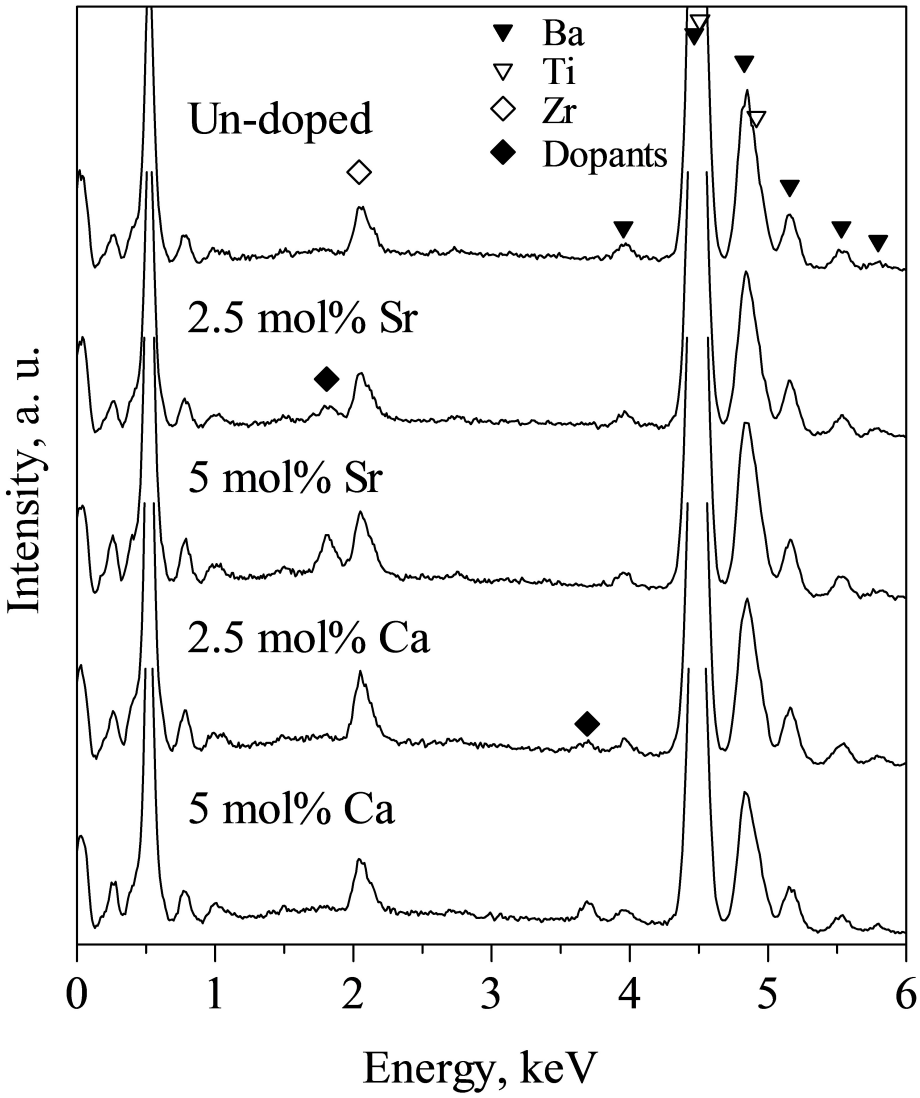

(b) As-annealed, 1250 ℃, 8h

Figure 7.8: EDS patterns of Sr, Ca, and un-doped BZT10 samples

Table. 7.2 shows the tolerance factor calculated using the ionic radii with coordinated numbers X and XII respectively. According to the result, the factor t went close to unity with the lower coordinated number (X over XII), indicating a more stable perovskite structure. Therefore, doping using Sr and Ca induced the formation of Oxygen vacancy, responsible for the large leakage current that will be discussed in the later section.

Table 7.2: Tolerance factors of doped BZT10 samples calculated using different coordination numbers

	Coordination XII	Coordination X
Un-doped	1,055	1,027
2.5 mol% Sr	1,054	1,026
5 mol% Sr	1,053	1,024
2.5 mol% Ca	1,053	1,025
5 mol% Ca	1,051	1,022

7.6 Dielectric properties of Sr and Ca-doped BZT10

Fig. 7.9 shows the dielectric constant and dielectric loss curve of the Sr, Ca, and un-doped BZT10 samples. After doping by Sr and Ca, the diffused dielectric constant peak, corresponding to the mix-relaxor behavior of the un-doped BZT10 sample, split into 2 distinguish peaks: a broad peak at low-temperature corresponding to the ferroelectric-relaxor phase transition and the second peak of relaxor phase to the non-asymmetric cubic corresponding to the paraelectric phase.

In the case of Ca-doped and 2.5 mol% Sr-doped, the first phase transition of ferroelectric-relaxor appeared at around 75 ℃, and the second relaxor-paraelectric happened at 115 ℃. However, the Sr doping increased to 5 mol%, and a reduction of transition temperature was observed, where ferroelectric- relaxor occurred at 70℃and the relaxor-paraelectric at 100 ℃. The phenomenon

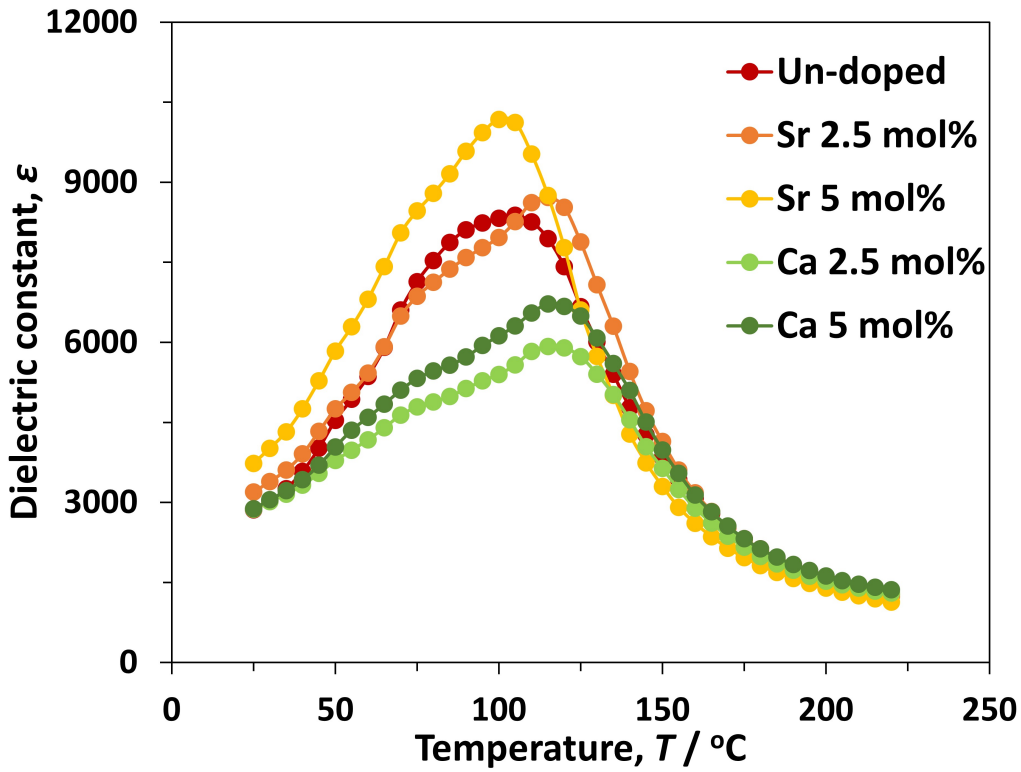

(a) Dielectric constant

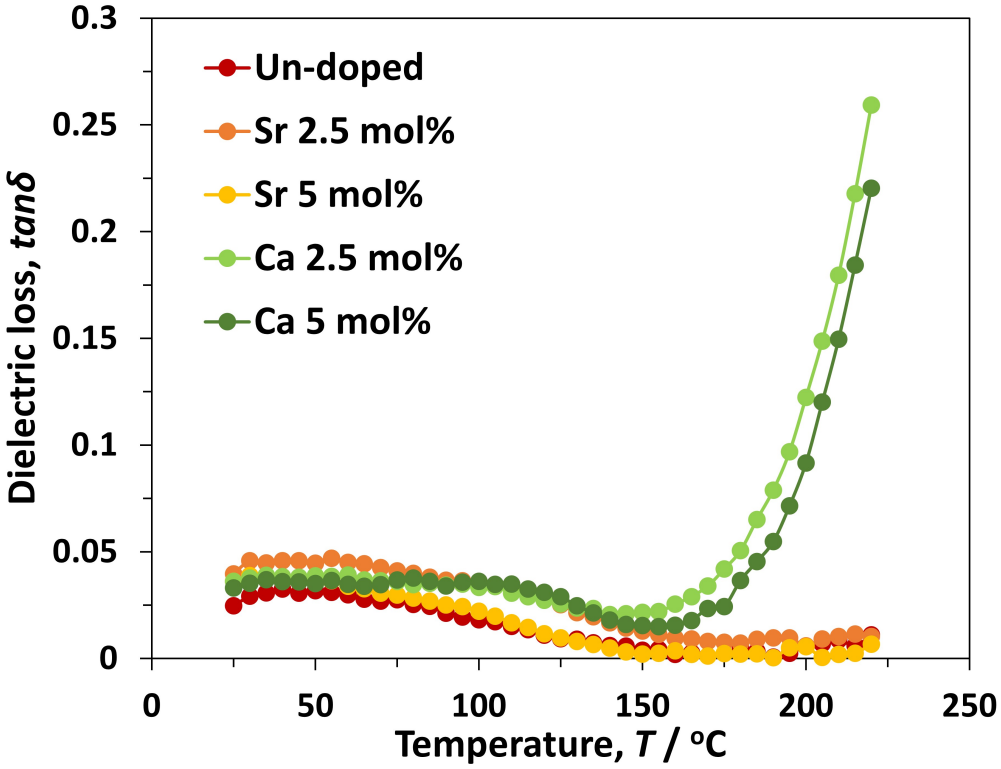

(b) Dielectric loss

Figure 7.9: Temperature dependent dielectric constant and dielectric loss curves of Sr, Ca, and un-doped BZT10 samples

is related to the shrinkage of the crystal lattice as a small ionic radii cation was substituted in the A-site of perovskite. As a result, the material was softening, and the ferroelectric, followed by Curie temperature, decreased. On the other hand, the Ca-doped sample exhibited a Ca off-centering behavior, compensating for the effect of lattice shrinkage. Therefore, as observed in Fig. 7.9a, there were no significant changes in Curie temperature.

Besides that, the dielectric loss of the Ca-doped sample exhibited a higher value compared to the un-doped and Sr-doped samples. The phenomenon was due to the low internal resistance followed by high leakage current, which is well correlated to the prediction of oxygen vacancy by tolerance factor calculation.

Fig. 7.10 shows the hysteresis loop of 4 doped samples, and table 7.3 summarizes the remanent polarization, saturated polarization, and coercive field of each sample at room temperature. Among all, the Sr-doped sample shows a significantly high spontaneous polarization of 18.2 for the 2.5 mol%, and 17.4 μC/cm^3 with the 5 mol% sample. In the contrary, the value obtained in the Ca-doped system was quite low, 11.8 for the 2.5 mol%, and 12.9 μC/cm^3 with the 5 mol%.

Table 7.3: Coercive field, remanent, and saturated polarization of 4 doped samples

	2.5 mol% Sr	5 mol% Sr	2.5 mol% Ca	5 mol% Ca
E_c [kV/m]	162.7	173.2	195.5	144.0
P_r [μC/cm^3]	18.2	17.4	11.8	12.9
P_s [μC/cm^3]	4.5	6.2	2.5	2.8

At 60 ℃all samples exhibit a large variation in remanent polarization and coercive field which might correspond to the ferroelectric-relaxor phase transition. 2.5 mol% Sr shows an polarization change of 1.3 μC/cm^3 and coercive field reduction of 36.3 kV/m when temperature go from 50 to 60 ℃. These numbers in 5 mol% Sr-doped samples was also 1.3 and 37.3, 2.5 mol% Ca were 0.1 and 16.7, and 2.5 mol% Ca were 0.9 μC/cm^3 and 62.7 kV/m respectively. Upon 100 ℃, all samples gradually shifted to a slim non-linear shape of

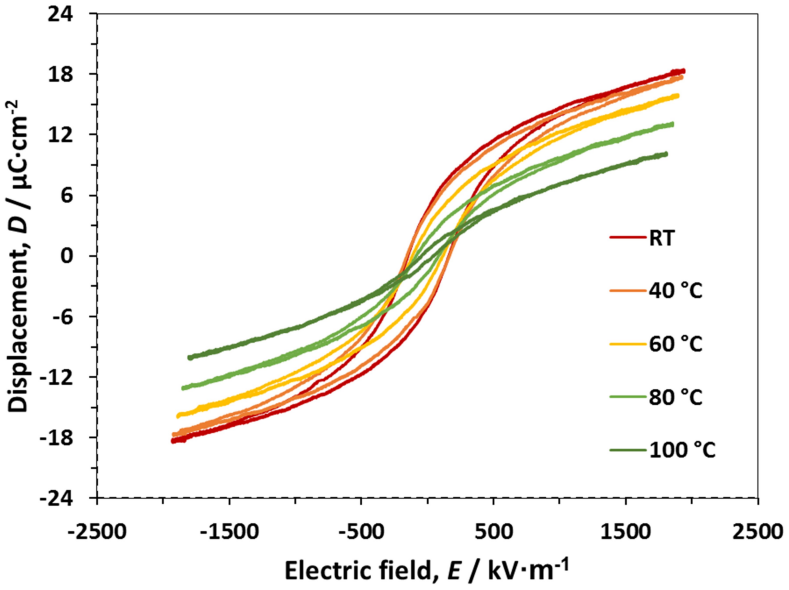

(a) 2.5 mol% Sr-doped

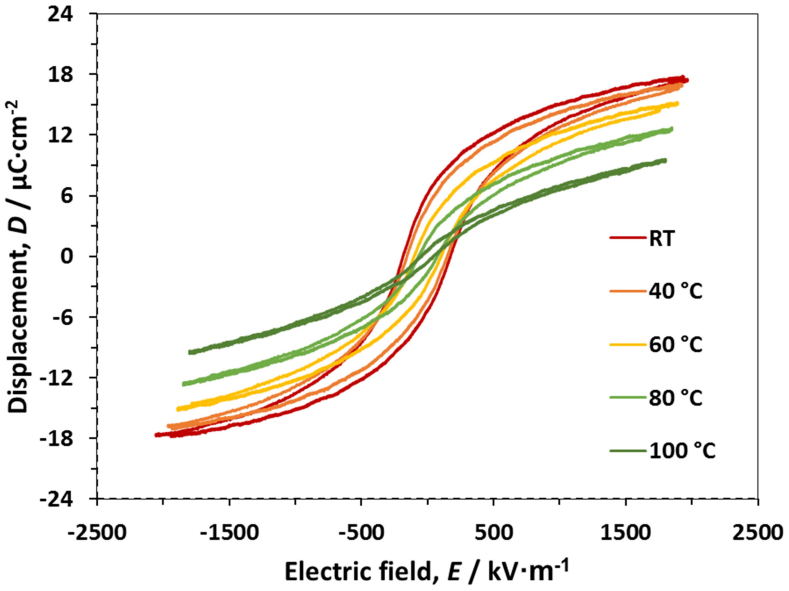

(b) 5 mol% Sr-doped

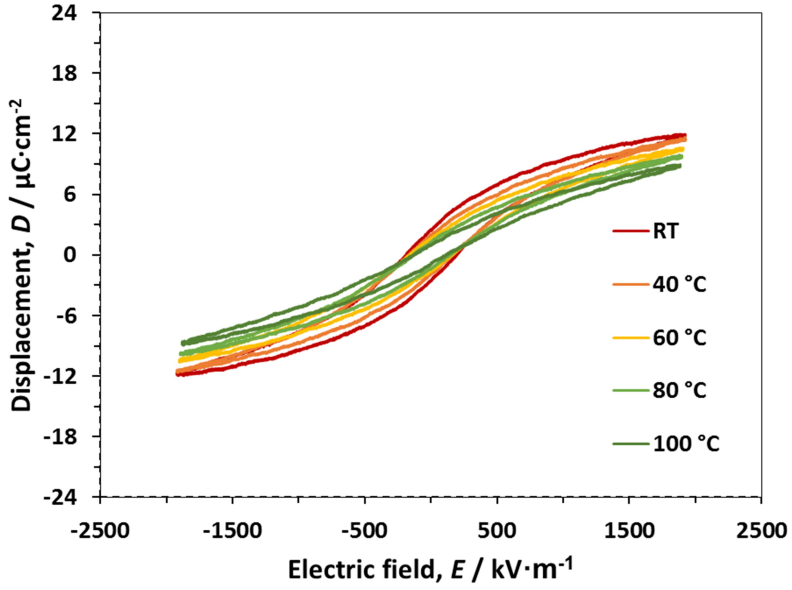

(c) 2.5 mol% Ca-doped

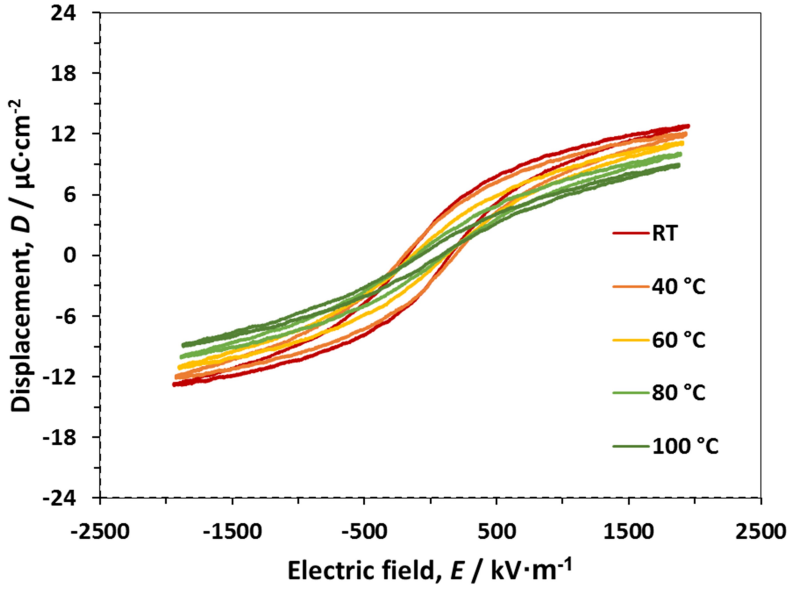

(d) 5 mol% Ca-doped

Figure 7.10: Temperature dependent hysteresis loop of 4 doped BZT10 samples

paraelectric phase. The early ferroelectric-relaxor transition was responsible for the peak split observed in the dielectric constant curve.

7.7 Power generation of Sr and Ca-doped BZT10

Fig. 7.11 shows the power generation of the Sr and doped BZT10 in comparison with the un-doped sample. Sr doping enhances the energy density from 2.9, 5.3, 10.6 mJ/cm^3 to 3.8, 7.5, 14.7 mJ/cm^3 and 4.4, 8.9, 15.8 mJ/cm^3 corresponding to the 2.5 mol% and 5 mol% Sr respectively. However, Ca doping caused a significant drop in power generation. The value decreased to 0.7, 0.7, and 0.4 mJ/cm^3 for the 2.5 mol% doped sample, 1.0, 0.3, and -0.2 mJ/cm^3 (energy consumes) for the 5 mol% sample.

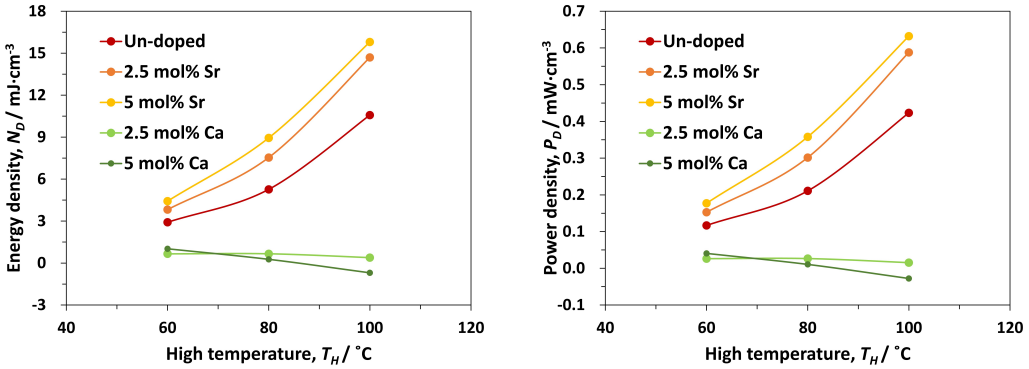

(a) Energy density (b) Power density

Figure 7.11: Power generation of doped BZT10 samples

Fig. 7.12 shows the cycle loop of each sample. The enhancement of remanent polarization and spontaneous polarization which were also observed in the hysteresis loop is responsible for the increase of power generation in the Sr-doped sample. Furthermore, the Sr doping also improved pyroelectricity, causing the electric field during the isodisplacement processes to increase faster, especially for large temperature ranges. On contrary, Ca-doped not only decrease the remanent polarization and spontaneous polarization of the BZT10 system but also induced a large leakage current which was observed in high dielectric loss behavior. The effect of leakage current especially kicked in the high temperature, causing a continuous drop in power generation.

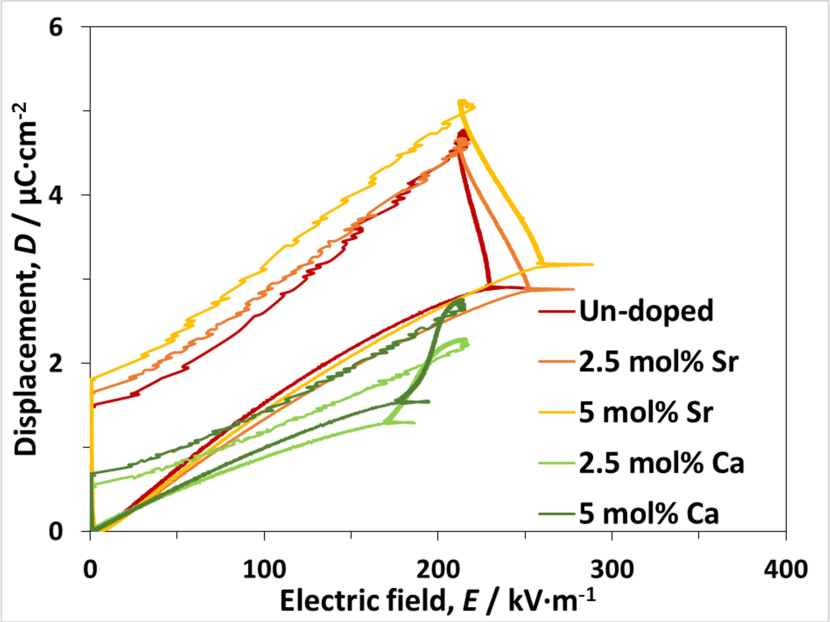

(a) Temperature range 40-60 ℃

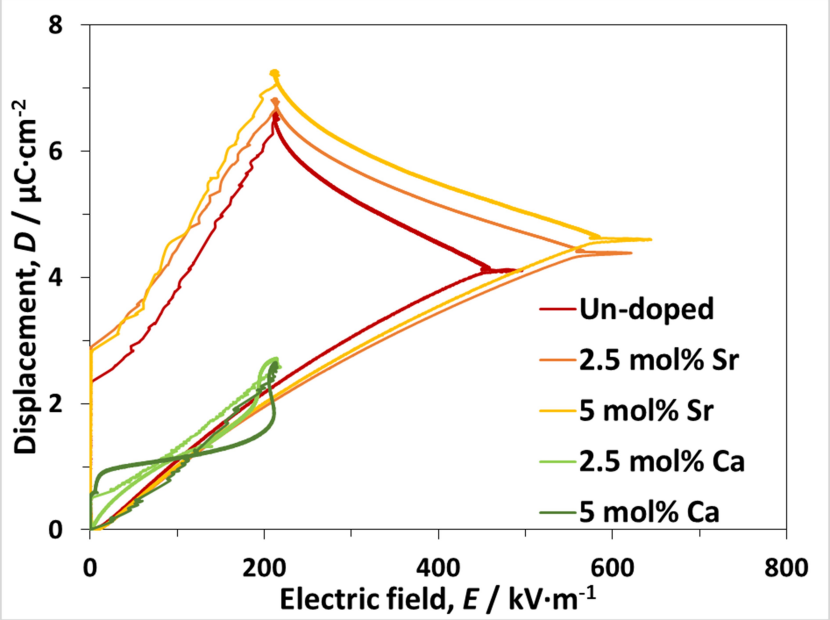

(b) Temperature range 40-100 ℃

Figure 7.12: Kim cycle loop of doped BZT10 samples

Fig. 7.13 shows the power generation test using the conventional Olsen cycle of 4 doped samples. Again, the Sr-doped successfully enhanced the pyroelectric conversion ability of the BZT10 sample and increased the energy density from 3.1, 4.3, 5.7 mJ/cm^3 to 3.6, 4.8, 6.2 mJ/cm^3 with 2.5 mol% Sr and 4.3, 5.5, 7.4 mJ/cm^3 in the case of 5 mol%. In contrast, the Ca doped reduced the energy density to 1.2, 1.3, and to 0 mJ/cm^3 with 2.5 mol% doping, 1.2, 1.5, and down to -1.4 mJ/cm^3 with the 5 mol%.

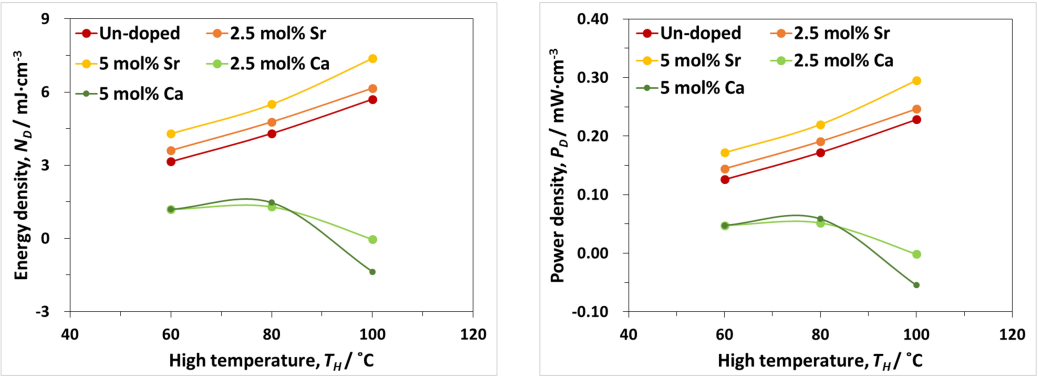

(a) Energy density (b) Power density

Figure 7.13: Power generation with Olsen cycle of doped BZT10 samples

In comparison to the Olsen cycle, the power generation of un-doped and Sr-doped exhibited a higher value and increased quickly with the rise of high temperature. The power generation with the Kim cycle increased 3.6, 3.8, and 3.6 times for un-doped, 2.5 mol%, and 5 mol% respectively, with the high-temperature going from 60 ℃ to 100 ℃. These values in the Olsen cycle were 1.8, 1.7, and 1.7 respectively. However, in the case of Ca doped sample, the power generation using the Olsen cycle was higher than the Kim cycle at low temperatures. The values were 1.2, 1.3 mJ/cm^3 and 1.2, 1.5 mJ/cm^3 for 2.5 and 5 mol%, respectively (high-temperature T_H = 60, 80 ℃). Therefore, in terms of some samples with high internal resistance, the Olsen cycle would be a more efficient choice for low-grade heat recovery.

Fig. 7.14 shows the Olsen cycle loop of the 4 doped samples. The enhancement in remanent and spontaneous polarization once again raises the pyroelectric heat-to-electricity potential of the Sr-doped samples. In the case of Ca-

doped, the internal resistance induced a large leakage current, which caused a loop-cross and reverse cycle as observed in Fig. 7.14b.

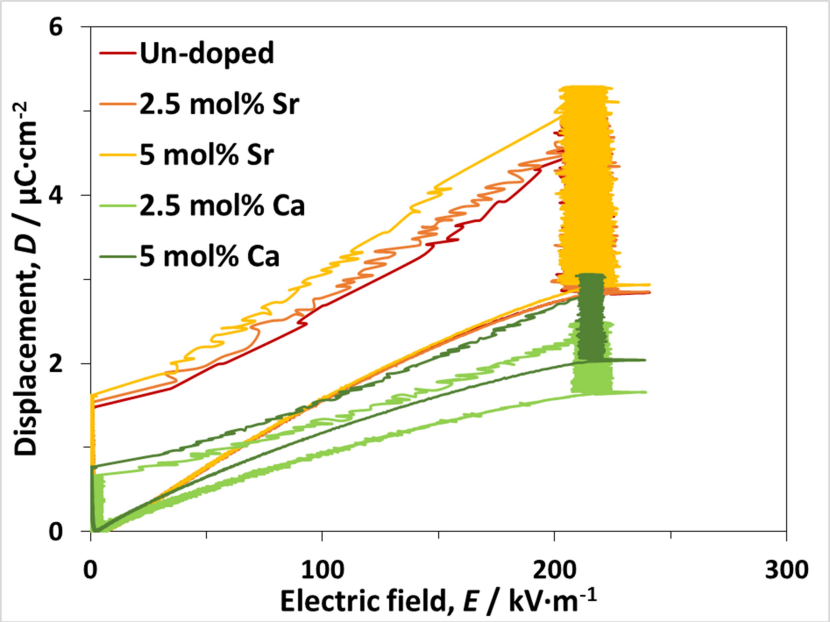

(a) Temperature range 40-60 ℃

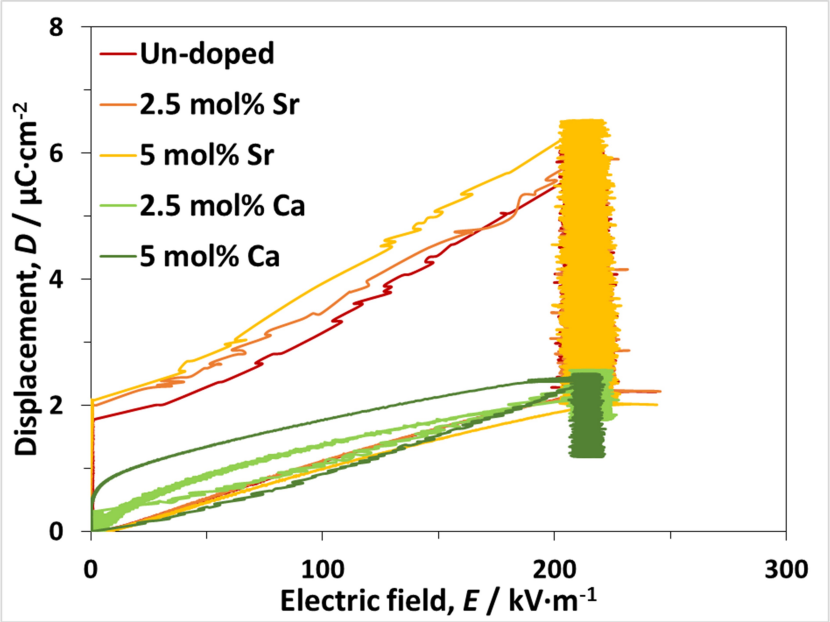

(b) Temperature range 40-100 ℃

Figure 7.14: Olsen cycle loop of doped BZT10 samples

Chapter 8

Conclusion

The objective of developing a lead-free pyroelectric material with phase transition temperature below 130 ℃ for application in low-grade waste heat to electricity recycling was fulfilled in this thesis through 8 chapters.

Chapter 1 explained the current situation of global usage energy and reveal the 52% potential of waste heat available for recovery. Multiple attempts were made in many countries and areas, which achieved some success in waste heat management. However, low-grade is still left out there and gathering notices from countries, and people for its high potential. The need meets the potential has led our group to develop a waste heat recovery technology covering the high-potential low-grade source.

In chapter 2, multiple waste heat management technologies were reviewed, focusing on three strategies. Recycling with its mobility, and variation got our attention to be able to apply it in multiple different scenarios. Among that, the developing Internet of Things, robots, and artificial intelligence are the biggest targets. To solve the crisis caused by battery maintenance and replacement, pyroelectric with the flexibility for working with a single heat source configuration and targeting different low-grade heat, was chosen as the technology to investigate in this research.

Therefore, also in this chapter, the thesis pointed out the main objective of our research is to develop a pyroelectric material with phase transition temperature below 130 ℃ for application in low-grade waste heat to electricity recycling. The research faced two big problems: 1) Lacking below 130 ℃ solution and 2) Lead toxicity. Solving these two issues was the novelty of this

thesis, making the research achieve sustainable development goals 7 and 12, and supplying a clean, efficient solution to the future IoT.

Consequently, chapter 3 chose the lead-free $Ba(Zr,Ti)O_3$ with a high remanent, saturated polarization for a potential large polarization variation with temperature, the low coercive field for low input energy, mix ferroelectric-relaxor behavior for low phase transition temperature and large application range, and finally, a high piezoelectric effect with the Ca dopant.

In chapter 4, the $Ba(Zr,Ti)O_3$ was successfully fabricated into a single phase, high-density bulk. The sample exhibit a rhombohedral structure with a mix of ferroelectric-relaxor behavior. Therefore, a broad dielectric constant curve and a slim hysteresis loop with a low coercive field were achieved. Furthermore, a high polarization variation was obtained during the ferroelectric-relaxor phase transition for a potential heat to electricity.

Chapter 5 investigate the pyroelectric heat to the electricity of the BZT sample under a single heat source configuration. Since the natural heat source is a combination of different frequencies and temperature ranges, the BZT10 sample under three frequencies and temperature span was tested. The result showed that the Kim cycle is efficient in improving the pyroelectric conversion ability of the BZT10 sample under highly fluctuating, large different sources. A power density of 15.0 mW/cm^3 was achieved at $f = 0.1$ Hz and $\Delta T = 40$ ℃. Additional tuning using the electrical factor of electric field application and the thermal factor of sample thicknesses was investigated, revealing the potential for further improvement with these two factors. Consequently, an actual output power density based on the discharge through the resistor was measured, and a maximum power density of 13.7 mW/cm^3 was achieved. This power is able to supply energy to a Bluetooth Low Energy for IoT applications.

Chapter 6 studied the pyroelectric heat to the electricity of the BZT sample with a cooling assist configuration. Since the sample exhibited a strong sensitivity against high fluctuating conditions as studied in chapter 5, an optimized heating time of 12.5s and cooling time of 22.5s was investigated and applied. At a low temperature of 20 ℃ and a high temperature of 120 ℃, the sample resulted in an energy density of 504 mJ/cm^3, the highest value reported for bulk type lead-free materials in the BT family.

After chapters 5 and 6, the BZT10 samples showed multiple properties which can overcome the conventional materials and see the application in some low-energy consumed IoT devices. In chapter 7, the pyroelectric conversion was again enhanced using 2 isovalent dopants of Sr and Ca. The Sr doping successfully reached a high remanent and saturated polarization value, hence, improving the conversion ability 1.4 and 1.5 times with the Kim cycle, and 1.1 and 1.3 times with the Olsen cycle for the 2.5 mol% and 5 mol% dopants respectively. Unfortunately, the Ca dopants downgraded the conversion ability to a significantly low value in both cases. Nevertheless, Sr-doping would be a promising method for enhancing low-grade waste heat recovery with the pyroelectricity of the BZT10 sample.

Appendix A

Output power density of BZT10 samples

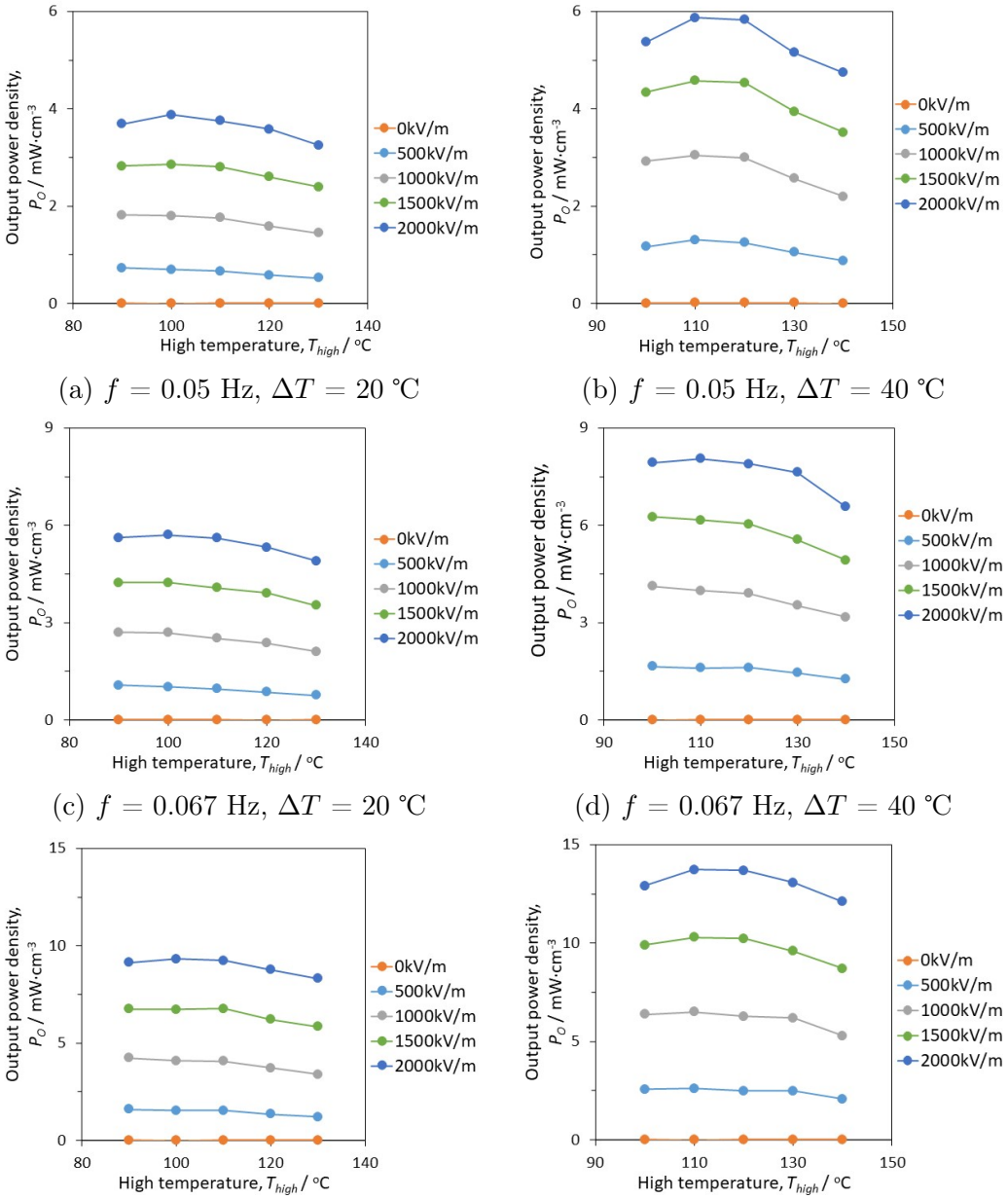

(a) $f = 0.05$ Hz, $\Delta T = 20$ ℃ (b) $f = 0.05$ Hz, $\Delta T = 40$ ℃

(c) $f = 0.067$ Hz, $\Delta T = 20$ ℃ (d) $f = 0.067$ Hz, $\Delta T = 40$ ℃

(e) $f = 0.1$ Hz, $\Delta T = 20$ ℃ (f) $f = 0.1$ Hz, $\Delta T = 40$ ℃

Figure A.1: Output power density of the 0.4-mm thick BZT10 sample measured a simulated single heat source fluctuating at $f = 0.05$ Hz, 0.067 Hz, 0.1 Hz and $\Delta T = 20$ ℃, 40 ℃.

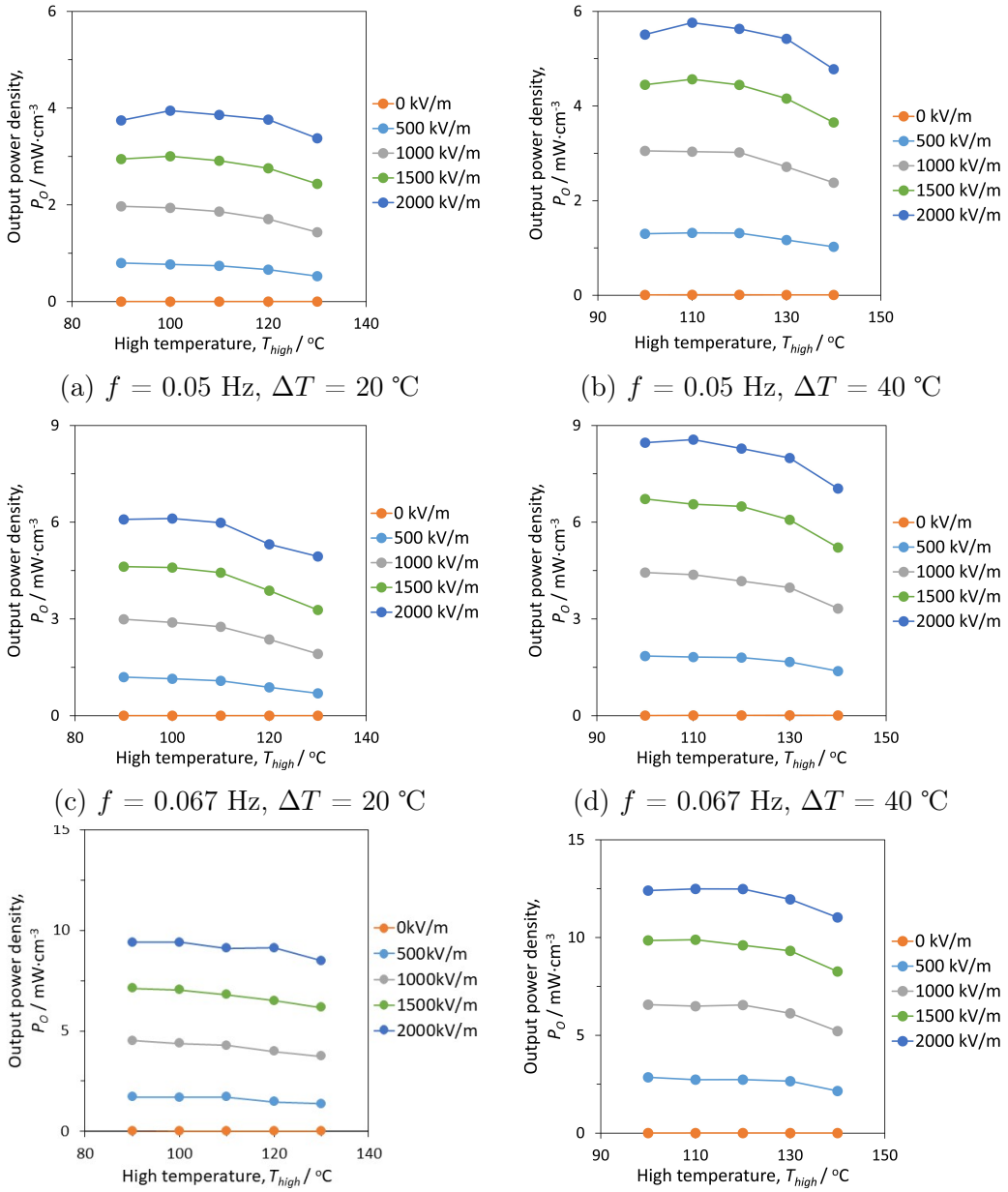

(a) $f = 0.05$ Hz, $\Delta T = 20$ ℃ (b) $f = 0.05$ Hz, $\Delta T = 40$ ℃

(c) $f = 0.067$ Hz, $\Delta T = 20$ ℃ (d) $f = 0.067$ Hz, $\Delta T = 40$ ℃

(e) $f = 0.1$ Hz, $\Delta T = 20$ ℃ (f) $f = 0.1$ Hz, $\Delta T = 40$ ℃

Figure A.2: Output power density of the 0.5-mm thick BZT10 sample measured a simulated single heat source fluctuating at $f = 0.05$ Hz, 0.067 Hz, 0.1 Hz and $\Delta T = 20$ ℃, 40 ℃.

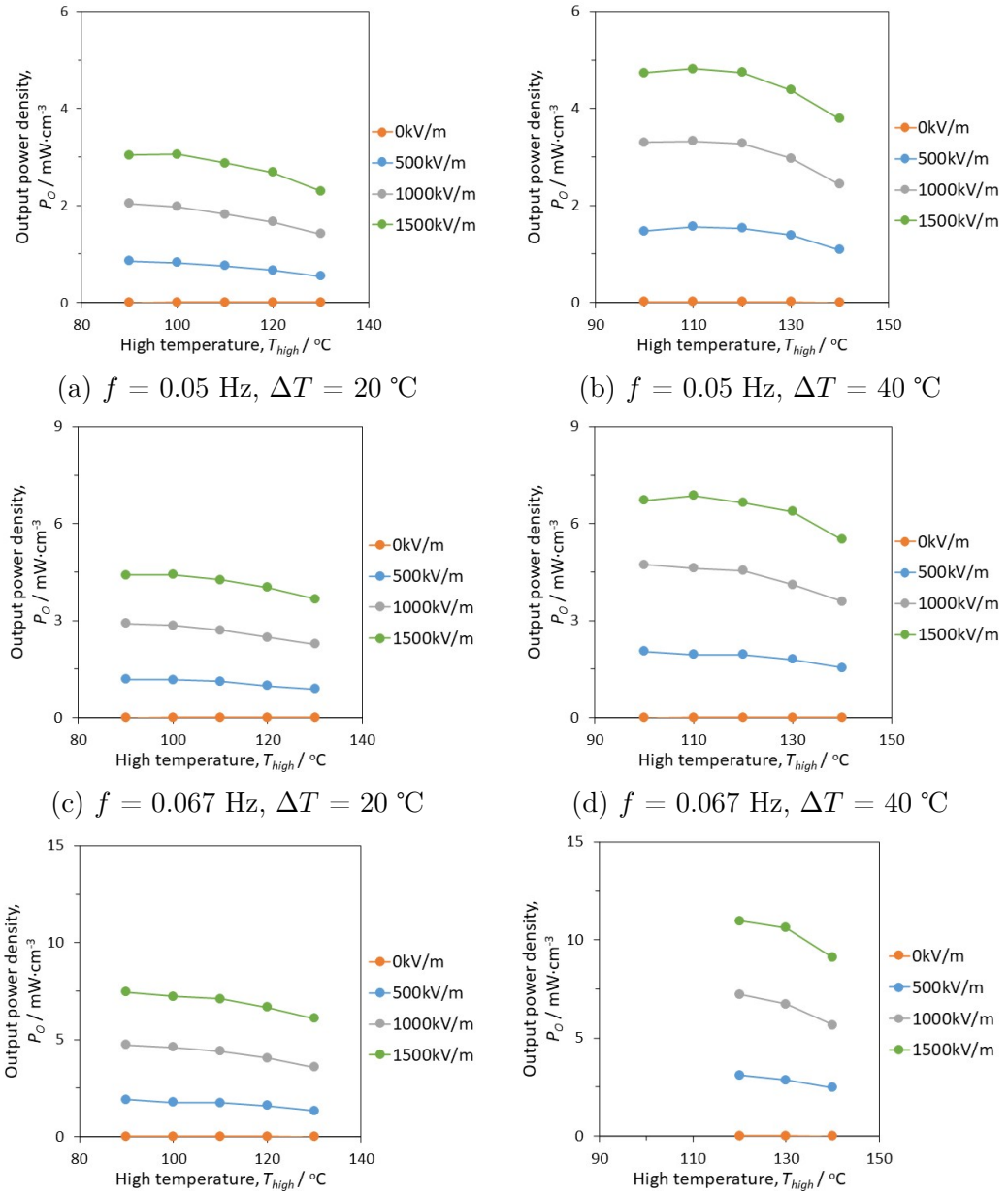

(a) $f = 0.05$ Hz, $\Delta T = 20$ ℃ (b) $f = 0.05$ Hz, $\Delta T = 40$ ℃

(c) $f = 0.067$ Hz, $\Delta T = 20$ ℃ (d) $f = 0.067$ Hz, $\Delta T = 40$ ℃

(e) $f = 0.1$ Hz, $\Delta T = 20$ ℃ (f) $f = 0.1$ Hz, $\Delta T = 40$ ℃

Figure A.3: Output power density of the 0.6-mm thick BZT10 sample measured a simulated single heat source fluctuating at $f = 0.05$ Hz, 0.067 Hz, 0.1 Hz and $\Delta T = 20$ ℃, 40 ℃.

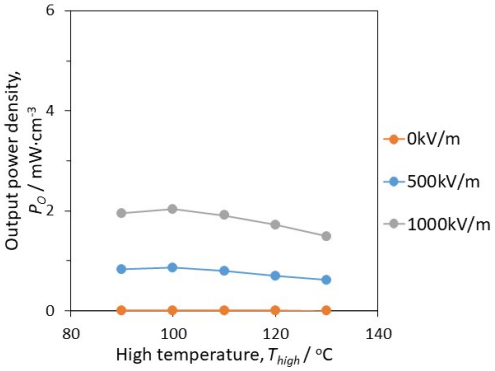

(a) $f = 0.05$ Hz, $\Delta T = 20$ ℃

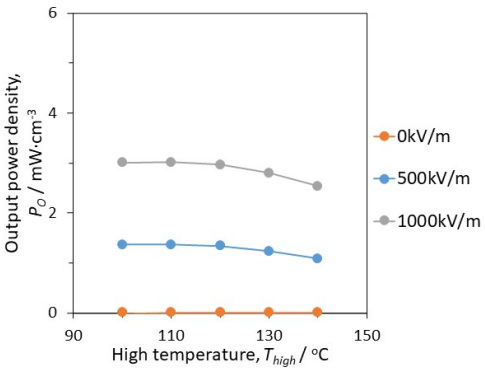

(b) $f = 0.05$ Hz, $\Delta T = 40$ ℃

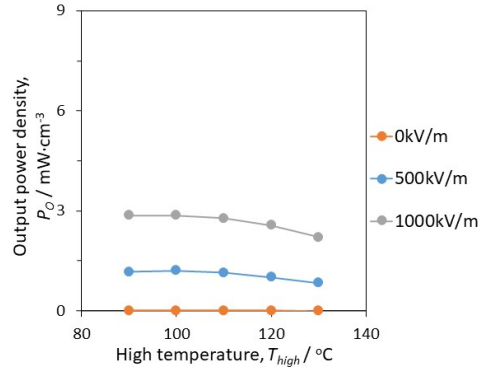

(c) $f = 0.067$ Hz, $\Delta T = 20$ ℃

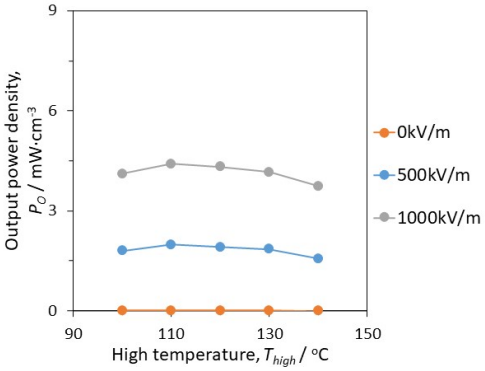

(d) $f = 0.067$ Hz, $\Delta T = 40$ ℃

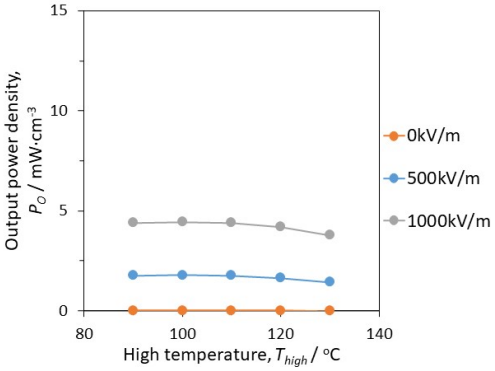

(e) $f = 0.1$ Hz, $\Delta T = 20$ ℃

Figure A.4: Output power density of the 0.7-mm thick BZT10 sample measured a simulated single heat source fluctuating at $f = 0.05$ Hz, 0.067 Hz, 0.1 Hz and $\Delta T = 20$ ℃, 40 ℃.

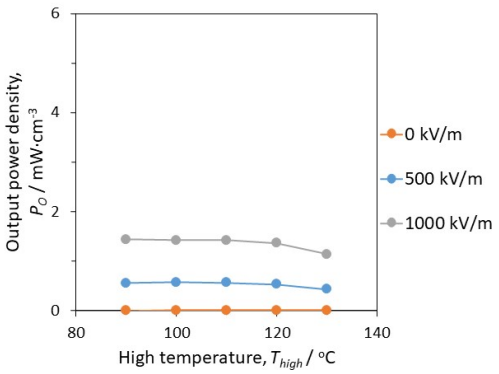

(a) $f = 0.05$ Hz, $\Delta T = 20$ °C

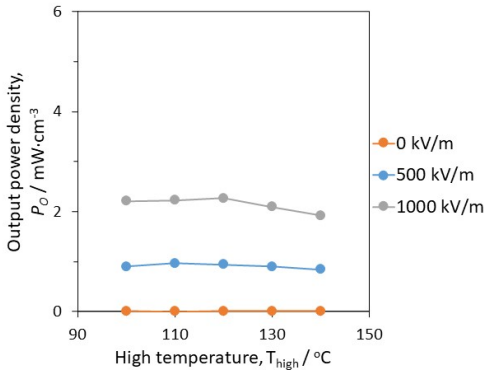

(b) $f = 0.05$ Hz, $\Delta T = 40$ °C

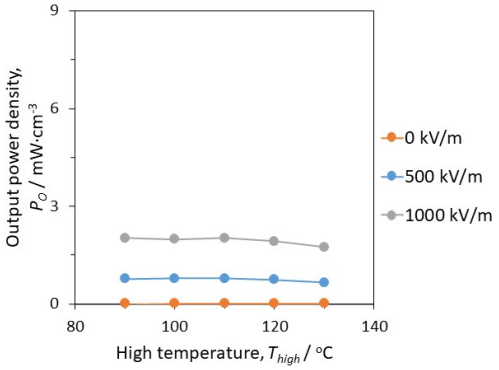

(c) $f = 0.067$ Hz, $\Delta T = 20$ °C

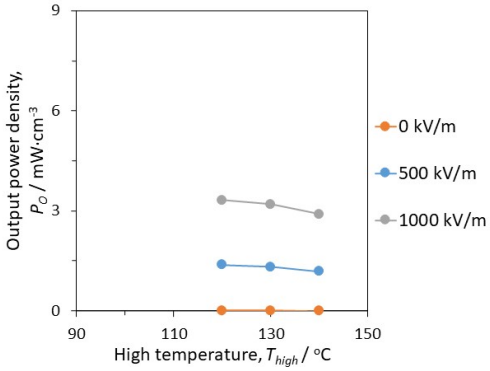

(d) $f = 0.067$ Hz, $\Delta T = 40$ °C

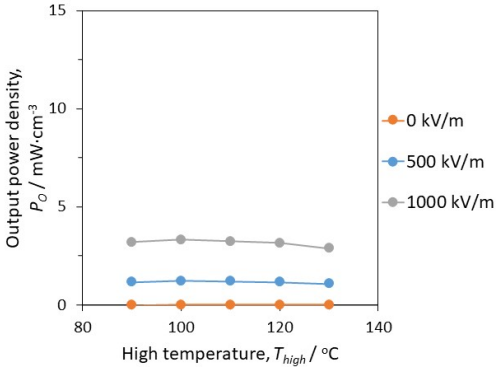

(e) $f = 0.1$ Hz, $\Delta T = 20$ °C

Figure A.5: Output power density of the 0.8-mm thick BZT10 sample measured a simulated single heat source fluctuating at $f = 0.05$ Hz, 0.067 Hz, 0.1 Hz and $\Delta T = 20$ °C, 40 °C.

Bibliography

[1] J.M. Cullen, J.M. Allwood, and E.H. Borgstein. "Reducing Energy Demand: What Are the Practical Limits?" In: *Environmental Science & Technology* 45.4 (2011), pp. 1711–1718. DOI: https://doi.org/10.1021/es102641n.

[2] C.M. Summers. "The conversion of energy". In: *Scientific American* 225.3 (1971), pp. 148–163. URL: http://www.jstor.org/stable/24923123.

[3] M. Schmidt. "The Sankey Diagram in Energy and Material Flow Management". In: *Journal of Industrial Ecology* 12.1 (2008), pp. 82–94. DOI: https://doi.org/10.1111/j.1530-9290.2008.00004.x.

[4] D.Y. Goswami and F. Kreith, eds. *Energy Conversion*. Boca Raton: CRC Press, 2007. DOI: https://doi.org/10.1201/9781420044324.

[5] G. Petrecca. "Introduction". In: *Energy Conversion and Management: Principles and Applications*. Cham: Springer International Publishing, 2014, pp. 1–5. DOI: https://doi.org/10.1007/978-3-319-06560-1_1.

[6] M. González-Torres et al. "A cross-country review on energy efficiency drivers". In: *Applied Energy* 289 (2021), p. 116681. DOI: https://doi.org/10.1016/j.apenergy.2021.116681.

[7] N. Eyre. "Energy efficiency in the energy transition". In: *Eceee 2019 Summer Study on energy efficiency: Is efficient sufficient?* (2019), pp. 247–254.

[8] P.T. Landsberg and G. Tonge. "Thermodynamic energy conversion efficiencies". In: *Journal of Applied Physics* 51.7 (1980), R1–R20. DOI: https://doi.org/10.1063/1.328187.

[9] M. Castro Oliveira et al. “Review on Energy Efficiency Progresses, Technologies and Strategies in the Ceramic Sector Focusing on Waste Heat Recovery”. In: *Energies* 13.22 (2020), p. 6096. DOI: https://doi.org/10.3390/en13226096.

[10] H. Khayyam et al. “Improving energy efficiency of carbon fiber manufacturing through waste heat recovery: A circular economy approach with machine learning”. In: *Energy* 225 (2021), p. 120113. DOI: https://doi.org/10.1016/j.energy.2021.120113.

[11] J.M. Cullen and J.M. Allwood. “The efficient use of energy: Tracing the global flow of energy from fuel to service”. In: *Energy Policy* 38.1 (2010), pp. 75–81. DOI: https://doi.org/10.1016/j.enpol.2009.08.054.

[12] Q. Bian. “Waste heat: the dominating root cause of current global warming”. In: *Environmental Systems Research* 9.8 (2020), pp. 1–11. DOI: https://doi.org/10.1186/s40068-020-00169-2.

[13] L. Paoli, R. Lupton, and J. Cullen. “Probabilistic model allocating primary energy to end-use devices”. In: *Energy Procedia* 142 (2017), pp. 2441–2447. DOI: https://doi.org/10.1016/j.egypro.2017.12.180.

[14] A. Grubler et al. “Energy Primer”. In: *Global Energy Assessment*. Cambridge: Cambridge University Press, 2012, pp. 99–150. DOI: https://doi.org/10.1017/CBO9780511793677.

[15] J.M. Cullen and J.M. Allwood. “Theoretical efficiency limits for energy conversion devices”. In: *Energy* 35.5 (2010), pp. 2059–2069. DOI: https://doi.org/10.1016/j.energy.2010.01.024.

[16] C.H. Dyer et al. “Enabling technologies for industrial energy demand management”. In: *Energy Policy* 36.12 (2008), pp. 4434–4443. DOI: https://doi.org/10.1016/j.enpol.2008.09.028.

[17] G.P. Hammond. “Towards sustainability: energy efficiency, thermodynamic analysis, and the ‘two cultures’”. In: *Energy Policy* 32.16 (2004), pp. 1789–1798. DOI: https://doi.org/10.1016/j.enpol.2003.09.015.

[18] A.B. Jaffe and R.N. Stavins. “The energy-efficiency gap What does it mean?” In: *Energy Policy* 22.10 (1994), pp. 804–810. DOI: https://doi.org/10.1016/0301-4215(94)90138-4.

[19] S.J. DeCanio. "Barriers within firms to energy-efficient investments". In: *Energy Policy* 21.9 (1993), pp. 906–914. DOI: https://doi.org/10.1016/0301-4215(93)90178-I.

[20] S.J. DeCanio. "The efficiency paradox: bureaucratic and organizational barriers to profitable energy-saving investments". In: *Energy Policy* 26.5 (1998), pp. 441–454. DOI: https://doi.org/10.1016/S0301-4215(97)00152-3.

[21] International Energy Agency. *World Energy Outlook 2021*. 2021, p. 386. DOI: https://doi.org/10.1787/14fcb638-en.

[22] International Energy Agency. *World Energy Outlook 2010*. 2010, p. 738. DOI: https://doi.org/https://doi.org/10.1787/weo-2010-en.

[23] International Energy Agency. *World Energy Outlook 2019*. 2019, p. 810. DOI: https://doi.org/https://doi.org/10.1787/caf32f3b-en.

[24] International Energy Agency. *World Energy Outlook 2020*. 2020, p. 464. DOI: https://doi.org/https://doi.org/10.1787/557a761b-en.

[25] R. Fassler. "Efficiency Regulations: Driving power conversion efficiency designs". In: *IEEE Power Electronics Magazine* 4.1 (2017), pp. 19–24. DOI: https://doi.org/10.1109/MPEL.2016.2642518.

[26] D.M. Gann, Y. Wang, and R. Hawkins. "Do regulations encourage innovation? - the case of energy efficiency in housing". In: *Building Research & Information* 26.5 (1998), pp. 280–296. DOI: https://doi.org/10.1080/096132198369760.

[27] J. Malinowski et al. "Motor and Drive-System Efficiency Regulations: Review of Regulations in the United States and Europe". In: *IEEE Industry Applications Magazine* 23.1 (2017), pp. 34–41. DOI: https://doi.org/10.1109/MIAS.2016.2600723.

[28] M.A. Rosen, I. Dincer, and M. Kanoglu. "Role of exergy in increasing efficiency and sustainability and reducing environmental impact". In: *Energy Policy* 36.1 (2008), pp. 128–137. DOI: https://doi.org/10.1016/j.enpol.2007.09.006.

[29] I.S. Ertesvåg. "Society exergy analysis: a comparison of different societies". In: *Energy* 26.3 (2001), pp. 253–270. DOI: https://doi.org/10.1016/S0360-5442(00)00070-0.

[30] N. Nakićenović, P.V. Gilli, and R. Kurz. “Regional and global exergy and energy efficiencies”. In: *Energy* 21.3 (1996), pp. 223–237. DOI: https://doi.org/10.1016/0360-5442(96)00001-1.

[31] G.M. Reistad. “Available Energy Conversion and Utilization in the United States”. In: *Journal of Engineering for Power* 97.3 (1975), pp. 429–434. DOI: https://doi.org/10.1115/1.3446026.

[32] C. Forman et al. “Estimating the global waste heat potential”. In: *Renewable and Sustainable Energy Reviews* 57 (2016), pp. 1568–1579. DOI: https://doi.org/10.1016/j.rser.2015.12.192.

[33] A. Firth, B. Zhang, and A. Yang. “Quantification of global waste heat and its environmental effects”. In: *Applied Energy* 235 (2019), pp. 1314–1334. DOI: https://doi.org/10.1016/j.apenergy.2018.10.102.

[34] A.S. Rattner and S. Garimella. “Energy harvesting, reuse and upgrade to reduce primary energy usage in the USA”. In: *Energy* 36.10 (2011), pp. 6172–6183. DOI: https://doi.org/10.1016/j.energy.2011.07.047.

[35] R. Repice, ed. *Annual energy review 2009*. Washington, DC: U.S. Energy Information Administration, 2010.

[36] I. Johnson, W.T. Choate, and A. Davidson. *Waste Heat Recovery. Technology and Opportunities in U.S. Industry*. Tech. rep. 2008. DOI: https://doi.org/10.2172/1218716.

[37] M. Luberti et al. “An estimate of the ultralow waste heat available in the European Union”. In: *Energy* 238.C (2022), p. 121967. DOI: https://doi.org/10.1016/j.energy.2021.121967.

[38] J. Patronen and H. Uimonen. *Report for the Ministry of Economic Affairs and Employment: Overview of the potential for waste heat and cost-benefit analysis of efficient heating in accordance with the energy efficiency directive*. Tech. rep. 2020.

[39] Thermal management materials and technology research association. “産業分野の排熱実態調査報告書. [Waste heat survey report in the industrial field]”. In: *The energy conservation* 71.6 (2019), pp. 66–77.

[40] Thermal management materials and technology research association. “活用が期待される、未利用熱. [Unused heat expected to be utilized]”. In: *Asahi Research Center Watching* (2019). URL: https://arc.asahi-kasei.co.jp/member/watching/pdf/w_298-02.pdf.

[41] E. Lanzi, E. Verdolini, and I. Haščič. "Efficiency improving fossil fuel technologies for electricity generation: Data selection and trends". In: *Energy Policy* 39.11 (2011), pp. 7000–7014. DOI: https://doi.org/10.1016/j.enpol.2011.07.052.

[42] M. Bilgili et al. "An overview of renewable electric power capacity and progress in new technologies in the world". In: *Renewable and Sustainable Energy Reviews* 49 (2015), pp. 323–334. DOI: https://doi.org/10.1016/j.rser.2015.04.148.

[43] L.T.C. Montoya et al. "Wind power plant planning and modeling". In: *Hybrid Renewable Energy Systems and Microgrids*. Ed. by E. Kabalci. Cambridge: Academic Press, 2021. Chap. 8, pp. 259–312. DOI: https://doi.org/10.1016/B978-0-12-821724-5.00012-X.

[44] E. Worrell et al. "Industrial energy efficiency and climate change mitigation". In: *Energy Efficiency* 2 (2008), pp. 109–123. DOI: https://doi.org/10.1007/s12053-008-9032-8.

[45] K. Blok. "Improving Energy Efficiency by Five Percent and More per Year?" In: *Journal of Industrial Ecology* 8.4 (2004), pp. 87–99. DOI: https://doi.org/10.1162/1088198043630478.

[46] X. Cao, X. Dai, and J. Liu. "Building energy consumption status worldwide and the state-of-the-art technologies for zero-energy buildings during the past decade". In: *Energy and Buildings* 128 (2016), pp. 198–213. DOI: https://doi.org/10.1016/j.enbuild.2016.06.089.

[47] S. Kobayashi, S. Plotkin, and S. Ribeiro. "Energy efficiency technologies for road vehicles". In: *Energy Efficiency* 2 (2009), pp. 125–137. DOI: https://doi.org/10.1007/s12053-008-9037-3.

[48] D. Feroldi, M. Serra, and J. Riera. "Energy Management Strategies based on efficiency map for Fuel Cell Hybrid Vehicles". In: *Journal of Power Sources* 190.2 (2009), pp. 387–401. DOI: https://doi.org/10.1016/j.jpowsour.2009.01.040.

[49] H. Jouhara et al. "Waste heat recovery technologies and applications". In: *Thermal Science and Engineering Progress* 6 (2018), pp. 268–289. DOI: https://doi.org/10.1016/j.tsep.2018.04.017.

[50] P. Donnellan, K. Cronin, and E. Byrne. "Recycling waste heat energy using vapour absorption heat transformers: A review". In: *Renewable and Sustainable Energy Reviews* 42 (2015), pp. 1290–1304. DOI: https://doi.org/10.1016/j.rser.2014.11.002.

[51] Z. Xu and R. Wang. "Absorption heat pump for waste heat reuse: current states and future development". In: *Frontiers in Energy* 11 (2017), pp. 414–436. DOI: https://doi.org/10.1007/s11708-017-0507-1.

[52] C. Arpagaus et al. "High temperature heat pumps: Market overview, state of the art, research status, refrigerants, and application potentials". In: *Energy* 152 (2018), pp. 985–1010. DOI: https://doi.org/10.1016/j.energy.2018.03.166.

[53] Z. Tan, X. Feng, and Y. Wang. "Performance comparison of different heat pumps in low-temperature waste heat recovery". In: *Renewable and Sustainable Energy Reviews* 152 (2021), p. 111634. DOI: https://doi.org/10.1016/j.rser.2021.111634.

[54] K.J. Chua, S.K. Chou, and W.M. Yang. "Advances in heat pump systems: A review". In: *Applied Energy* 87.12 (2010), pp. 3611–3624. DOI: https://doi.org/10.1016/j.apenergy.2010.06.014.

[55] Advanced Manufacturing Office. "Use Feedwater Economizers for Waste Heat Recovery". In: *Energy Efficiency and Renewable Energy* (2012). URL: https://www.campbell-sevey.com/wp-content/uploads/2019/02/Steam-Tip-3-Feedwater-Economizers-for-Waste-Heat-Recovery.pdf.

[56] V.D. Stevanovic et al. "Efficiency and power upgrade at the aged lignite-fired power plant by flue gas waste heat utilization: High pressure versus low pressure economizer installation". In: *Energy* 187 (2019), p. 115980. DOI: https://doi.org/10.1016/j.energy.2019.115980.

[57] Z. Li et al. "Advances, challenges and perspectives of using transport membrane condenser to recover moisture and waste heat from flue gas". In: *Separation and Purification Technology* 285 (2022), p. 120331. DOI: https://doi.org/10.1016/j.seppur.2021.120331.

[58] D. Wang et al. "Coal power plant flue gas waste heat and water recovery". In: *Applied Energy* 91.1 (2012), pp. 341–348. DOI: https://doi.org/10.1016/j.apenergy.2011.10.003.

[59] K. Rahbar et al. “Review of organic Rankine cycle for small-scale applications”. In: *Energy Conversion and Management* 134 (2017), pp. 135–155. DOI: https://doi.org/10.1016/j.enconman.2016.12.023.

[60] H. Liu, Y. Shao, and J. Li. “A biomass-fired micro-scale CHP system with organic Rankine cycle (ORC) – Thermodynamic modelling studies”. In: *Biomass and Bioenergy* 35.9 (2011), pp. 3985–3994. DOI: https://doi.org/10.1016/j.biombioe.2011.06.025.

[61] H.D. Madhawa Hettiarachchi et al. “Optimum design criteria for an Organic Rankine cycle using low-temperature geothermal heat sources”. In: *Energy* 32.9 (2007), pp. 1698–1706. DOI: https://doi.org/10.1016/j.energy.2007.01.005.

[62] G. Pei, J. Li, and J. Ji. “Analysis of low temperature solar thermal electric generation using regenerative Organic Rankine Cycle”. In: *Applied Thermal Engineering* 30.8 (2010), pp. 998–1004. DOI: https://doi.org/10.1016/j.applthermaleng.2010.01.011.

[63] C. Invernizzi, P. Iora, and P. Silva. “Bottoming micro-Rankine cycles for micro-gas turbines”. In: *Applied Thermal Engineering* 27.1 (2007), pp. 100–110. DOI: https://doi.org/10.1016/j.applthermaleng.2006.05.003.

[64] T. Endo et al. “Study on Maximizing Exergy in Automotive Engines”. In: *SAE Technical Paper Series* (2007). DOI: https://doi.org/10.4271/2007-01-0257.

[65] B.F. Tchanche, M. Pétrissans, and G. Papadakis. “Heat resources and organic Rankine cycle machines”. In: *Renewable and Sustainable Energy Reviews* 39 (2014), pp. 1185–1199. DOI: https://doi.org/10.1016/j.rser.2014.07.139.

[66] P. Colonna et al. “Organic Rankine Cycle Power Systems: From the Concept to Current Technology, Applications, and an Outlook to the Future”. In: *Journal of Engineering for Gas Turbines and Power* 137.10 (2015). DOI: https://doi.org/10.1115/1.4029884.

[67] N.V. Burnete et al. “Review of thermoelectric generation for internal combustion engine waste heat recovery”. In: *Progress in Energy and Combustion Science* 91 (2022), p. 101009. DOI: https://doi.org/10.1016/j.pecs.2022.101009.

[68] J.R. Armstead and S.A. Miers. "Review of Waste Heat Recovery Mechanisms for Internal Combustion Engines". In: *Journal of Thermal Science and Engineering Applications* 6.1 (2013). DOI: https://doi.org/10.1115/1.4024882.

[69] G. Snyder and E. Toberer. "Complex Thermoelectric Materials". In: *Nature materials* 7 (2008), pp. 105–14. DOI: https://doi.org/10.1038/nmat2090.

[70] R. Patowary and D.C. Baruah. "Thermoelectric conversion of waste heat from IC engine-driven vehicles: A review of its application, issues, and solutions". In: *International Journal of Energy Research* 42.8 (2018), pp. 2595–2614. DOI: https://doi.org/10.1002/er.4021.

[71] M. Aljaghtham and E. Celik. "Design optimization of oil pan thermoelectric generator to recover waste heat from internal combustion engines". In: *Energy* 200 (2020), p. 117547. DOI: https://doi.org/10.1016/j.energy.2020.117547.

[72] Q. Cao, W. Luan, and T. Wang. "Performance enhancement of heat pipes assisted thermoelectric generator for automobile exhaust heat recovery". In: *Applied Thermal Engineering* 130 (2018), pp. 1472–1479. DOI: https://doi.org/10.1016/j.applthermaleng.2017.09.134.

[73] M. Mirhosseini, A. Rezania, and L. Rosendahl. "Power optimization and economic evaluation of thermoelectric waste heat recovery system around a rotary cement kiln". In: *Journal of Cleaner Production* 232 (2019), pp. 1321–1334. DOI: https://doi.org/10.1016/j.jclepro.2019.06.011.

[74] C. Vining. "An inconvenient truth about thermoelectrics". In: *Nature materials* 8 (2009), pp. 83–5. DOI: https://doi.org/10.1038/nmat2361.

[75] A. Kumar et al. "A Review on Fundamentals, Design and Optimization to High ZT of Thermoelectric Materials for Application to Thermoelectric Technology". In: *Journal of Electronic Materials* 50 (2021), pp. 1–23. DOI: https://doi.org/10.1007/s11664-021-09153-7.

[76] R.W. Whatmore. "Pyroelectric devices and materials". In: *Reports on Progress in Physics* 49.12 (1986), pp. 1335–1386. DOI: https://doi.org/10.1088/0034-4885/49/12/002.

[77] A. Sultana et al. “A pyroelectric generator as a self-powered temperature sensor for sustainable thermal energy harvesting from waste heat and human body heat”. In: *Applied Energy* 221 (2018), pp. 299–307. DOI: https://doi.org/10.1016/j.apenergy.2018.04.003.

[78] J. Kim et al. “Pyroelectric power generation from the waste heat of automotive exhaust gas”. In: *Sustainable Energy Fuels* 4.3 (2020), pp. 1143–1149. DOI: https://doi.org/10.1039/C9SE00283A.

[79] S. Pandya et al. “Pyroelectric energy conversion with large energy and power density in relaxor ferroelectric thin films”. In: *Nature Materials* 17 (2018). DOI: https://doi.org/10.1038/s41563-018-0059-8.

[80] R. Kandilian, A. Navid, and L. Pilon. “The pyroelectric energy harvesting capabilities of PMN–PT near the morphotropic phase boundary”. In: *Smart Materials and Structures* 20.5 (2011), p. 055020. DOI: https://doi.org/10.1088/0964-1726/20/5/055020.

[81] J. Kim et al. “Temperature stability of PIN-PMN-PT ternary ceramics during pyroelectric power generation”. In: *Journal of Alloys and Compounds* 768 (2018), pp. 22–27. DOI: https://doi.org/10.1016/j.jallcom.2018.07.182.

[82] B.P. Kasmia. “Preparation & pyroelectric properties evaluation of Lanthanum modified Lead Zirconate Titanate (PLZT) for waste heat power generation”. Master thesis. Nagaoka: Nagaoka University of Techonology, 2020.

[83] I. Sudoh. “Improvement of power generation and figure of merit evaluation by composition control of ferroelectric ceramics that contributes to energy conversion from a variable heat source”. Master thesis. Nagaoka: Nagaoka University of Techonology, 2019.

[84] H. Sugiyama et al. “Examination of pyroelectric power generation over a wide temperature range by controlling the Zr:Sn composition ratio of PLZST”. In: *Journal of Asian Ceramic Societies* 10.1 (2021), pp. 1–9. DOI: https://doi.org/10.1080/21870764.2021.2013145.

[85] Environmental Protection Agency. *Learn about Lead*. Sept. 2022. URL: https://www.epa.gov/lead/learn-about-lead#effects.

[86] M.A. Assi et al. “The detrimental effects of lead on human and animal health”. In: *Veterinary World* 9.6 (2016). DOI: https://doi.org/10.14202/vetworld.2016.660-671.

[87] B. Pourrut et al. “Lead uptake, toxicity, and detoxification in plants.” In: *Reviews of Environmental Contamination and Toxicology* 213 (2011). DOI: https://doi.org/10.1007/978-1-4419-9860-6_4.

[88] “DIRECTIVE 2002/95/EC OF THE EUROPEAN PARLIAMENT AND OF THE COUNCIL of 27 January 2003 on the restriction of the use of certain hazardous substances in electrical and electronic equipment”. In: *Official Journal of the European Union* (2003).

[89] Japanese Industrial Standards Committee. “The marking for presence of the specific chemical substances for electrical and electronic equipment”. In: *JIS* (2005).

[90] Ministry of Industry and Information Technology. “Management methods for the restriction of the use of hazardous substances in electrical and electronic products”. In: *China RoHS* (2006).

[91] Department of Economic and Social Affairs. *THE 17 GOALS*. URL: https://sdgs.un.org/goals.

[92] B. Ericson et al. “Blood lead levels in low-income and middle-income countries: a systematic review”. In: *The Lancet Planetary Health* 5.3 (2021), e145–e153. DOI: https://doi.org/10.1016/S2542-5196(20)30278-3.

[93] M. Johnsson and P. Lemmens. “Crystallography and Chemistry of Perovskites”. In: *Handbook of Magnetism and Advanced Magnetic Materials*. John Wiley & Sons, Ltd, 2007. DOI: https://doi.org/10.1002/9780470022184.hmm411.

[94] F. Li et al. “Piezoelectric activity in Perovskite ferroelectric crystals”. In: *IEEE Transactions on Ultrasonics, Ferroelectrics, and Frequency Control* 62.1 (2015), pp. 18–32. DOI: https://doi.org/10.1109/TUFFC.2014.006660.

[95] A.S. Bhalla, R. Guo, and R. Roy. “The perovskite structure—a review of its role in ceramic science and technology”. In: *Materials Research Innovations* 4.1 (2000), pp. 3–26. DOI: https://doi.org/10.1007/s100190000062.

[96] M. Tachibana, T. Kolodiazhnyi, and E. Takayama-Muromachi. “Thermal conductivity of perovskite ferroelectrics”. In: *Applied Physics Letters* 93.9 (2008), p. 092902. DOI: https://doi.org/10.1063/1.2978072.

[97] M.T. Masood. "Solution-Processable Compact and Mesoporous Titanium Dioxide Thin Films as Electron-Selective Layers for Perovskite Solar Cells". Doctor thesis. Turku: Åbo Akademi University, 2020.

[98] A. Berenov, F. Le Goupil, and N.M. Alford. "Effect of ionic radii on the Curie temperature in $Ba_{1-x-y}Sr_xCa_yTiO_3$ compounds". In: *Scientific Reports* 6 (2016), p. 28055. DOI: https://doi.org/10.1038/srep28055.

[99] C.H. Park and D.J. Chadi. "Microscopic study of oxygen-vacancy defects in ferroelectric perovskites". In: *Physical Review B* 57.22 (1998), R13961–R13964. DOI: https://doi.org/10.1103/PhysRevB.57.R13961.

[100] V. Polinger, P. Garcia-Fernandez, and I.B. Bersuker. "Pseudo Jahn–Teller origin of ferroelectric instability in $BaTiO_3$ type perovskites: The Green's function approach and beyond". In: *Physica B: Condensed Matter* 457 (2015), pp. 296–309. DOI: https://doi.org/10.1016/j.physb.2014.09.048.

[101] I. Coondoo, N. Panwar, and A. Kholkin. "Lead-free piezoelectrics: Current status and perspectives". In: *Journal of Advanced Dielectrics* 03.2 (2013), p. 1330002. DOI: https://doi.org/10.1142/S2010135X13300028.

[102] M. Acosta et al. "$BaTiO_3$-based piezoelectrics: Fundamentals, current status, and perspectives". In: *Applied Physics Reviews* 4.4 (2017), p. 041305. DOI: https://doi.org/10.1063/1.4990046.

[103] K. Nakamura, S. Higuchi, and T. Ohnuma. "Density Functional Perturbation Theory to Predict Piezoelectric Properties". In: *Perturbation Methods with Applications in Science and Engineering*. Ed. by İ. Bakırtaş. Rijeka: IntechOpen, 2018. Chap. 1. DOI: https://doi.org/10.5772/intechopen.76827.

[104] A. Arnau and D. Soares. "Fundamentals of Piezoelectricity". In: *Piezoelectric Transducers and Applications*. Ed. by A.A. Vives. Berlin, Heidelberg: Springer Berlin Heidelberg, 2008, pp. 1–38. DOI: https://doi.org/10.1007/978-3-540-77508-9_1.

[105] K. Uchino. *Ferroelectric devices*. 2nd ed. 2009, pp. 1–349.

[106] D. Fu and M. Itoh. "Role of Ca off-Centering in Tuning Ferroelectric Phase Transitions in $Ba(Zr,Ti)O_3$ System". In: *Ferroelectric Materials*. Ed. by A.P. Barranco. Rijeka: IntechOpen, 2015. Chap. 5. DOI: https://doi.org/10.5772/61017.

[107] M. Dragoman. "MoS_2 thin films as electrically tunable materials for microwave applications". In: *Applied Physics Letters* 107.24 (2015), p. 243109. DOI: https://doi.org/10.1063/1.4938145.

[108] I.H. Lone et al. "Multiferroic ABO_3 Transition Metal Oxides: a Rare Interaction of Ferroelectricity and Magnetism". In: *Nanoscale Research Letters* 14 (2019), p. 142. DOI: https://doi.org/10.1186/s11671-019-2961-7.

[109] Q. Xu et al. "Construction of Bio-Piezoelectric Platforms: From Structures and Synthesis to Applications". In: *Advanced Materials* 33.27 (2021), p. 2008452. DOI: https://doi.org/10.1002/adma.202008452.

[110] L. Gaul and J. Becker. "Model-based piezoelectric hysteresis and creep compensation for highly-dynamic feed forward rest-to-rest motion control of piezoelectrically actuated flexible structures". In: *International Journal of Engineering Science* 47.11 (2009), pp. 1193–1207. DOI: https://doi.org/10.1016/j.ijengsci.2009.07.006.

[111] "IEEE Standard on Piezoelectricity". In: *ANSI/IEEE Std 176-1987* (1988), 0_1. DOI: https://doi.org/10.1109/IEEESTD.1988.79638.

[112] A. Abdal-Kadhim and S.L. Kok. "Piezoelectric Pre-Stressed Bending Mechanism for Impact-Driven Energy Harvester". In: *IOP Conference Series: Materials Science and Engineering* 210 (June 2017), p. 012037. DOI: https://doi.org/10.1088/1757-899X/210/1/012037.

[113] P. Peng et al. "Enhanced pyroelectric properties in $(Bi_{0.5}Na_{0.5})TiO_3$–$BiAlO_3$– $NaNbO_3$ ternary system lead-free ceramics". In: *Journal of the American Ceramic Society* 101.9 (2018), pp. 4044–4052. DOI: https://doi.org/10.1111/jace.15568.

[114] S. Jachalke et al. "How to measure the pyroelectric coefficient?" In: *Applied Physics Reviews* 4.2 (2017), p. 021303. DOI: https://doi.org/10.1063/1.4983118.

[115] Y. Tang et al. "Improved Pyroelectric Properties of $CaBi_4Ti_4O_{15}$ Ferroelectrics Ceramics by Nb/Mn Co-Doping for Pyrosensors". In: *Journal of the American Ceramic Society* 99.4 (2016), pp. 1294–1298. DOI: https://doi.org/10.1111/jace.14075.

[116] Y. Tang et al. "Pyroelectric properties of Mn-doped Aurivillius ceramics with different pseudo-perovskite layers". In: *Journal of the American Ceramic Society* 101.4 (2018), pp. 1592–1597. DOI: https://doi.org/10.1111/jace.15267.

[117] B. Bhatia et al. "Pyroelectric current measurements on $PbZr_{0.2}Ti_{0.8}O_3$ epitaxial layers". In: *Journal of Applied Physics* 112.10 (2012), p. 104106. DOI: https://doi.org/10.1063/1.4766271.

[118] X. Wu et al. "The influence of defects on ferroelectric and pyroelectric properties of $Pb(Mg_{1/3}Nb_{2/3})O_3$–$0.28PbTiO_3$ single crystals". In: *Materials Chemistry and Physics* 132.1 (2012), pp. 87–90. DOI: https://doi.org/10.1016/j.matchemphys.2011.10.055.

[119] C.R. Bowen et al. "Pyroelectric materials and devices for energy harvesting applications". In: *Energy & Environmental Science* 7.12 (2014), pp. 3836–3856. DOI: https://doi.org/10.1039/C4EE01759E.

[120] J. Zhu et al. "Thermal equations of state and phase relation of $PbTiO_3$: A high P-T synchrotron X-ray diffraction study". In: *Journal of Applied Physics* 110.8 (2011), p. 084103. DOI: https://doi.org/10.1063/1.3651377.

[121] A. Tagantsev et al. "The origin of antiferroelectricity in $PbZrO_3$". In: *Nature communications* 4 (2013), p. 3229. DOI: https://doi.org/10.1038/ncomms3229.

[122] M. Ahtee and A.M. Glazer. "Lattice parameters and tilted octahedra in sodium-potassium niobate solid solutions". In: *Acta Crystallographica Section A* 32.3 (1976), pp. 434–446. DOI: https://doi.org/10.1107/S0567739476000983.

[123] T. Sato et al. "Extending the applicability of the Goldschmidt tolerance factor to arbitrary ionic compounds". In: *Scientific reports* 6 (2016), p. 23592. DOI: https://doi.org/10.1038/srep23592.

[124] C.J. Bartel et al. "New tolerance factor to predict the stability of perovskite oxides and halides". In: *Science Advances* 5.2 (2019), eaav0693. DOI: https://doi.org/10.1126/sciadv.aav0693.

[125] W. Travis et al. "On the application of the tolerance factor to inorganic and hybrid halide perovskites: a revised system". In: *Chemical Science* 7.7 (2016), pp. 4548–4556. DOI: https://doi.org/10.1039/C5SC04845A.

[126] M. Li et al. "Interband electronic transitions and phase diagram of $PbZr_{1-x}Ti_xO_3$ ($0.05 \leq x \leq 0.70$) ceramics: ellipsometric experiment and first-principles theory". In: *Journal of Physics D: Applied Physics* 49 (2016), p. 275305. DOI: https://doi.org/10.1088/0022-3727/49/27/275305.

[127] D. Shangguan et al. "Enhanced energy-storage performances of (1-x)$PbZrO_3$-x$PbSnO_3$ antiferroelectric thin films under low electric fields". In: *Journal of Alloys and Compounds* 870 (2021), p. 159440. DOI: https://doi.org/10.1016/j.jallcom.2021.159440.

[128] Z. Lili and Y. Huang. "Theory of relaxor-ferroelectricity". In: *Scientific Reports* 10 (2020). DOI: https://doi.org/10.1038/s41598-020-61911-5.

[129] M. Manley et al. "Phonon localization drives polar nanoregions in a relaxor ferroelectric". In: *Nature communications* 5 (Apr. 2014), p. 3683. DOI: https://doi.org/10.1038/ncomms4683.

[130] L.K. Pradhan and M. Kar. "Relaxor Ferroelectric Oxides: Concept to Applications". In: *Multifunctional Ferroelectric Materials*. Ed. by D.R. Sahu. Rijeka: IntechOpen, 2021. Chap. 4. DOI: https://doi.org/10.5772/intechopen.96185.

[131] R. Kandilian, A. Navid, and L. Pilon. "The pyroelectric energy harvesting capabilities of PMN–PT near the morphotropic phase boundary". In: *Smart Materials and Structures* 20.5 (2011), p. 055020. DOI: https://doi.org/10.1088/0964-1726/20/5/055020.

[132] F.Y. Lee et al. "Pyroelectric energy conversion using PLZT ceramics and the ferroelectric–ergodic relaxor phase transition". In: *Smart Materials and Structures* 22.2 (2013), p. 025038. DOI: https://doi.org/10.1088/0964-1726/22/2/025038.

[133] H. Sugiyama et al. "Pyroelectric power generation in PLZST material by temperature dependent phase transformation". In: *Ceramics International* 48.6 (2022), pp. 8689–8695. DOI: https://doi.org/10.1016/j.ceramint.2021.12.080.

[134] F. Moura et al. "Dielectric and ferroelectric characteristics of barium zirconate titanate ceramics prepared from mixed oxide method". In: *Journal of Alloys and Compounds* 462.1 (2008), pp. 129–134. DOI: https://doi.org/10.1016/j.jallcom.2007.07.077.

[135] M. Zhu et al. "Diffused phase transition boosted dye degradation with $Ba(Zr_xTi_{1-x})O_3$ solid solutions through piezoelectric effect". In: *Nano Energy* 89 (2021), p. 106474. DOI: https://doi.org/10.1016/j.nanoen.2021.106474.

[136] D. Ricinschi et al. "Ferroelectric–relaxor crossover characteristics in $Ba(Zr_xTi_{1-x})O_3$ ceramics investigated by AFM-piezoresponse study". In: *Journal of the European Ceramic Society* 30.2 (2010), pp. 237–241. DOI: https://doi.org/10.1016/j.jeurceramsoc.2009.05.022.

[137] C. Ciomaga et al. "Preparation and characterisation of the $Ba(Zr,Ti)O_3$ ceramics with relaxor properties". In: *Journal of the European Ceramic Society* 27.13 (2007), pp. 4061–4064. DOI: https://doi.org/10.1016/j.jeurceramsoc.2007.02.095.

[138] W. Cai et al. "Effects of oxygen partial pressure on the electrical properties and phase transitions in $(Ba,Ca)(Ti,Zr)O_3$ ceramics". In: *Journal of Materials Science* 55 (2020), pp. 9972–9992. DOI: https://doi.org/10.1007/s10853-020-04771-8.

[139] G. Bhargavi et al. "Analysis of temperature and frequency dependent dielectric properties, dynamic hysteresis loop and thermal energy conversion in $BaZr_{0.05}Ti_{0.95}O_3$ ceramic". In: *Journal of Materials Science: Materials in Electronics* 29 (2018), pp. 11439–11448. DOI: https://doi.org/10.1007/s10854-018-9236-4.

[140] D. Ando and K. Kakimoto. "Pyroelectric energy harvesting using low-T_C (1-x)$(Ba_{0.7}Ca_{0.3})TiO_3$-x$Ba(Zr_{0.2}Ti_{0.8})O_3$ bulk ceramics". In: *Journal of the American Ceramic Society* 101.11 (2018), pp. 5061–5070. DOI: https://doi.org/10.1111/jace.15746.

[141] S. Patel et al. "Enhanced thermal energy conversion and dynamic hysteresis behavior of Sr-added $Ba_{0.85}Ca_{0.15}Ti_{0.9}Zr_{0.1}O_3$ ferroelectric ceramics". In: *Journal of Materiomics* 2 (2016), pp. 75–86. DOI: https://doi.org/10.1016/j.jmat.2016.01.002.

[142] D. Sharma et al. "Thermal energy conversion and temperature-dependent dynamic hysteresis analysis for $Ba_{0.85}Ca_{0.15}Ti_{0.9-x}Fe_xZr_{0.1}O_3$ ceramics". In: *Journal of Asian Ceramic Societies* 4.1 (2016), pp. 102–111. DOI: https://doi.org/10.1016/j.jascer.2015.12.005.

[143] S. Khobragade and S. Patel. "Thermal Energy Harvesting Capabilities in Lead-Free $Ba_{0.85}Ca_{0.15}Ti_{0.9-x}Sn_xZr_{0.1}O_3$ Ferroelectric Ceramics". In: *Journal of Electronic Materials* 49 (2019), pp. 1194–1203. DOI: https://doi.org/10.1007/s11664-019-07821-3.

[144] B. Fan et al. "Lead-free $Ba(1-x)Sr_xTiO_3$ ceramics for room-temperature pyroelectric energy conversion". In: *Ceramics International* 44.7 (2018), pp. 8270–8276. DOI: https://doi.org/10.1016/j.ceramint.2018.02.009.

[145] J. Binner and T.S.R.C. Murthy. "Structural and Thermostructural Ceramics". In: *Encyclopedia of Materials: Technical Ceramics and Glasses*. Ed. by M. Pomeroy. Vol. 2. Amsterdam: Elsevier, 2021, pp. 3–24.

[146] A. Leriche, S. Hampshire, and F. Cambier. "Control of the Microstructure in Ceramics". In: *Encyclopedia of Materials: Technical Ceramics and Glasses*. Ed. by M. Pomeroy. Vol. 2. Amsterdam: Elsevier, 2021, pp. 349–366.

[147] L. Dong, D.S. Stone, and R.S. Lakes. "Enhanced dielectric and piezoelectric properties of $xBaZrO_3$-$(1-x)BaTiO_3$ ceramics". In: *Journal of Applied Physics* 111.8 (2012), p. 084107. DOI: https://doi.org/10.1063/1.4705467.

[148] E. Fatuzzo, H. Kiess, and R. Nitsche. "Theoretical Efficiency of Pyroelectric Power Converters". In: *Journal of Applied Physics* 37.2 (1966), pp. 510–516. DOI: https://doi.org/10.1063/1.1708205.

[149] A. van der Ziel. "Solar power generation with the pyroelectric effect". In: *Journal of Applied Physics* 45.9 (1974), pp. 4128–4128. DOI: https://doi.org/10.1063/1.1663926.

[150] D.G. Frood. "A Note on the use of the titanates as thermoelectric transducers". In: *Canadian Journal of Physics* 32.4 (1954), pp. 313–317. DOI: https://doi.org/10.1139/p54-029.

[151] S.R. Hoh. "Conversion of thermal to electrical energy with ferroelectric materials". In: *Proceedings of the IEEE* 51.5 (1963), pp. 838–845. DOI: https://doi.org/10.1109/PROC.1963.2277.

[152] B.H. Beam, J.F. Fry, and L.D. Russell. "Experiments on Radiant Energy Conversion using thin Dielectric Films". In: *Space Power Systems Engineering*. Ed. by G.C. Szego and J.E. Taylor. Vol. 16. Elsevier, 1966, pp. 877–894. DOI: https://doi.org/10.1016/B978-1-4832-3056-6.50042-6.

[153] R.B. Olsen and D.D. Brown. "High efficiency direct conversion of heat to electrical energy-related pyroelectric measurements". In: *Ferroelectrics* 40.1 (1982), pp. 17–27. DOI: https://doi.org/10.1080/00150198208210592.

[154] R.B. Olsen. "Ferroelectric Conversion of Heat to Electrical Energy: A Demonstration". In: *Journal of Energy* 6.2 (1982), pp. 91–95. DOI: https://doi.org/10.2514/3.62580.

[155] R.B. Olsen, D.A. Bruno, and J. M. Briscoe. "Pyroelectric conversion cycles". In: *Journal of Applied Physics* 58.12 (1985), pp. 4709–4716. DOI: https://doi.org/10.1063/1.336244.

[156] S. Pandya et al. "New approach to waste-heat energy harvesting: pyroelectric energy conversion". In: *NPG Asia Materials* 11 (2019), p. 26. DOI: https://doi.org/10.1038/s41427-019-0125-y.

[157] Y. Kim et al. "Novel Electrothermodynamic Power Generation". In: *Advanced Energy Materials* 5.13 (2015), p. 1401942. DOI: https://doi.org/10.1002/aenm.201401942.

[158] F.Y. Lee et al. "Pyroelectric waste heat energy harvesting using relaxor ferroelectric 8/65/35 PLZT and the Olsen cycle". In: *Smart Materials and Structures* 21.2 (2012), p. 025021. DOI: https://doi.org/10.1088/0964-1726/21/2/025021.

[159] A. Siao et al. "Pyroelectric waste heat energy harvesting using the Olsen cycle on Pb(Zr, Ti)O_3-Pb(Ni, Nb)O_3 ceramics". In: *Journal of Applied Physics* 124.17 (2018), p. 174104. DOI: https://doi.org/10.1063/1.5037112.

[160] C. Ye, T. Tamagawa, and D.L. Polla. "Experimental studies on primary and secondary pyroelectric effects in $Pb(Zr_xTi_{1-x})O_3$, $PbTiO_3$, and ZnO thin films". In: *Journal of Applied Physics* 70.10 (1991), pp. 5538–5543. DOI: https://doi.org/10.1063/1.350212.

[161] K.H. Chew et al. "Primary and secondary pyroelectric effects of ferroelectric 0-3 composites". In: *Journal of Applied Physics* 94.2 (2003), pp. 1134–1145. DOI: https://doi.org/10.1063/1.1583154.

[162] A.S. Bhalla and R.E. Newnham. "Primary and secondary pyroelectricity". In: *Physica status solidi (a)* 58.1 (1980), K19–K24. DOI: https://doi.org/10.1002/pssa.2210580146.

[163] A. Movchikova et al. "The role of the secondary pyroelectric effect in a ferroelectric relaxor $0.72Pb(Mg_{1/3}Nb_{2/3})O_3$-$0.28PbTiO_3$". In: *Bulletin of the Russian Academy of Sciences: Physics* 74 (Sept. 2010), pp. 1270–1271. DOI: https://doi.org/10.3103/S106287381009025X.

[164] I. McKinley, R. Kandilian, and L. Pilon. "Waste heat energy harvesting using the Olsen cycle on $0.945Pb(Zn_{1/3}Nb_{2/3})O_3$– $0.055PbTiO_3$ single crystals". In: *Smart Materials and Structures* 21 (2012), p. 035015. DOI: https://doi.org/10.1088/0964-1726/21/3/035015.

[165] D.W. Hahn and M.N. Özisik. *Heat conduction*. 3rd ed. Hoboken: Wiley, 2012. DOI: https://doi.org/10.1002/9781118411285.

[166] L. You et al. "Effect of lanthanum doping on tetragonal-like $BiFeO_3$ with mixed-phase domain structures". In: *Physical Review B* 90.13 (2014), p. 134110. DOI: https://doi.org/10.1103/PhysRevB.90.134110.

Acknowledgement

I would like to express my deepest appreciation to my supervisor, Prof. Tadachika Nakayama, for the patient guidance, encouragement, and advice he has provided throughout my time as his student. Thanks to Prof. Tadachika Nakayama, I had a chance to experience an interesting research subject, an opportunity for an internship at a global company, and mostly a fulfilling 7 years of studying abroad.

I would like to express my sincere gratitude to Prof. Hisayuki Suematsu, and Associate Prof. Tsuneo Suzuki of the Extreme Energy-Density Research Institute. Together with Prof. Nakayama, Prof. Hisayuki Suematsu, and Associate Prof. Tsuneo Suzuki with all of their valuable comments, understanding, and support, have guided me and this research through all of the difficulties and challenges.

I am also thankful to Prof. Masatoshi Takeda, Prof. Noboru Yamada, Specially Appointed Prof. Juan Paulo Wiff, and Assistant Prof. Masaki Baba for all their support during experiments and profound knowledge in this field.

This endeavor would not have been possible without Dr. Tan Minh Triet Huynh and all of his encouragement, understanding, and assistance. He's always been there when I need him most. I would like to extend my sincere thanks to Dr. Phuong Thao Bui, Dr. Duy Hieu Nguyen, and Dr. Minh Chu Ngo. They are the best seniors and friends that I could wish for.

I am also thankful to Dr. Hironari Sugiyama, Mr. Genki Onishi, and Mr. Iori Sudoh for all of their instruction and comments on my research. Without any of them, I might have not finished this journey.

I would like to express my sincere gratitude to Mr. Akio Shida of technical staff, Ms. Noriko Araki and Mr. Akira Ishizaki of technical assistant, Ms.

Kayoko Watanabe, Ms. Chiyoe Niitsuya, and Ms. Konishi Nana of secretary, to my seniors, colleagues, and juniors in the laboratory with whom I have shared a lot of time.

I would like to express my heartfelt gratitude to my parents, my sister, my partners, and my family, who have always watched over me warmly and given me love at all times. Thank you very much.

Part of this research was supported by the New Energy and Industrial Development Organization (NEDO) through the NEDO Leading Research Program. We would like to express our sincere gratitude.

Achievements

Original article

1. Nguyen Chi Trung Ngo, Hironari Sugiyama, Buddhika Amila Kumara Sodige, Juan Paulo Wiff, Satoru Yamanaka, Yoonho Kim, Tsuneo Suzuki, Masaaki Baba, Masatoshi Takeda, Noboru Yamada, Koichi Niihara, and Tadachika Nakayama. "Sensitivity and effectivity of Kim's novel electro-thermodynamic cycle over Olsen cycle on waste heat recovering with high fluctuating temperature source using lead-free pyroelectric $Ba(Zr_{0.1}Ti_{0.9})O_3$". *AIP Advances*. **11** (2021) 125310.

2. Nguyen Chi Trung Ngo, Hironari Sugiyama, Buddhika Amila Kumara Sodige, Juan Paulo Wiff, Satoru Yamanaka, Yoonho Kim, Tsuneo Suzuki, Masaaki Baba, Masatoshi Takeda, Noboru Yamada, Koichi Niihara, and Tadachika Nakayama. "Enhancing low-temperature energy harvesting by lead-free ferroelectric $Ba(Zr_{0.1}Ti_{0.9})O_3$". *Journal of the American Ceramic Society*. **106** (2023) 201-212.

3. Nguyen Chi Trung Ngo, Hironari Sugiyama, Buddhika Amila Kumara Sodige, Juan Paulo Wiff, Hideto Furuno, Satoru Yamanaka, Yoonho Kim, Tsuneo Suzuki, Masaaki Baba, Masatoshi Takeda, Noboru Yamada, Koichi Niihara, and Tadachika Nakayama. "Enhancing low-grade waste heat recovery by lead-free ferroelectric $Ba(Zr_{0.1}Ti_{0.9})O_3$ with Sr and Ca isovalent dopants. *Ceramics International*. Accepted.

Conferrence

1. N. C. T. Ngo, G. Onishi, T. M. T. Huynh, T. Nakayama, T. Suzuki, H. Suematsu, and K. Niihara. "ZrO_2 micro particles transferring in

polysiloxane solution under the nanosecond pulsed electric field". *The 9 th U3 Materials Design Forum.* Mar. 2018. Hikone, Japan. (Oral).

2. N. C. T. Ngo, J. P. Wiff, T. Suzuki, H. Suematsu, and T. Nakayama. "Lead-free pyroelectric $(Ba_{1-x}Ca_x)(Zr_{0.1}Ti_{0.9})O_3$ for low-grade waste heat recovery via power generation". *The 7th International Symposium on Organic and Inorganic Electronic Materials and Related Nanotechnologies.* Jun. 2019. Matsumoto, Japan. (Oral).

3. N. C. T. Ngo, H. Sugiyama, J. P. Wiff, T. Suzuki, H. Suematsu, and T. Nakayama. "Y doped (Pb, Ba, La)(Zr, Sn, Ti)O_3 lead-based pyroelectric materials for low-grade waste heat harvesting". *The ^{36}th International Japan-Korea Seminar on Ceramics.* Nov. 2019. Tottori, Japan. (Oral)

4. N. C. T. Ngo, H. Sugiyama, J. P. Wiff, T. Suzuki, H. Suematsu, and T. Nakayama. "Er-doped (Pb, Ba, La)(Zr, Sn, Ti)O3 lead-based pyroelectric materials for low-grade waste heat harvesting". *The 45th International Conference and Exposition on Advanced Ceramics.* Feb. 2021. Virtual. (Oral)

5. N. C. T. Ngo, H. Sugiyama, J. P. Wiff, T. Suzuki, H. Suematsu, and T. Nakayama. "Low temperature pyroelectric energy harvesting of lead-free ceramic Ba(Zr Ti)O_3 using the Kim cycle". *The 5th International Symposium on Hybrid Materials and Processing* Jul. 2021. Virtual. (Oral)

6. N. C. T. Ngo, H. Sugiyama, B. A. K. Sodige, J. P. Wiff, T. Suzuki, H. Suematsu, and T. Nakayama. "Effect of Ca and Sr doping on the low-temperature power generation of lead-free pyroelectric Ba(Zr Ti)O_3". *The 1st International Young Generation Symposium.* Dec. 2022. Kobe, Japan. (Oral)

7. N. C. T. Ngo, H. Sugiyama, B. A. K. Sodige, J. P. Wiff, T. Suzuki, H. Suematsu, and T. Nakayama. "Enhancing the power generation of lead-free pyroelectric Ba(Zr Ti)O_3 with strontium (Sr) doping". *The 47th International Conference and Exposition on Advanced Ceramics.* Jan. 2023. Daytona Beach, United State of America. (Oral)

Award

1. The 1st International Young Generation Symposium. Presentation award. Dec. 2022.